Local Gas Injection as a Scrape-off Layer Diagnostic on the Alcator C-Mod Tokamak

by

David F. Jablonski

B.S. Applied Physics, Columbia University (1991)

Submitted to the Department of Nuclear Engineering
in Partial Fulfillment of the Requirements for the Degree of

Doctor of Philosophy

at the
Massachusetts Institute of Technology
May 1996

© 1996 Massachusetts Institute of Technology. All rights reserved.

Signature of Author

Department of Nuclear Engineering
22 May 1996

Certified by _____

Brian LaBombard
Research Scientist, Plasma Fusion Center
Thesis Supervisor

Certified by _____

George M. McCracken
Research Scientist, Plasma Fusion Center
Thesis Reader

Certified by _____

Ian H. Hutchinson
Professor, Department of Nuclear Engineering
Thesis Reader

Accepted by _____

Jeffrey P. Freidberg
Professor, Department of Nuclear Engineering
Chairman, Department Committee on Graduate Students

Local Gas Injection as a Scrape-off Layer Diagnostic on the Alcator C-Mod Tokamak

by

David F. Jablonski

Submitted to the Department of Nuclear Engineering on 22 May 1996
in Partial Fulfillment of the Requirements for the Degree of

Doctor of Philosophy

ABSTRACT

A capillary puffing array has been installed on Alcator C-Mod which allows localized introduction of gaseous species in the scrape-off layer. This system has been utilized in experiments to elucidate both global and local properties of edge transport. Deuterium fueling and recycling impurity screening are observed to be characterized by non-dimensional screening efficiencies which are independent of the location of introduction. In contrast, the behaviour of non-recycling impurities is seen to be characterized by a screening time which is dependent on puff location.

The work of this thesis has focused on the use of the capillary array with a camera system which can view impurity line emission plumes formed in the region of an injection location. The ionic plumes observed extend along the magnetic field line with a comet-like asymmetry, indicative of background plasma ion flow. The flow is observed to be towards the nearest strike-point, independent of x-point location, magnetic field direction, and other plasma parameters. While the axes of the plumes are generally along the field line, deviations are seen which indicate cross-field ion drifts.

A quasi-two dimensional fluid model has been constructed to use the plume shapes of the first charge state impurity ions to extract information about the local background plasma, specifically the temperature, parallel flow velocity, and radial electric field. Through comparisons of model results with those of a three dimensional Monte Carlo code, and comparisons of plume extracted parameters with scanning probe measurements, the efficacy of the model is demonstrated. Plume analysis not only leads to understandings of local edge impurity transport, but also presents a novel diagnostic technique.

Thesis Supervisor: Brian LaBombard
Research Scientist, Plasma Fusion Center

Thesis Reader: George M. McCracken
Research Scientist, Plasma Fusion Center

Thesis Reader: Ian H. Hutchinson
Professor, Department of Nuclear Engineering

Acknowledgments

I would find much amusement in finding the statement "I acknowledge nobody; I did it all myself" written at the beginning of a thesis. Alas, such will not be stated here. Without the contributions of many, the work of this thesis could not have begun, much less been completed.

First and foremost, I would like to thank the research scientists, engineers, technicians, support staff, and my fellow grad students of the MIT Plasma Fusion Center with whom I have had the pleasure to work these past five years. I can say, without even a touch of sarcasm, that this has been the best work environment I have ever encountered. Particular mention needs to be given of Brian LaBombard, who has managed to retain his sanity even after supervising me for half a decade. I would like to thank Brian, Bruce Lipschultz, Garry McCracken, Bob Childs, and Tom Toland for the many hours of work they contributed to the design, installation, and implementation of the NINJA system. I would like to acknowledge Garry, Jim Terry, and Aaron Allen for their work on the successful implementation of a plume imaging system. Specific mention need also be given to Brian, Garry, and Ian Hutchinson for their comments and suggestion on the content and text of this thesis, which led to Herculean improvement in the presentation of the work. Steve Lisgo, a grad student at the University of Toronto, spent many days performing and perfecting the DIVIMP calculations presented in the pages that follow, and to him, I owe a great deal of gratitude as well.

My education in plasma physics has not been a self-taught course. I have benefited from world class instruction at both MIT and Columbia. At Columbia, Paul Diament, a professor in the Electrical Engineering department, instilled in me an appreciation for the beauty of Maxwell's Equations which has stayed with me to this day. Michael Mauel and Gerald Navratil, both of the Applied Physics department, provided me with a solid introduction to plasma physics; specific mention needs be made of Mike, who, for better or worse, got me into this whole fusion game. That solid background in science and plasma physics has been greatly expanded

and enhanced by the professors of MIT, particular by Ian, a teacher beyond par. Also inimitable to my education has been the truly endless hours of discussion with Brian and Garry, some of which has even been devoted to plasma physics.

I owe a great deal to a great number of people who have not had direct attachment to my work on C-Mod, who have nonetheless made my time here possible and enjoyable. I would first like to thank Linda, Lawrence, and Brent Light, Francis, Margaret, Frank, Angela, and Lottie Jablonski, Reynold and Helen Schwartz, and the other members of my family for their support and kinship. I would also like to thank David 'Gleek' Amanullah, Tim 'Gobbs' Barry, Janet 'Mrs. Kotter' Clesse, Victor 'Hugo' Contero, Delores 'Pebbles' Darcy, Ronald 'Carmine' Gee, Jerry 'Bam-Bam' Godfrey, Kumud 'Egon' Jindal, Gillian 'gillian' McLaughlin, Richard 'Boing' Miller, Rajiv 'Qweef' Modak, Daniel 'Professor' Moriarty, Brian 'Slug' Murray, David 'Mousse' Park, Tim 'Whopperhead' Rankin, Robert 'Hump' Reardon, Glenn 'Twiki' Schroter, Yuichi 'Toad' Seki, and Kirsten 'Phoebe' Thompson for their support and the great pleasure their friendships have given me. Mention should be made as well of Pierre, Voillaine, Hitesh, Kelly, Kathy, Chris, Gleb, Jen, Henri, Johnathan, Kevin, Tim, and Matt, whom have all been treated to the unique pleasure of sharing an abode with me while I have attended the Institute.

Table of Contents

List of Figures

List of Tables

Chapter 1
Background

The motivation for this thesis, and for all fusion research, is the building of a commercially viable fusion-based power plant. The first section provides a brief summary of the progress made towards this goal over the past fifty years. In the two sections that follow, more specific background to the experimental program of this thesis is given, specifically on the machine on which the research takes place, and on the sub-field of fusion work into which the research of this dissertation falls. The final section provides a brief summary of the specific goals and motivations for the research program and an outline of the chapters that follow.

1.1 Fusion and the Tokamak[1]

Nuclear fusion has been considered a potential commercial power source since the discovery in the late 1930's that it was fusion reactions that powered the sun. Each atomic nucleus has a certain binding energy associated with it. If one imagines building nuclei from individual protons

---

[1]The primary sources for this section are:

     R. Herman, Fusion: The Search for Endless Energy, New York: Cambridge University Press, 1990.

     J.A. Wesson, ed., Tokamaks, Chapter 1, New York: Oxford University Press, 1987.

and neutrons, there would be a certain amount of energy liberated (by conversion from mass) upon the hypothetical joining of these particles to form a nucleus. Figure 1.1 shows a plot of this binding energy divided by the number of nucleons in the respective nucleus as a function of the atomic number.[2] The curve peaks with Iron-56 at just under 9 MeV per nucleon. Energy is liberated when nuclei combine or break apart so as to move from nuclei of lower to those of higher binding energy per nucleon. The process of splitting a nucleus, so as to move from the right part of the plot towards the center, is fission. The process of lighter nuclei combining to produce heavier nuclei, so as to move from the far left side of the plot towards the center, is fusion. Though energy production on the order of mega-electron volts may seem small (1 MeV being the equivalent of 1.6×10^{-13} Joules), it translates into astronomical energy liberation for small quantities of mass.

Fusion and fission research began at about the same time. The implementation of fission for commercial power production has proved far easier. Fusion is known to work as an energy source rather well -- witness the sun and the H-bomb. The use of it in a controlled manner by an electric utility has proven difficult if not intractable, even after fifty years of effort. The key with fusion is for the light nuclei to overcome their mutual repulsion. If one sets two protons next to each other, they will indeed not fuse because of the electrostatic repulsion of their positive charges. The sun and the H-bomb induce fusion in a similar manner, compressing light nuclei to very high densities (thousands of times denser than lead) at very high temperatures, forcing the nuclei to fuse into heavier nuclei and release energy. The sun accomplishes this feat with enormous

---

[2]K.S. Krane, <u>Introductory Nuclear Physics</u>, New York: John Wiley & Sons, 1988, p. 67.

gravitational pressure, an H-bomb with the use of an A-bomb. Neither method is practical for utility purposes. This leads one to two potential approaches for controlled fusion. The first works somewhat similarly to an H-bomb, only substituting high powered lasers or ion beams for an A-bomb, and using less fuel. This approach has been coined Inertial Confinement Fusion (ICF). The second does not attempt to reach the high pressures of the sun, but instead accepts very low density (thousands of times less dense than air), using very high temperatures (ten times hotter than the sun's center) to accomplish the same feat. Both approaches have been pursued in the past few decades. Though an arguable point, the second approach has met with greater progress.

Because this second approach involves such high temperatures, great care need be taken in holding the fuel. The approach is termed Magnetic Confinement Fusion (MCF) because of the use of magnetic fields to contain the light nuclei used in the process. When the temperature of a gas gets higher than a few eV (1 ev≈12000K), the constituent atoms ionize, with the electrons and nuclei dissociating. The resultant ionized gas, generally with overall electric neutrality but made up of individually charged particles, is termed a plasma. Because charged particles will tend to follow a magnetic field, magnetic fields can be used to contain and control it. One can imagine putting the plasma into a solenoid, with the charged particles being confined along the field lines. A simple straight solenoid would well hold the plasma from moving radially outward, but, because one could not make the solenoid infinitely long, the plasma would fly out the ends. The obvious solution is to bend the solenoid back upon itself, leading one to the toroidal, or donut, shape utilized in most MCF research devices.

Figure 1.1: Binding Energy of the Nucleons

Figure 1.1: Binding Energy of the Nucleons
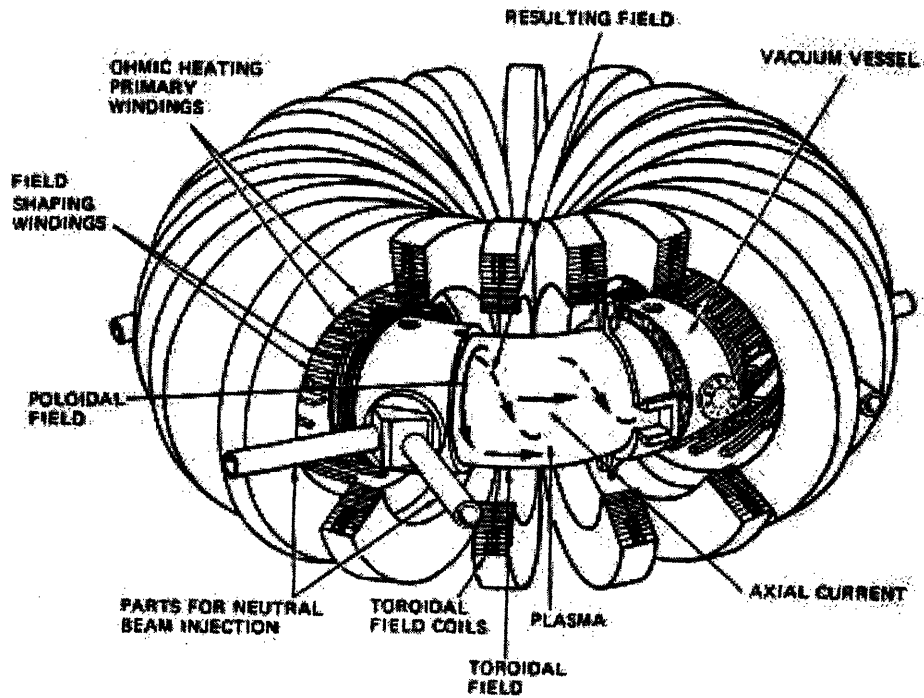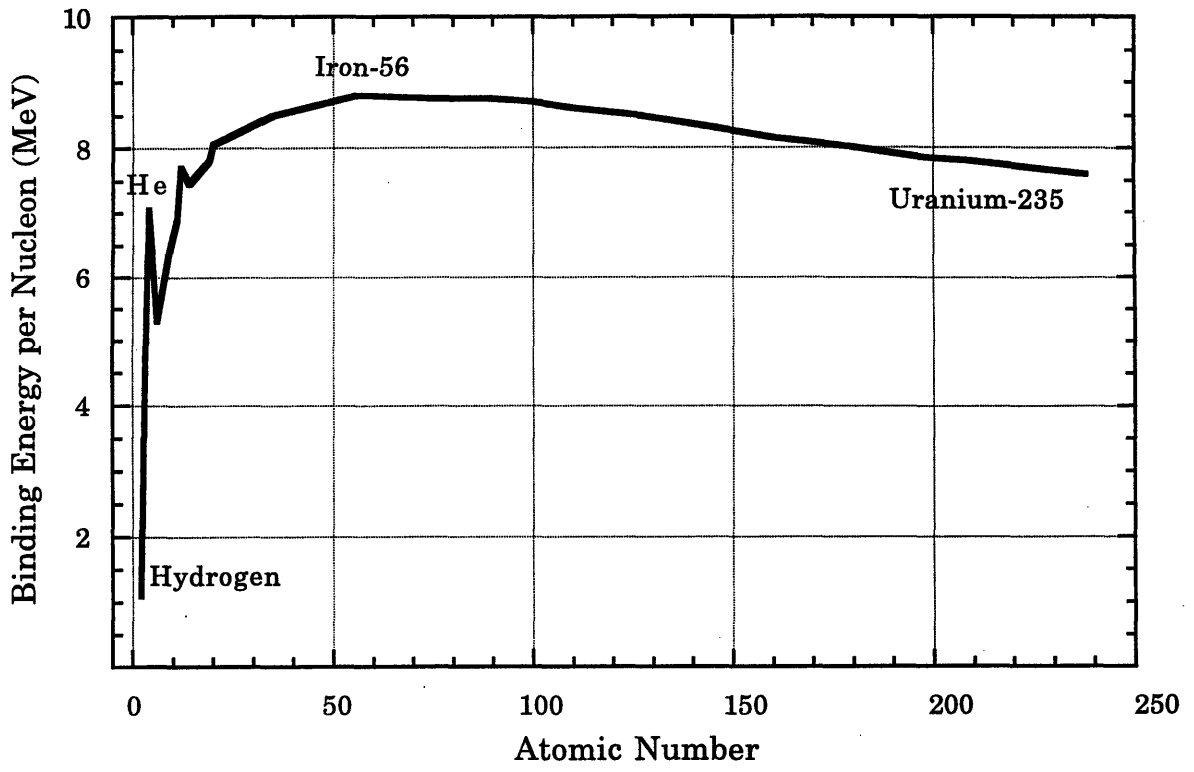
Figure 1.2: Schematic of a Tokamak

Spurred by Juan Peron's false claims of Argentinean Physicists building a fusion power device, the U.S., U.K., and Soviet Union launched MCF programs in earnest in the early 1950's. For national security reasons, the programs were at first highly classified, but by the late 1950's, when it became apparent that fusion power plants were far in the future and that the military applications of the devices were limited, the work was unclassified, and an international fusion research community was born. A number of different devices were experimented with, most with a toroidal shape, as mentioned above. Though progress was made, it was slow, and the level of understanding of the physics involved limited. At the 1968 International Atomic Energy Agency (IAEA) conference in Novosibirsk, Siberia, the Soviets announced a breakthrough. They claimed the construction of a device that produced temperatures and confinement times ten times greater than those the most advanced American and British machines had attained. Though these results were initially met with skepticism, they were eventually confirmed, and the world fusion community did a quick change of gear to adopt the Soviet design. The Soviet machine, termed the tokamak (Russian acronym for 'toroidalnya kamera ee magnetnaya katushka' or 'the toroidal chamber and magnetic coil') is a toroidal solenoid device like the others, but with an induced plasma current. The electric current, produced inductively, gives the magnetic field in the torus a helical shape, a property which has been found to be beneficial for plasma containment. Conceived in 1951 by Sakharov and

Tamm,[3] the basics of it are shown in figure 1.2.[4] Notice the solenoid, producing a magnetic field down the center of the torus, with the plasma current, induced by the inductor ('ohmic') primary, giving the field its helical twist. There are additional 'poloidal field' coils, circularly shaped, to stabilize and shape the plasma. The purpose of these extra coils can be understood by remembering that parallel currents repel, anti-parallel currents attract. The plasma, with a current running through it, has a tendency to move about; these coils are in place to keep the plasma where it is desired. The shaping function of these coils is of more recent interest; one can shape the plasma to produce desired properties. The figure also refers to Neutral Beam Injection, one method of heating the plasma to complement the resistive heating caused by the plasma current.

Since the publication of the Soviet results in the late 1960's, MCF research has had a tokamak focus, simply because, even 30 years later, it is the tokamak that gives far and away the best results. Steady progress has been made towards the power plant goal. So called scientific breakeven, in which as much energy is produced by fusion as is expended in maintaining the plasma, has been approached, and in some cases surpassed, on the fusion community's flagship machines (TFTR at Princeton, DIII-D at GA Technologies in San Diego, JET in Abingdon, England, and JT-60U in Naka-machi, Japan), though a caveat need be added. The experiments which reached these thresholds involved the use of straight Deuterium fuel. Proper breakeven would have been reached if a mixture of Deuterium and Tritium had been used for an identical experiment (hence one would

---

[3]A.D. Sakharov and I.E. Tamm, "Theory of a Magnetic Thermonuclear Reactor", in Plasma Physics and the Problem of Controlled Thermonuclear Reactions, Volume 1, New York: Pergamon Press, 1961, pp. 1-47.
[4]Figure taken from J.M. Rawls, et al, "Status of Tokamak Research", DOE/ER-0034 (1979).

better term the accomplishment 'equivalent breakeven'). Most tokamaks are not designed to use Tritium (Tritium is rather problematic to handle). The two machines that are so equipped, TFTR and JET, have recently begun experiments in which both Deuterium and Tritium are employed. This mixture is thought to be the easiest path to building a fusion power plant; though other fuel possibilities do exist (such as straight Deuterium, Deuterium and Helium-3, and Hydrogen and Boron), these alternatives entail a much higher barrier for reaching breakeven.

Though there is much physics and engineering work to be done with existing machines, the next big step in tokamak research, that of reaching ignition, will require a next generation machine. Ignition involves producing enough fusion in the tokamak plasma so that not only is more energy produced than used, but the reactions themselves are self-sustaining. The focus of this effort is the International Thermonuclear Experimental Reactor (ITER), a joint collaboration between the United States, the European Union, Japan, and Russia.[5] Though the project has an uncertain future, the ITER effort has become the raison d'être of the fusion community, with most experimental tokamak work designed to be 'ITER relevant'. ITER is planned to have two stages: the first for physics work, dealing with the consequences of ignition in particular; the second for engineering work, to deal with the engineering and design problems which will need be solved to build a demonstration tokamak power reactor. If ITER is built, its cost is likely to be in excess of $10 billion, with

---

[5]Recent Summaries of ITER work include:
     G. Janeschitz, "Status of ITER", Plasma Phys Control Fusion, 37 (1995), pp. A19-35.
     D.E. Post, "ITER: Physics Basis", Plasma Physics and Controlled Nuclear Fusion Research 1990, Volume 3, pp. 239-53.

construction not completed until well into the first decade of the 21st century.

There is much physics to be understood, and perhaps even more engineering to be done. Few doubt that ITER could be built and ignition reached. Even then however, to get to a power plant will require much development, particularly to make such a plant economically viable. Some have concluded that it is indeed a pipe dream because of the inherent complexity, and hence cost, endemic to the tokamak and the use of a Deuterium/Tritium fuel mixture.[6] Though there will be difficulty in reaching the goals of the fusion program, it is an effort which has been deemed worthwhile by the fusion community and many governments. It is so deemed because of the inherent attraction in the fusion power concept: the production of energy from a fuel virtually limitless (and cheap) with negligible environmental impact.

1.2 Alcator C-Mod

MIT's primary contribution to tokamak research has been the Alcator line of machines. Beginning with the first Alcator, conceived by Bruno Coppi in the early 1970's,[7] the philosophy of the program has been to build high magnetic field, high density, high performance machines which are compact, and hence, low cost. This is accomplished in large part through superior magnetic system design, a benefit of a close association between the Alcator program and the Francis M. Bitter National Magnet Laboratory (which was, until a couple of years ago, located at MIT). The

_____

[6]Perhaps the best known such critique being L.M. Lidsky, "The Trouble with Fusion", Technology Review, Oct 1983, pp. 32-44.

[7]U. Ascoli-Bartoli, et al, "High- and Low-Current-Density Plasma Experiments within the MIT Alcator Programme", Plasma Physics and Controlled Nuclear Fusion Research 1974, Volume 1, pp. 191-203.

Alcator tokamak, and its successor, Alcator C, had peak toroidal magnetic fields of 12 Tesla on axis, the largest of any fusion research device yet built. This approach has many benefits; it allows the reaching of plasma parameters similar to those of larger machines at a fraction of the cost. In a show of perhaps even surpassing its larger brethren, Alcator C was in fact the first tokamak in the world to surpass the Lawson Criterion (the minimum product of density and confinement time needed for breakeven, $n_e\tau_E$ of $6x10^{19}m^{-3}sec$).[8] Alcator C-Mod, the third machine in the line, began regular operation in May 1993.

Cross-sections of C-Mod, displaying the main components of the machine, are shown in figures 1.3 and 1.4.[9] The machine contains an array of copper magnets driven by 10 separate power conversion systems. All magnets are cooled with liquid Nitrogen, a cooling scheme more complicated and expensive than the use of water, for example, but giving the copper six times the conductivity it would have at room temperature. The entire machine is encased in a cryostat for holding the Nitrogen liquid. The 10 toroidal field (TF) magnets, delivering a magnetic field of up to 9 Tesla on axis, contain 120 turns of copper each and have sliding joints at each of the four corners. The sliding joints are unique, allowing movement of the 4 'arms' of the magnet of up to 3 mm. The arrangement allows the magnets to withstand a much larger physical load than would be possible with similarly sized solid magnets. The central ohmic transformer (OH) coils, wound about the TF core, consist of four layers of windings and are designed to produce up to 3 MA of inductive current in the plasma,

---

[8]M. Greenwald, et al, "Energy Confinement of High-Density Pellet-Fueled Plasmas in the Alcator C Tokamak", Physical Review Letters, 53(1984), pp. 352-5.

[9]The discussion that follows on the components and systems of C-Mod is largely condensed from S. Fairfax, et al, "Papers Presented at the IEEE 14th Symposium on Fusion Engineering by the Alcator C-Mod Engineering Staff, Oct. 1991", PFC/JA-91-33.
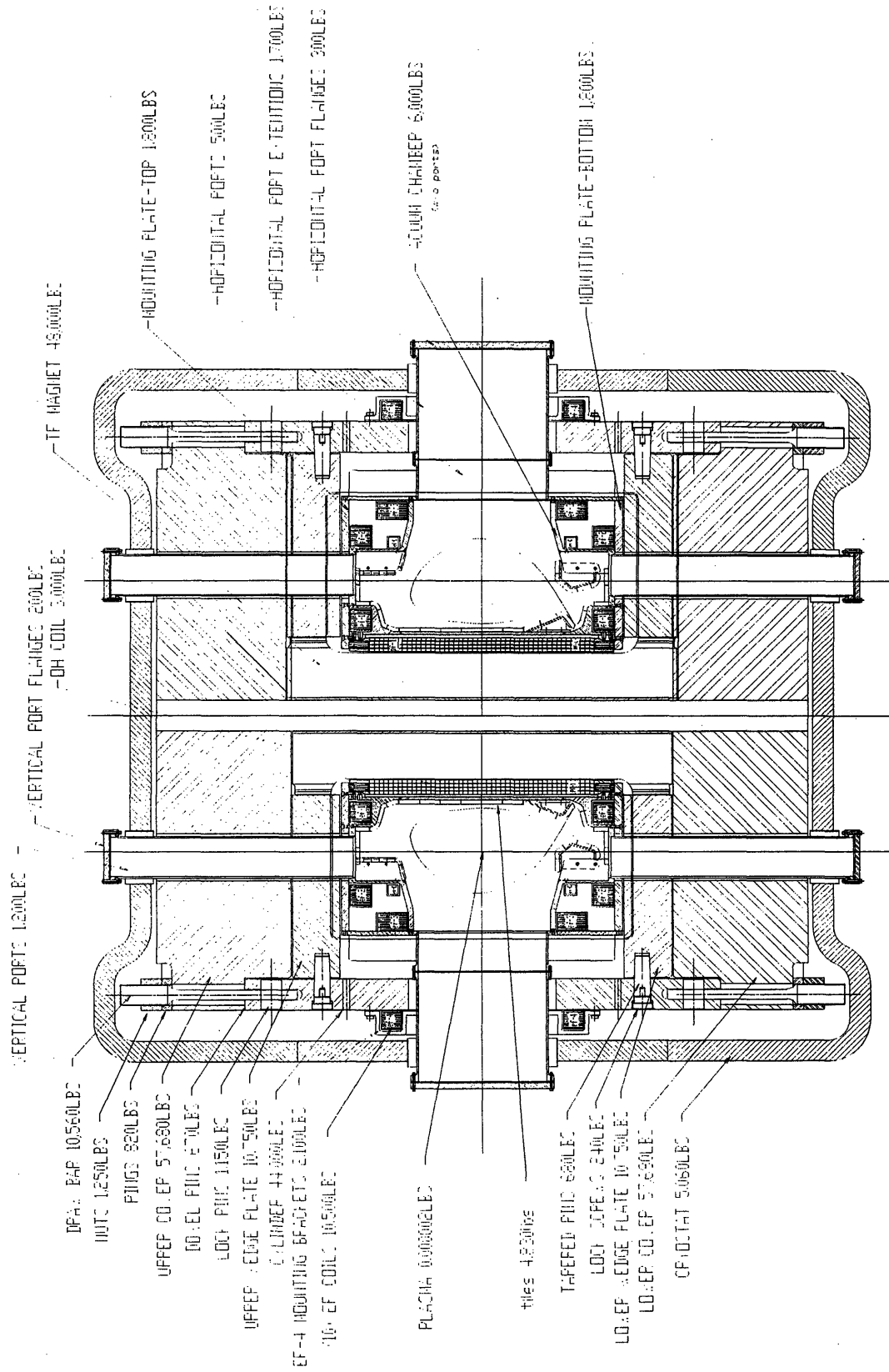
Figure 1.3: Cross-section of the Alcator C-Mod Tokamak
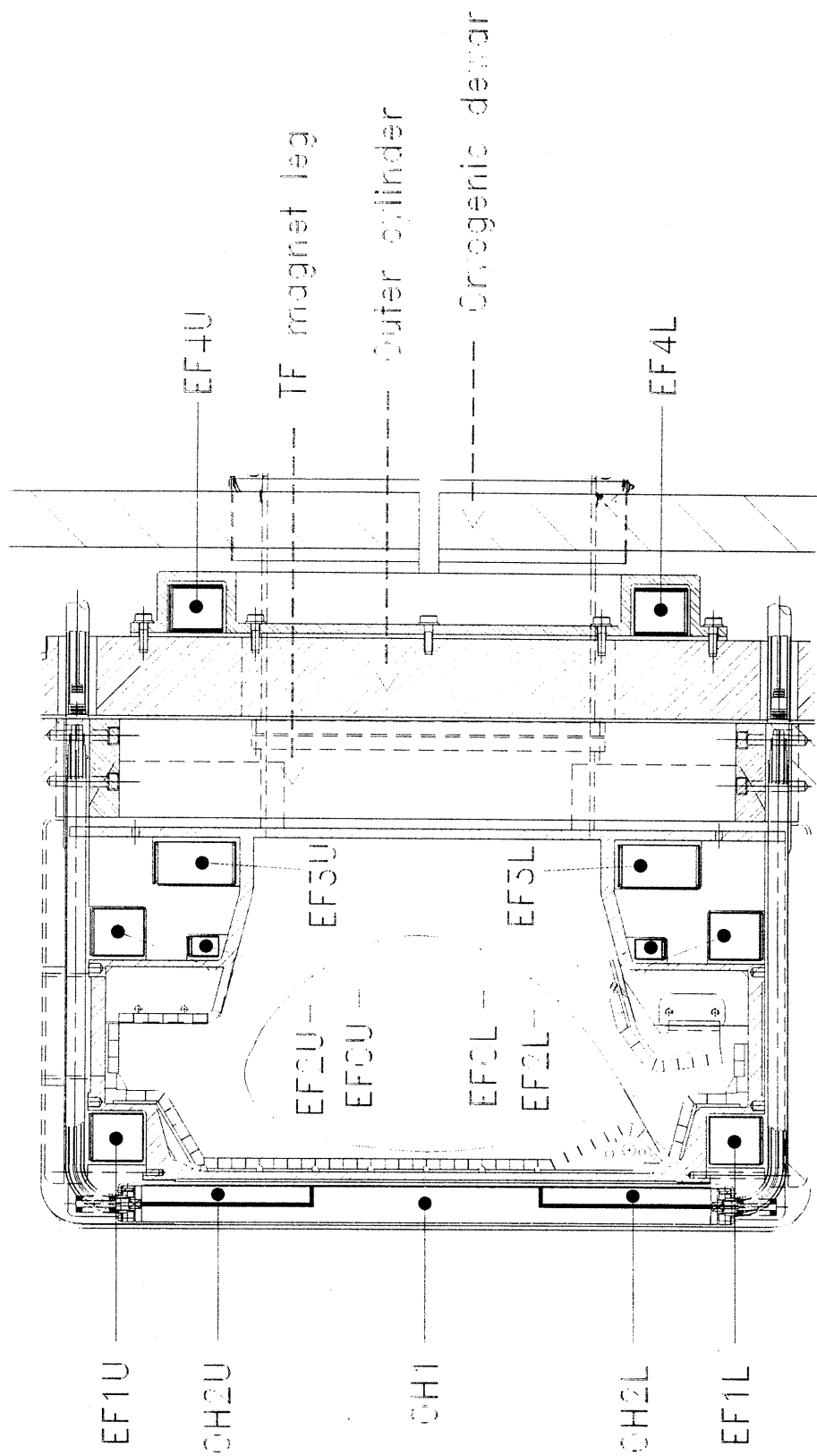
Figure 1.4: Partial Cross-section of the Alcator C-Mod Tokamak

providing up to 7.5 Wb of flux swing. There are 5 pairs of poloidal field (EF) magnets, allowing for complex control and shaping of the plasma. These magnet systems are powered with an alternator and 75-ton flywheel which can store up to 2000 MJ of energy.

The vacuum vessel and superstructure of C-Mod are forged of 304L and 316LN stainless steel respectively. The vacuum chamber contains no electrical breaks, so that large currents flow in it, induced by the magnet systems. While the situation has certain drawbacks, it does have strong attractions, such as mechanical simplicity and passive stabilization of the plasma (from eddy currents produced in the vessel walls). There are 10 horizontal and 20 vertical ports built into the chamber for diagnostic access. The horizontal ports, with a width of about 20 cm, allow for human in-vessel access for installations and repairs. The inside of the chamber is lined with approximately 7000 Molybdenum tiles designed and aligned for withstanding the heat loads incident upon the walls during operation (more on this in the next section). The superstructure, consisting of a central column and top and bottom plates, is designed to contain and support the machine, the magnets in particular. The covers are 66 cm thick and weigh about 30 tons each.

Auxiliary heating (heating in addition to that of the inductive current induced by the OH coils) is provided by fast wave ion-cyclotron RF. Currently, two fixed two-strap dipole antennas provide up to 3.5 MW of heating, with an upgrade to 8 MW planned. Heating is generally done at 80 MHz with a Hydrogen minority species in the plasma of 5-20% concentration. Lower-hybrid current drive (producing non-inductive plasma current as well as plasma heating), is also planned for C-Mod.

Control and data collection for C-Mod is accomplished with hardware logic for personnel protection (eg: access to the machine cell), Allen-Bradley PLC/PC controls for control and data collection on a slow (on the order of seconds) time scale, a CAMAC/DEC workstation system for control and data collection on a fast time scale, and a hybrid digital/analog computer for magnet and gas injection control. The hybrid computer is necessary for real time feedback control of plasma current, position, shape, and density. For response to fast changing plasma conditions, the hybrid was deemed the most cost-effective option. Much unique work has been done on the plasma control system of C-Mod, work necessitated by the C-Mod plasma itself.[10] A Hewlett-Packard optical storage jukebox is used for data archiving.

Table 1.1 gives a listing of the machine design parameters and those that have been achieved.[11] While there are many phenomena relevant to the tokamak and the eventual building of a power reactor for which investigation on a large scale machine is essential, there are others which can well be investigated, in some cases even better investigated, on a smaller machine such as C-Mod. In terms of size, plasma current, and plasma temperature, C-Mod is no match for its larger brethren. In terms of such parameters relevant to the next generation of tokamaks as magnetic field, central density, and parallel scrape-off layer heat flux, C-Mod not only makes the grade, but surpasses most other existing tokamaks by a wide margin. There is also the issue, not shown in this simple table, of

---

[10]I.H. Hutchinson, "Plasma Shape Control: A General Approach and its Application to Alcator C-Mod", PFC/JA-95-4, Feb 1995, Fusion Technology, to be published.

[11]For summaries of some of the results of Alcator C-Mod experiments, see:
  I.H. Hutchinson, et al, "First Results from Alcator C-Mod", Phys Plasmas, 1(1994), pp. 1511-8.
  M. Porkolab, et al, "Overview of Recent Results from Alcator C-Mod", Plasma Physics and Controlled Nuclear Fusion Research 1994, Volume 1, pp. 123-135.

Table 1.1: Parameters of Alcator C-Mod

Parameter	C-Mod Designed	C-Mod Achieved
Major Radius (m)	0.67	---
Minor Radius (m)	0.21	---
Toroidal Field (Tesla)	9.0	8.0
Plasma Current (MA)	3.0	1.2
Aux Heating (MW)	8.0	3.5
Pulse Length (sec)	7.0	1.5
Core n_e (per m^3)	---	1.6×10^{21}
Core T_e (keV)	---	4.0
Parallel SOL Power Flux (MW/m^2)	---	400

flexibility; it is a far simpler task, and far cheaper, to alter C-Mod components than it is to do so on larger machine. This point is expounded here to explain why, while C-Mod is relatively small, and cost much less than the flagship tokamaks, the results from it are unique, interesting, and relevant to the fusion community.

Figures 1.5 and 1.6 give an abbreviated account of a representative C-Mod discharge (960126027 -- 27th shot of the run on 26 Jan 1996). A representative magnetic equilibrium of the shot is shown in figure 1.5, showing the generally used single-null diverted configuration, with inner and outer gaps of about 1.5 cm (the outer limiter installed to protect the RF antennas is not pictured). Figure 1.6 graphs the time histories of selected parameters. The shots usually last 1500 msec (barring disruption), with a plasma current flat top of about 600 msec. 1.1 MA of current and 2 MW of RF power are employed in the shot. The plasma is seen in both so-called L- and H- modes. The H-mode (between .65 and 1.1 seconds) is seen here with a large drop in H-alpha emission, as well as an increase in confinement time, witnessed by the rise in plasma density, temperature, and stored energy. Confinement time enhancement (or 'H') factors in C-Mod have typically been less than 1.4.[12] With boronization,[13] values as high as 2.5 have been achieved.

1.3 The Tokamak Edge

The field of edge physics is concerned with the interaction of the plasma with the walls in which it is contained -- everything outside of the

---

[12]J.A. Snipes, et al, "Characteristics of H-Modes on Alcator C-Mod", Phys Plasmas, to be published.
[13]J. Winter, "A Comparison of Tokamak Operation with Metallic Getters (Ti, Cr, Be) and Boronization", Journal of Nuclear Materials, 176-177(1990), pp. 14-31.
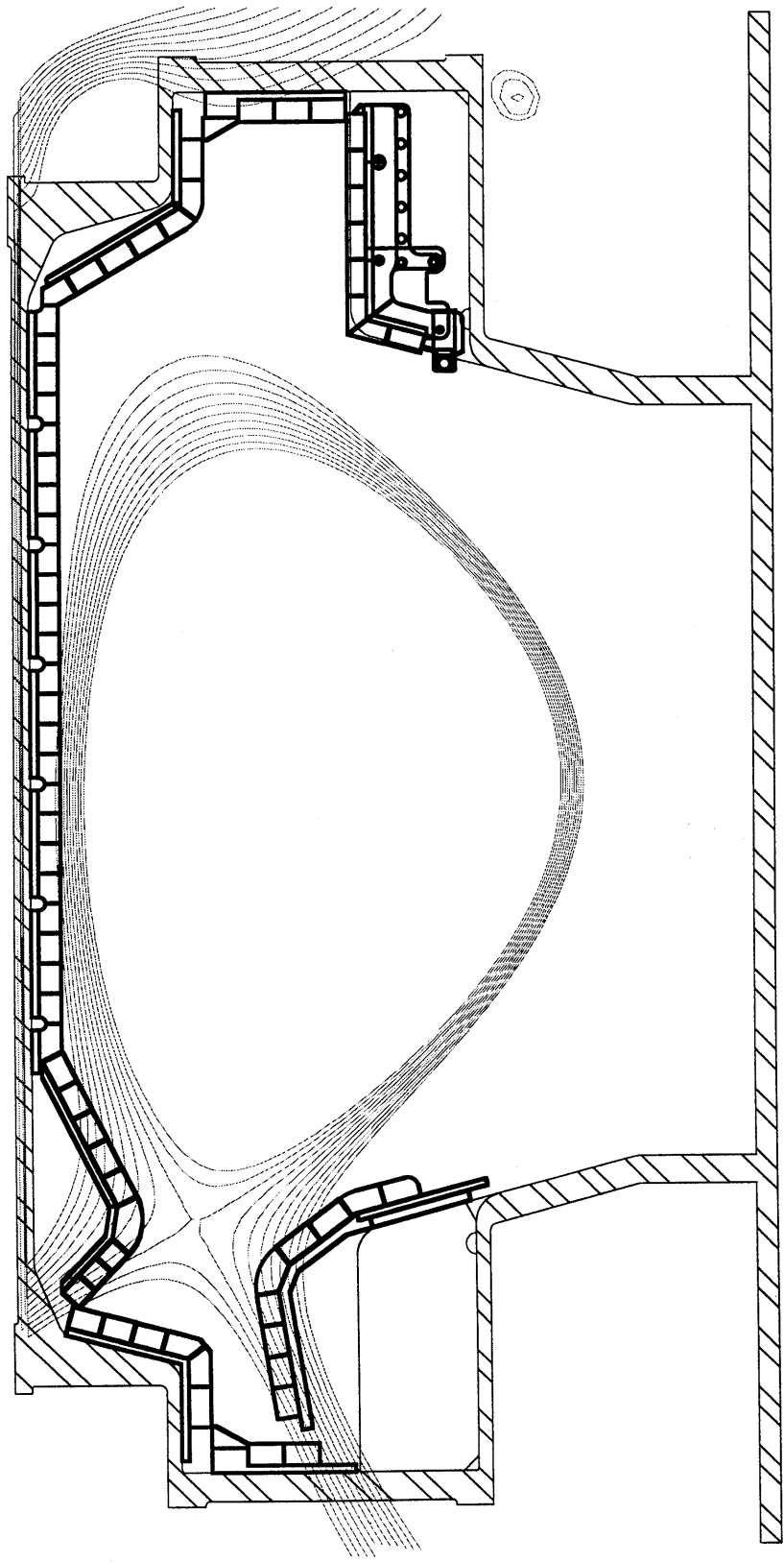
Figure 1.5: Magnetic Equilibrium of Shot 960126027 at .84sec

Figure 1.6: Parameter Time Histories for Shot 960126027

Time into Shot (sec)
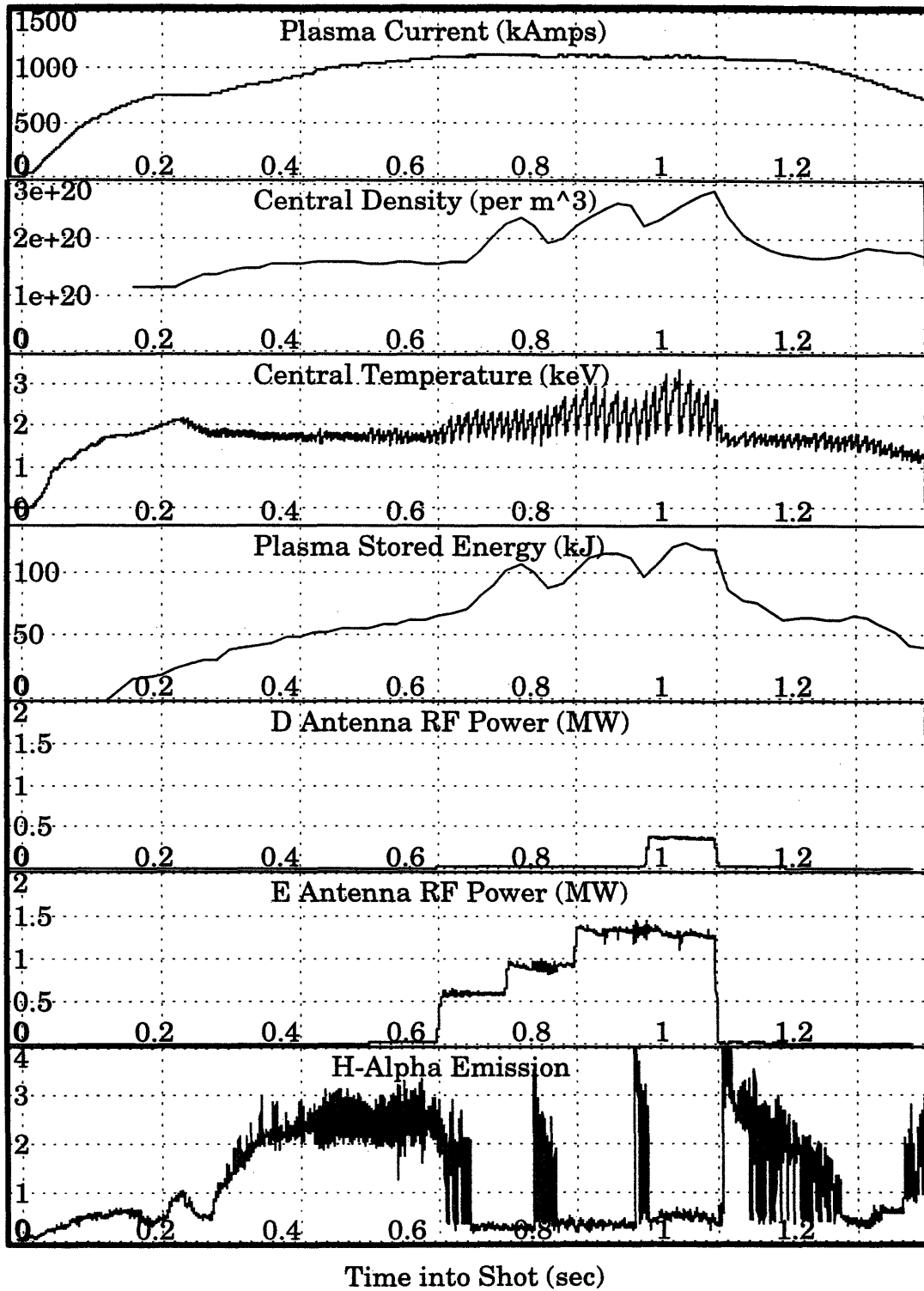
last closed magnetic flux surface (LCFS) of the core. The LCFS is defined as being the outermost set of field lines which terminate upon themselves. Put another way, edge physics is concerned with the area of the tokamak (or other fusion device) in which the magnetic field lines terminate at a solid surface. It is a sub-field of the fusion community which has historically been given scant attention; little effort was put into understanding the plasma edge until rather recently. The situation has altered drastically. The current state of affairs is perhaps best described by the title of an article by Paul-Henri Rebut, the past project director of JET and ITER: "The Key to ITER: the Divertor and the First Wall."[14] Though it is the central plasma in which the all-important fusion reactions occur, it is the edge that in large part determines just how many fusion reactions will be able to occur.

The function of the edge is two-fold: To keep what you want in the central plasma in there (Deuterium, Tritium, energy), and to keep out what you do not want there, namely impurities (Helium, Carbon, Molybdenum, etc.). Figure 1.7 gives the six basic configurations one can use for the edge.[15] These configurations fall into two categories: limiters and divertors. The limiter is conceptually simpler, and easier to implement, allowing the central plasma to come into direct contact with a solid surface, effectively cutting into the plasma to limit its extent. The divertor, almost exclusively implemented in the poloidal scheme, keeps the primary impurity producing surfaces (the divertor plates) at a distance from the central plasma. It accomplishes this feat by using magnetic shaping

---

[14]P.-H. Rebut, et al, "The Key to ITER: the Divertor and First Wall", JET-P(93)06, Jan 1993.
[15]Figure taken from G.M. McCracken and P.E. Stott, "Plasma-Surface Interactions in Tokamaks", Nuclear Fusion, 19(1979), p. 968.

Limiters   Divertors
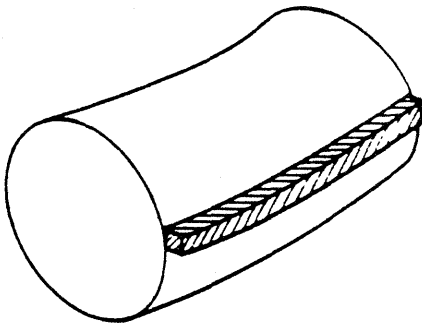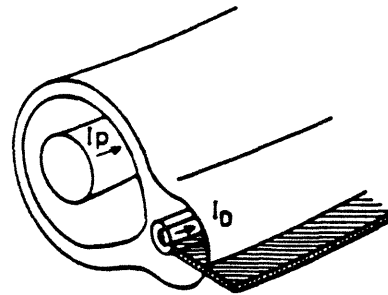
Toroidal limiter   Poloidal divertor
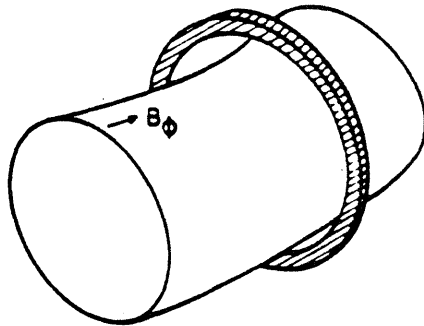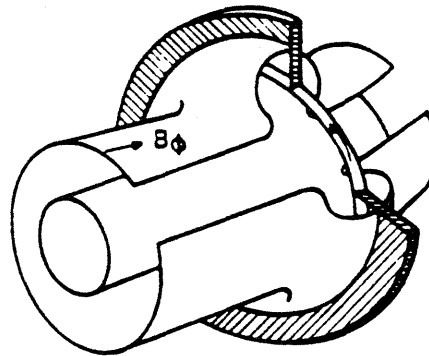
Poloidal limiter   Toroidal divertor
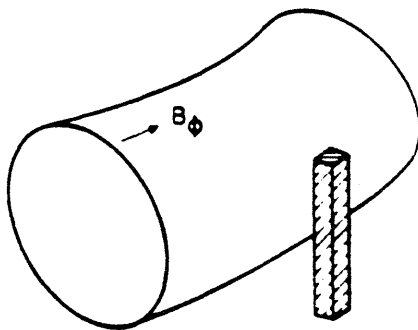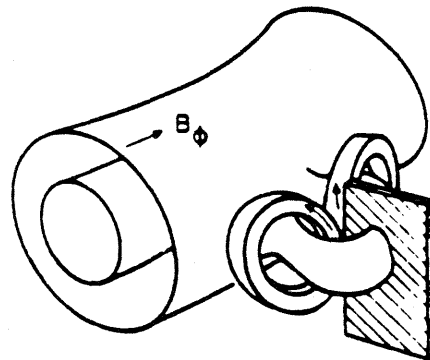
Rail limiter   Bundle divertor

Figure 1.7: Various Edge Configurations

rather than solid surfaces to define the LCFS. Implementation is more complicated than that for a limiter tokamak; the payoff comes in generally cleaner (less impurity ridden) confined plasmas within the LCFS. For this reason, it is divertors which are seen as the future of the tokamak edge and now receive the focus of the community's attention.[16]

The edge, and the divertor scheme in particular, is of increasing importance because of the operating regimes seen for the next generation of tokamaks.[17] Besides contending with the basic two functions discussed above, the edge will also need to contend with the high heat fluxes emanating from the plasma center (in steady state, rather than pulsed, as in today's machines), and with the extraction of the helium that will be produced in fusion reactions. The heat flux problem is simply to make sure that the flux striking solid surfaces is not ruinous, whether by causing the injection of large quantities of impurities, or by causing unacceptable rates of erosion. To deal with this, the heat flux emanating from the central plasma needs to be mitigated through ionic and atomic processes (radiation, charge exchange, etc) before reaching the divertor plates. The divertor (and limiter) scheme pours the heat and particle flux reaching the edge into a narrow column channeled down to the divertor (or limiter) surface. The challenge is to induce enough energy and/or momentum losses in the channel so as to spread out this large flux of heat, whether through selective introduction of impurities or creative control of plasma parameters.

---

[16]For an exhaustive review of divertor work to date see C.S. Pitcher and P.C. Stangeby, "Experimental Divertor Physics", Plasma Phys Control Fusion, to be published.
[17]A recent summary of the work on the divertor for ITER is G. Janeschitz, "The ITER Divertor Concept", Journal of Nuclear Materials, 220-222(1995), pp. 73-88.

1.3.1 The Alcator C-Mod Edge

Alcator C-Mod is a unique vehicle for the investigation of edge phenomena, owing to a closed divertor design (see figure 1.8),[18] and its operating regime. As touched upon in section 1.2, C-Mod has the highest heat flux, magnetic field, and operating density of any existing tokamak, and hence is in many ways the one most relevant for extrapolation to the next generation of machines. The study of the physics of its edge, and the control of it, is vital for expanding the current knowledge base. A divertor design rather similar to that on C-Mod has, in fact, been chosen for ITER.

Figure 1.8 shows a cross section of the C-Mod tokamak, with the molybdenum tiles lining the inner-wall and divertors. The choice of Molybdenum, rather than graphite (used on most machines) or another low-Z (low atomic weight) material, has provided the fusion community with a vehicle for investigating a high-Z first wall. There is a trade-off between high- and low-Z materials for lining a tokamak. Molybdenum tiles eject fewer impurities into the plasma, while Carbon has the advantage of being light, hence causing less damage than a high-Z material, such as Molybdenum, when reaching the central plasma. Since January 1996, C-Mod has been using boronization of the first wall in an effort to accomplish the best of both worlds; attempting, and in large part succeeding, to retain the attractive features of Molybdenum while greatly reducing the quantity of high-Z atoms polluting the plasma.

---

[18]B. LaBombard, et al, "Design of Limiter/Divertor First Wall Components for Alcator C-Mod" in "Papers Presented at the IEEE 14th Symposium on Fusion Engineering by the Alcator C-Mod Engineering Staff, Oct. 1991", PFC/JA-91-33.
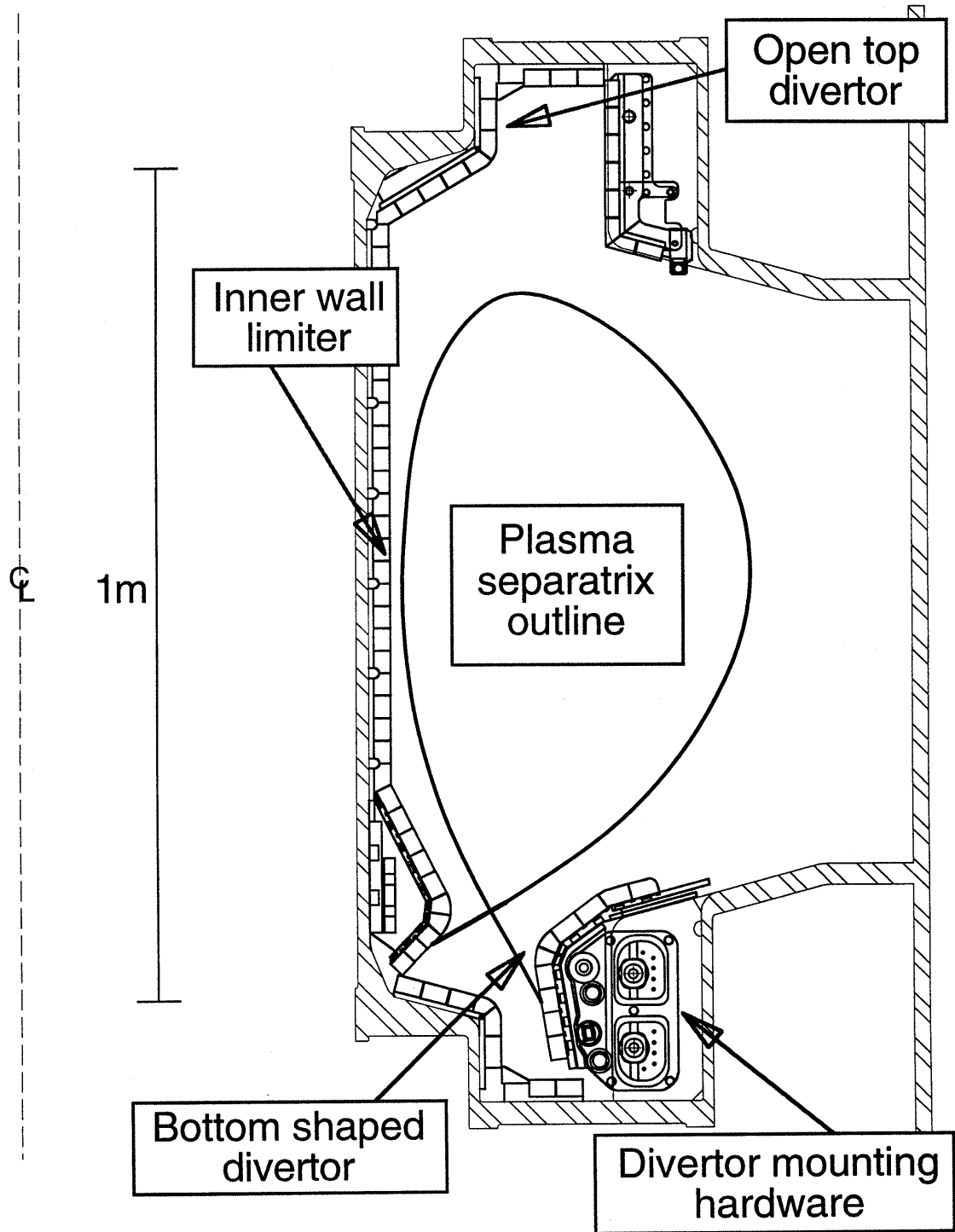
Figure 1.8: C-Mod Plasma Facing Components

Open top divertor

Inner wall limiter

Plasma separatrix outline

1m

Bottom shaped divertor

Divertor mounting hardware

C-Mod does in fact have two divertors, a conventional 'open' divertor on the top, and the unique 'closed' divertor mentioned above on the bottom of the vessel. The closed divertor is designed so that the magnetic field lines strike the divertor plates at a shallow angle, giving net heat flux reduction to the tiles. The design is also such that particles being emitted from the divertor plates head into the so-called private flux region rather than towards the central plasma. The mechanical layout in conjunction with the set of EF coils for shaping allows for 4 basic configurations: single-null lower diverted, as shown in the figure, single-null upper diverted, using the open upper divertor, double-null diverted, with two x-points, utilizing both divertors, and limited, utilizing the inner wall as a rail limiter. Additionally, the lower divertor can be used in three ways, as shown in figure 1.9. The 'vertical target' configuration is that most used, and is in fact the mode for which the divertor target plates were shaped.

The most interesting general result of experiments with the Alcator scrape-off layer (SOL) is the observation of three distinct operational regimes.[19] Which regime exists for a particular discharge is a function of central density, power flux emanating from the central plasma, and impurity content in the edge. Figure 1.10 shows how these three regimes are characterized by the temperature and pressure profiles along a field line in the SOL (the three densities indicated on the top of the figure refer to the volume averaged electron density of the confined plasma). What is shown is the profiles of these three parameters as a function of the distance (ρ) of the field line in question from the LCFS at the machine outer-midplane. The profiles are given at two locations: at the divertor plates and

---

[19]B. LaBombard, et al, "Scaling and Transport Analysis of Divertor Conditions on the Alcator C-Mod Tokamak", Phys Plasmas, 2(1995), pp. 2242-8.

HORIZONTAL
TARGET
(FLAT-PLATE)
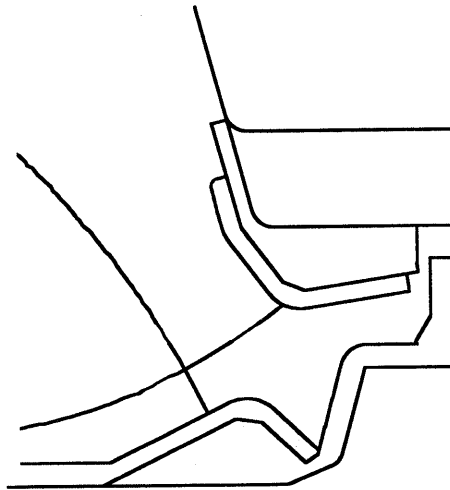
VERTICAL
TARGET
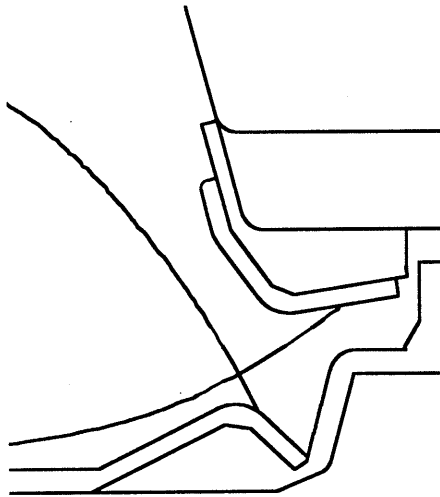
SLOT
DIVERTOR
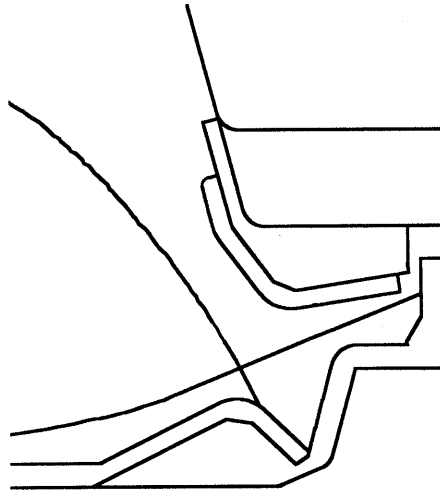
Figure 1.9: Lower Divertor Operating Configurations
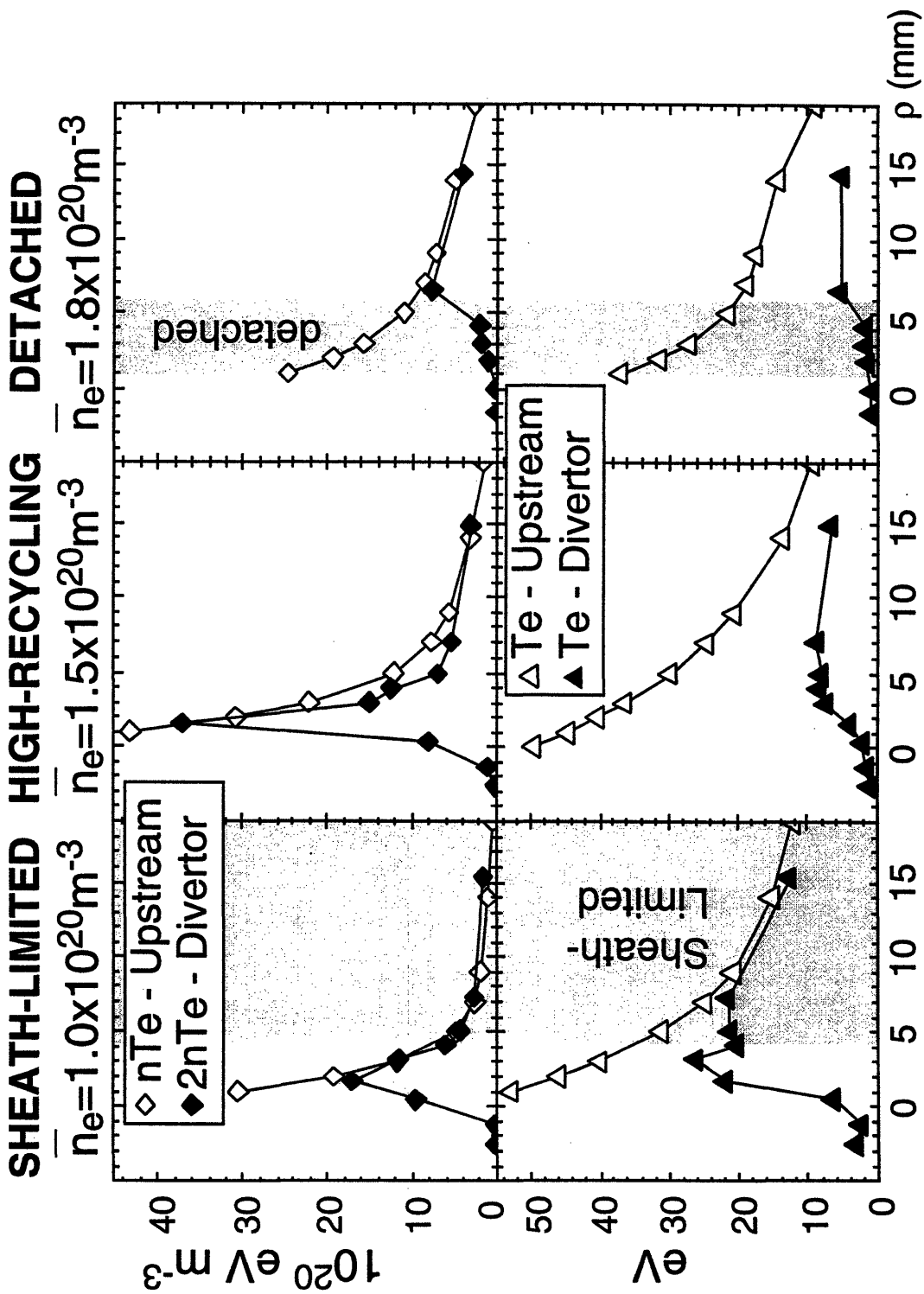
Figure 1.10: Effect of Three Regimes on Plasma Profiles

upstream from the divertor plates, about halfway to the midplane (how these quantities are measured will be discussed in chapter 2). In the first case, the so-called sheath limited regime, plasma pressure, as well as temperature (and hence density) is constant along the field line. The divertor sheath is such to support all the temperature drop on the flux tubes. In the other two regimes the temperature does not stay constant along the field line, rather it sees a large drop between the upstream value and that at the divertor. This is presumably due to the lower temperature along the flux tube, requiring a significant temperature gradient for adequate temperature conduction. In high-recycling, pressure does stay constant however, while in the third, the detached regime, pressure also sees a large drop between the upstream and plate. It is termed 'detached' because the plasma has literally separated from the divertor plate (caused by momentum dissipation in the edge). The divertor region in this third regime is thus cold and has low plasma pressure. When the situation is such that a significant fraction of the heat flux emanating from the core is radiated in the SOL a 'dissipative divertor' has been achieved. This situation usually arises in the detached and high-recycling regimes.[20] These regimes, the physics behind them, and their effect on the central plasma in terms of screening of impurities and plasma transport are of particular interest for reasons mentioned above: the need to have manageable heat loads on the divertor plates in the next generation of tokamaks while simultaneously having the tokamak edge accomplish its other goals (keeping energy and particles in and impurities out of the core plasma).

---

[20]B. Lipschultz, et al, "Dissipative Divertor Operation in the Alcator C-Mod Tokamak", Journal of Nuclear Materials, 220-222(1995), pp. 50-61.

1.3.2 Forces on an Impurity Ion

As touched upon in the last section, impurities play a dominant role in the performance of the edge, and of the central plasma. Their role is primarily a radiative one: the quantity of plasma energy they convert into radiation, and where they do so. This can be both beneficial (radiating energy in the divertor, cutting down on the heat flux hitting the target plates) and deleterious (radiating energy away from the fuel ions in the central plasma). Impurities will always exist in the tokamak plasma, both because they are emitted from the solid surfaces, and because they are often purposely introduced for various purposes. Where they reside and radiate will be determined by their transport.[21] A single particle picture of the impurity ions can be used to get a handle on their what drives their movements about the plasma edge.

The transport of the individual impurity ions along the magnetic field lines will be determined by a number of competing forces, including: (a) the impurity pressure gradient force, (b) friction with the background plasma, (c) electric fields, and (d) background plasma temperature gradient force. There could be, and likely are, others, but these are the four that are generally considered the most significant.[22] The origin and form of each of these forces is considered in turn:

(a) This force is perhaps the most straightforward, arising as long as the impurity density profile along the magnetic field is not uniform, it is simply:

---

[21]For a summary of the study of edge transport on Alcator C-Mod, see: B. LaBombard, et al, "Experimental Investigation of Transport Phenomena in the Scrape-off Layer and Divertor", Journal of Nuclear Materials, to be published.

[22]J. Neuhauser, et al, "Modeling of Impurity Flow in the Tokamak Scrape-off Layer", Nuclear Fusion, 24(1984), pp. 39-47.

$$F_{\nabla p} = -\frac{1}{n}\frac{dp}{dx} \qquad\qquad (1.1)$$

where x is the spatial variable along the field, n is the impurity ion density, and p is the impurity ion pressure (equal to the product of its density and temperature).

(b) Friction with the background ions is conceptually simple. If the impurity ions and the background plasma (generally Deuterium) ions have different velocities, the impurity ions will have a frictional force exerted upon them. This force will be of the form:

$$F_f = m\frac{v_B - v}{\tau_s} \qquad\qquad (1.2)$$

where v_B is the velocity of the background ions, v and m the velocity and mass of the impurity ion, and τ_s the characteristic frictional (or Spitzer 'slowing down')[23] time, i.e. the time scale over which the velocity of the impurity ions is expected to equilibrate with that of the background ions.

The background ions are expected to have a velocity, both from experimental observation, and from basic theory. To illustrate this, consider one of the SOL field lines connecting the inner and outer divertor plates.[24] The electrons, due to their light mass, can be assumed Maxwellian and their density to closely follow the Boltzmann relation:

$$n = n_0 \exp(eV / T_e) \qquad\qquad (1.3)$$

where V is the electric potential, n_0 the electron density at the point where V=0 (arbitrarily defined to be at the bulk plasma potential), and T_e is the electron temperature (in energy units). The plasma is assumed to be quasineutral, i.e. that the ion density (assume a singly charged background

[23]L. Spitzer, Jr., Physics of Fully Ionized Gases, New York: Interscience Publishers, Inc., 1956, pp. 76-81.
[24]The ensuing derivation follows that in section 3 of P.C. Stangeby and G.M. McCracken, "Plasma Boundary Phenomena in Tokamaks", Nuclear Fusion, 30(1990), pp. 1225-1379.

plasma ion species) will follow the electron density (n). For the ions, equations for conservation of particles and momentum can be written:

$$\frac{d}{dx}(nv) = S_p \tag{1.4}$$

$$nm_i v \frac{dv}{dx} = -\frac{dp_i}{dx} + enE - m_i v S_p \tag{1.5}$$

where $E=-dV/dx$ is the electric field, $p_i=nT_i$ the ion pressure, and S_p is a particle source term. This source term can be considered general, including both cross-field diffusion and ionization. Notice that any momentum source is neglected, an assumption known not to be always correct, but an assumption good enough for the sake of this illustration. If we define the sound speed and Mach number:

$$c_s \equiv \sqrt{\frac{T_e + T_i}{m_i}} \tag{1.6}$$

$$M \equiv \frac{v}{c_s} \tag{1.7}$$

and make the convenient assumption of isothermal ions (T_i constant), we can combine the equations to obtain:

$$\frac{dM}{dx} = \frac{S_p}{nc_s} \frac{(1+M^2)}{(1-M^2)} \tag{1.8}$$

Note that as M approaches 1 or -1 (ion velocity approaches the sound speed), the derivatives go to infinity, a breakdown in the equations resulting from a breakdown in the quasineutral assumption. If one were to work through the equations for the plasma near the divertor plates on this field line (the 'sheath equations'), one would find that this condition is reached very close to the plates. The Mach number, equal to 1 at one plate, -1 at the other, reduces in absolute magnitude as one moves away from the plate, reaching zero somewhere in between, at what is called the stagnation or symmetry point. To a first approximation, one would expect to find the symmetry

point roughly half-way between, the exact shape of the Mach number profile depending upon the shape of the source particle source function (S_p).

In figure 1.11(a), equation 1.8 is solved for a constant particle source using the boundary conditions that the Mach number is unity (and minus unity) at the plates, and zero half-way in between. It is a very crude approximation, but one which gives a solution which provides a qualitative handle on the shape of the background plasma velocity profiles. Even without the constant particle source approximation, equation 1.8 is still not strictly valid of course, but it does show that ion flows, and hence a frictional force on impurity ions, can be reasonably expected.

(c)   To see that an electric field along the magnetic field line is expected, one can solve the above equations for velocity in terms of Mach number,

$$V(M) = -\frac{T_e}{e}\ln(1+M^2) \qquad (1.9)$$

meaning that as long as one has a varying ion velocity, one will have an electric field. Using the constant particle source solution for Mach number plotted in figure 1.11(a), the resulting potential profile is given in figure 1.11(b). It shows the potential to go to zero (the 'bulk plasma potential') as the Mach number approaches zero, and to go to $-.69T_e/e$ at either plate. The electric field this causes will point away from the stagnation point, towards each plate. The force due to this field on the impurity ion will simply be (where Z is the ion charge state):

$$F_E = ZeE \qquad (1.10)$$

(d)   The background plasma temperature gradient force, takes the form

$$F_{\nabla T} = \alpha_e \frac{dT_e}{dx} + \beta_i \frac{dT_i}{dx} \qquad (1.11)$$

Figure 1.11: Edge Profiles Along Field Line with Constant Source
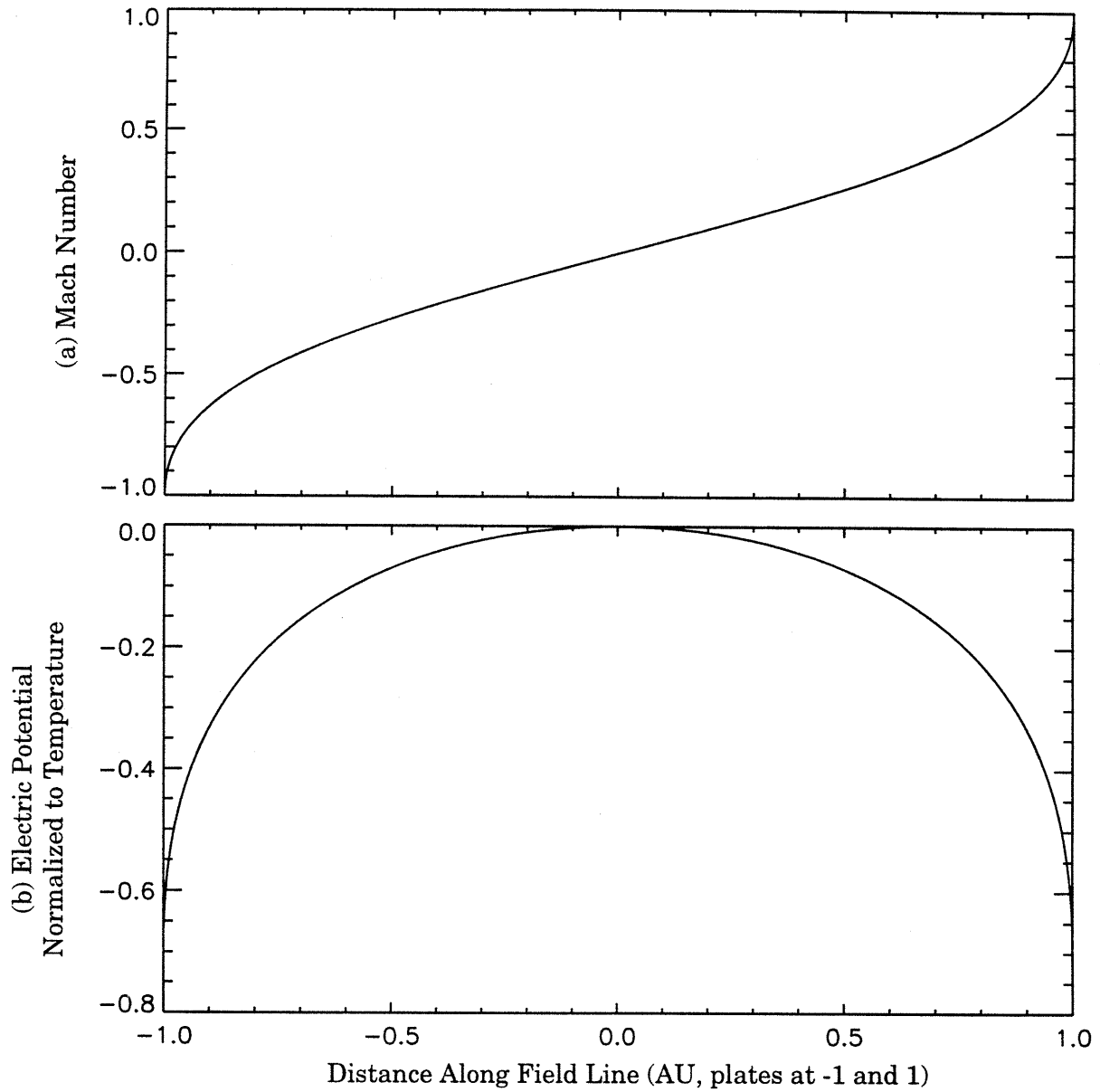
where α_e and β_i are constants. The force points up the gradient of temperature, somewhat counterintuitively. Though isothermal ions were assumed above, and though uniform temperatures along the field will be assumed in much of this thesis, both temperatures will generally have gradients, and this force will, in general not be negligible (though it will be considered such in later chapters).

Summarizing the forces driving impurity transport parallel to the magnetic field, one arrives at the equations:

$$F = F_{\nabla p} + F_f + F_E + F_{\nabla T} \tag{1.12}$$

$$F = \frac{1}{n}\frac{dp}{dx} + m\frac{v_B - v}{\tau_s} + ZeE + \alpha_e \frac{dT_e}{dx} + \beta_i \frac{dT_i}{dx} \tag{1.13}$$

The transport of the ions along the field will be determined by these competing forces. What one would like is for these forces to balance such that impurity ions, produced by plasma contact with the tokamak walls, or introduced purposely, will become entrained in the divertor, i.e. get pushed down into the divertor and stay there, wherever they appear. If this is the case, the core impurity radiation is kept to a minimum and the SOL impurity radiation to a maximum, as desired. As was seen above, the background electric field, and background plasma velocity will generally point towards the nearest solid surface on the flux surface, pushing the impurity ion in that direction. The background temperature gradient terms will push the ions in the opposite direction. The temperature gradient term is dependent upon the impurity ion profile (if the majority of the impurity ions are entrained in the divertor, for example, it will point away from the divertor plate).

Perpendicular to the field line, the transport of the impurity ions will in large part be determined by anomalous diffusion and drifts (anomalous meaning they cannot be derived from basic theory at present and are

measured experimentally). In its most general form the anomalous diffusion contribution to perpendicular ion velocity will be in the form:

$$\underline{v}_\perp = -\frac{1}{n}\underline{\underline{D}}_\perp \cdot \nabla_\perp n \qquad (1.14)$$

where n is the impurity ion density. There are however ion drifts to be expected which can be explained analytically. These arise from forces exerted upon the ions perpendicular to the magnetic field. These forces give rise to perpendicular drift velocities expressed by:[25]

$$\underline{v}_d = \frac{\underline{F} \times \underline{B}}{ZeB^2} \qquad (1.15)$$

such that the induced velocity is perpendicular to both the direction of the magnetic field and that of the force. Three examples of such drifts expected to contribute to cross-field impurity ion transport are the ∇B drift, the curvature drift, and the electric field drift.

The ∇B drift arises from small differences in the magnetic field over the extent of a particle's Larmor orbit. With the ion experiencing different magnetic fields over its trajectory, if one averages over that orbit, a net force is found. It is of the form:

$$\underline{F}_{\nabla B} = -\frac{Zer_L v_\perp}{2}\nabla B \qquad (1.16)$$

where r_L is the ion's Larmor radius, and v is its perpendicular velocity (along its gyro-orbit). Since the magnetic field decreases with increasing major radius in a tokamak, this force will point outward, giving a downward ion drift for a clockwise magnetic field (looking down), and an upward ion drift for a counterclockwise field (the drifts going oppositely for electrons).

---

[25]F.F. Chen, Plasma Physics and Controlled Fusion, Volume 1, New York: Plenum Press, 1984, Chapter 1.

Centrifugal force felt by the impurity ions as they travel along the magnetic field line gives rise to the curvature drift. The force will be of the form:

$$\underline{F}_R = m v_\parallel^2 \frac{\underline{R}_c}{R_c^2} \tag{1.17}$$

where R_c is the radius of curvature of the magnetic field. Because the magnetic field varies as $1/R_c$ in a tokamak (meaning the ∇B drift will be of similar form to the curvature, and be in the same direction), equations 1.16 and 1.17 are generally combined and considered together to express a 'curved vacuum field drift'.

The electric field force is as it was in equation 1.10:

$$\underline{F}_E = Ze\underline{E}_\perp \tag{1.18}$$

A radially directed electric field is in fact measured in tokamak SOL's, in C-Mod with the scanning probe (see section 2.2). These electric fields hence give rise to poloidally directed drift velocities. To see why this would theoretically be expected, one can take the inverse of the Boltzmann relation (equation 1.3), to obtain

$$V = \frac{T_e}{e} \ln(\frac{n}{n_o}) \tag{1.19}$$

where potential is chosen to be zero at the plate and n_o represents the value of density at the plate. Because the plate is a conductor, the electric potential over it will be uniform, hence the plate potential on each field line will be the same (here set to zero). Equation 1.19 is therefore applicable across field lines. Going radially outward from the core plasma, the temperature gradient will generally dominate any gradient in the log of the density ratio. This leads to the approximate expression for the resulting electric field,

$$\underline{E}_\perp \approx -\frac{1}{e}\nabla_\perp T_e \ln(\frac{n}{n_o}) \tag{1.20}$$

This field will generally point radially outward, giving rise to a poloidal drift.

1.4 Thesis Motivation and Outline

The motivation of the work presented in the following chapters is the construction of a simple edge diagnostic technique which can contribute to the understanding of SOL transport in a unique way. The primary experiments of the programme are basic: the observation of impurity gas injection into the edge with a CCD camera. With this simple method however, background plasma flow direction is shown rather vividly in locations otherwise inaccessible (or problematic to reach) with other diagnostics. Through modeling, the quantification of this plasma flow as well as the background plasma temperature and impurity ion poloidal drift velocity can be extracted. This can lead to a wealth of information which would otherwise be difficult to directly obtain. Though somewhat similar work has been performed elsewhere,[26] it has been less ambitious or has had other focuses. To round out the discussion of gas injection

---

[26]Examples include:

A.G. Hwang, "The Transport of Impurities in the Boundary Layer of the Joint European Torus (JET)", Doctoral Thesis, University of Toronto Institute for Aerospace Studies, Oct 1994.

U. Kögler, et al, "Experimental Studies and Modeling of Layer Deposition on Limiter Surfaces by Local Gas Injection in TEXTOR", Proceedings of the 22nd European Conference on Controlled Fusion and Plasma Physics, Volume IV, 1995, pp. 281-4.

G.F. Matthews, et al, "Impurity Transport at the DIII-D Divertor Strike Points", Proceedings of the 18th European Conference on Controlled Fusion and Plasma Physics, Volume III, 1990, pp. 229-32.

G.M. McCracken, et al, "A Study of Impurity Transport in the Plasma Boundary of TEXTOR using Gas Puffing", Journal of Nuclear Materials, 176-177(1990), pp. 191-6.

C.S. Pitcher, "Tokamak Plasma Interaction with Limiters", Doctoral Thesis, University of Toronto IAS, 1987.

C.S. Pitcher, et al, "Carbon Impurity Transport around Limiters in the DITE Tokamak", Journal of Nuclear Materials, 162-164(1989), pp. 337-42.

experiments, the global screening properties of the edge deduced from such experiments is briefly discussed as well.

The outline for the remaining chapters is as follows:

Chapter 2 discusses some of the diagnostics employed on Alcator C-Mod with emphasis on those tools most critical to the work of this thesis.

Chapter 3 presents the basics of impurity screening and Deuterium fueling experiments performed on C-Mod, with a brief analysis of the results observed.

Chapter 4 provides an overview of the primary experiments of the programme: the observation of 'plumes' produced in the region of impurity puffs.

Chapter 5 describes the fluid model employed to interpret the plumes observed, and discusses a benchmarking of the model against a more complete Monte Carlo code.

Chapter 6 employs the fluid model outlined in chapter 5 to interpret and extract numerical results from the plumes.

Chapter 7 summarizes the findings of the experimental program and discusses how the work could be improved and extended.

Chapter 2
Diagnostics

From the beginning of the fusion endeavor, the need to create tools for accurately measuring plasma properties was apparent. The very high temperatures and low densities associated with the plasma state make measuring its properties challenging; one cannot measure a 12 million degree gas with a mercury thermometer. This chapter gives an overview of some of the diagnostics used on Alcator C-Mod to measure the plasmas it creates. The first section describes the diagnostic which provides the backbone of this thesis, the second the two diagnostic systems which play the primary supporting role, the third gives a brief description of other diagnostics which this thesis makes use of to varying degrees.

2.1 The NINJA/Culham Diagnostic

As briefly stated in chapter 1, this diagnostic injects gases into the plasma and uses a CCD camera to record the emission pattern produced in the SOL about the injection point. Figure 2.1 shows the basic layout, with two camera views observing the array of impurity injection points. The two components of the diagnostic, the system used for delivering the gas to the desired location and that for recording the impurity emission, are described

Eyes indicate
Camera Views

Arrows indicate
Puff Locations
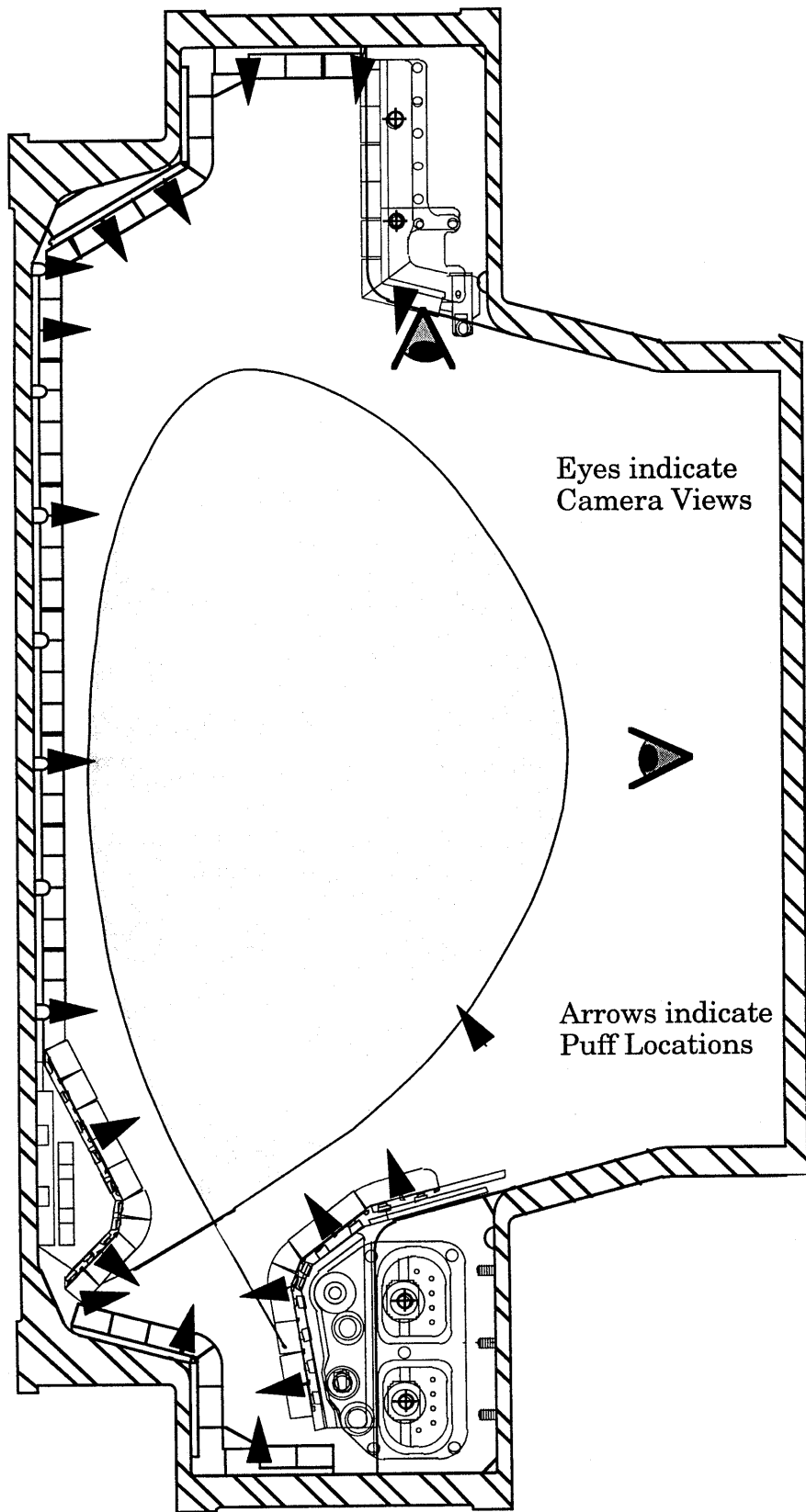
Figure 2.1: Layout of the NINJA/Culham Diagnostic

separately in the following sections. While these two systems used in conjunction provide the basis of the experimental program of this thesis, experiments are also described in the next chapter which use the first (NINJA) on its own.

2.1.1 The Neutral gas INJection Array (NINJA)[1]

NINJA is a flexible gas delivery system for the Alcator C-Mod edge. Impurities or fuel gas can be puffed at 33 different locations (the 20 poloidal locations shown in figure 2.1 at one toroidal location, 9 poloidal locations at another toroidal location, and single capillaries at 4 other). This can be done through single capillaries or through a number of capillaries in tandem in measured quantities ranging from .1 torr-litre to more than 100 torr-litres. The system complements the primary C-Mod gas system, which uses piezo-electric valves located on the outboard of the vessel to deliver fuel or impurities.[2] The piezo system gives fast time response (on the order of milliseconds), allowing for real-time feedback control on gas injection. NINJA, using pneumatic valves and capillary tubes, has slower time response (on the order of hundreds of milliseconds); indeed, gas injection quantity needs to be decided upon before the shot. What NINJA does provide is a wide range of injection locations.

Figure 2.2 gives a schematic of the NINJA system. It shares a gas mixing apparatus with the primary C-Mod gas system to eliminate duplication in equipment and allow for integration. There are a number of aspects to point out about the NINJA 'plenum'--the volume located between

---

[1]This section is an updated version of D. Jablonski, et al, "Capillary Gas Injection Experiments on Alcator C-Mod", <u>Bulletin of the APS</u>, 39(1994), Nov, 6P29.
[2]R. Childs, et al, "Design, Control, and Operation of the Vacuum and Gas System for Alcator C-Mod", Proceedings of the 15th IEEE/NPSS Symposium on Fusion Engineering, Volume 2, 1994, pp. 1051-4.
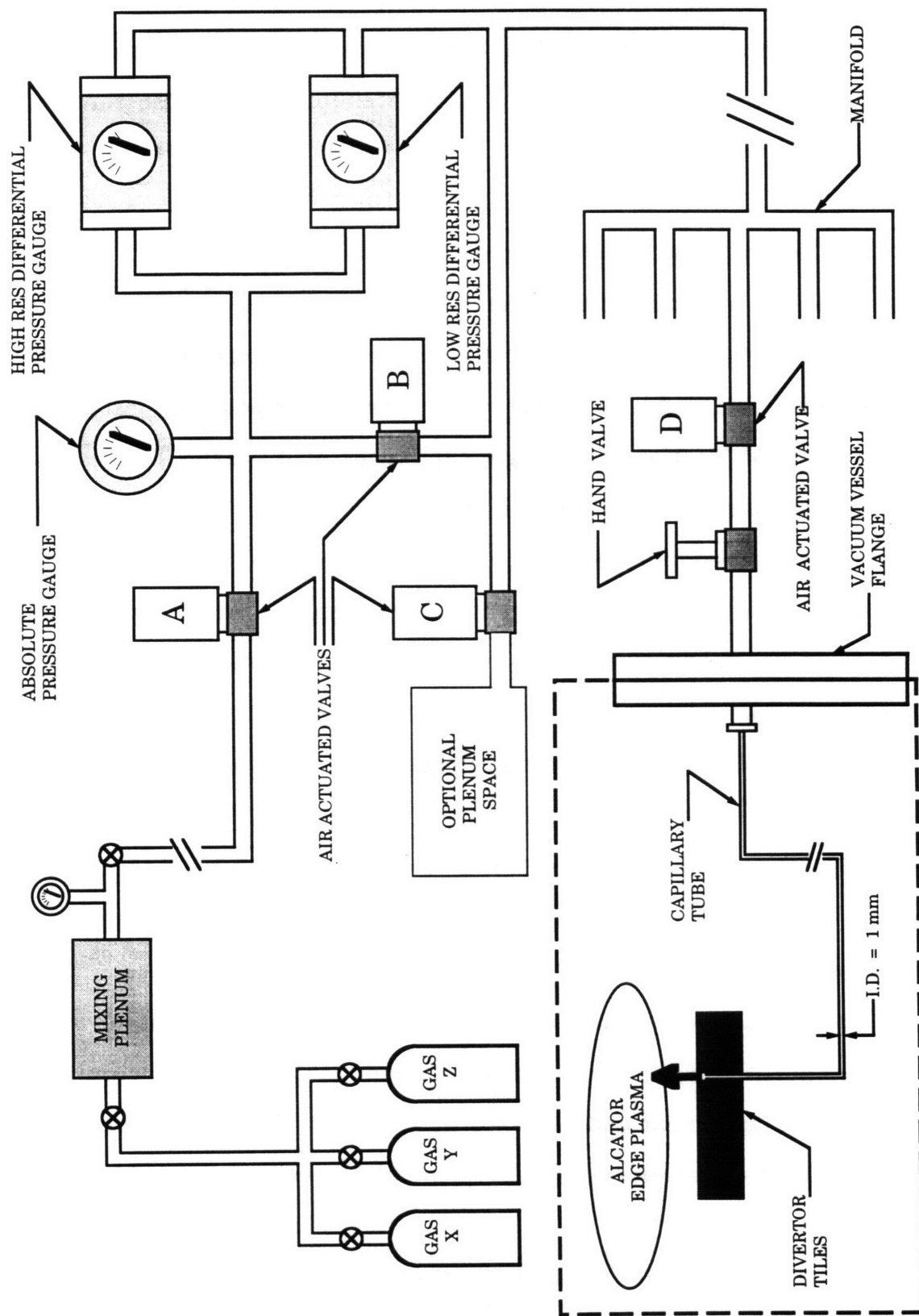
Figure 2.2: Schematic of the NINJA System

HIGH RES DIFFERENTIAL PRESSURE GAUGE

LOW RES DIFFERENTIAL PRESSURE GAUGE

ABSOLUTE PRESSURE GAUGE

MANIFOLD

HAND VALVE

AIR ACTUATED VALVE

VACUUM VESSEL FLANGE

AIR ACTUATED VALVES

OPTIONAL PLENUM SPACE

A

B

C

D

MIXING PLENUM

GAS X

GAS Y

GAS Z

CAPILLARY TUBE

I.D. = 1 mm

ALCATOR EDGE PLASMA

DIVERTOR TILES

the pneumatic valves labeled B and D. Normally, this plenum is 277 ml in volume. When valve C is opened, adding the 'Optional Plenum Space', the volume increases to 1260 ml. Roughly speaking, the smaller volume is employed for small gas injections, the larger volume for large injections. When gas is injected, valve B is closed so that the change in pressure in the plenum, which when multiplied by the plenum volume in use gives the quantity of gas injected, is measured by the differential (MKS Baratron type 221B) pressure gauges shown in the figure. The low resolution gauge measures up to 100 torr in pressure change, the high resolution up to 10 torr. Having both gauges as well as the variable plenum size gives the system the ability to measure a wide range of injection quantities. Another gauge (MKS Baratron type 121A), measures the absolute pressure level in the plenum. The plenum feeds into a manifold which goes to the individual capillaries. Each capillary has a pneumatic valve to control delivery through the tube. A hand valve for each capillary is located at the vacuum flange to allow for valving off the NINJA plenum for maintenance work without breaking vacuum in the vessel. Each capillary, going from the C-Mod flange up to the injection location, is about 3m long and has a 1 mm I.D. The hand valves are Nupro B series bellows type and the pneumatic are Nupro BN series miniature bellows type. The pneumatic valves are driven with about 80 psi air pressure delivered by 12 volt Burkert solenoid valves.

The slow time response of the system has two causes: the use of air driven pneumatic valves (with a response delay of about 70 msec), and the long thin capillary tubes though which the gas need travel. This second time delay is dependent upon the gas pressure in the plenum, ranging from milliseconds when the plenum pressure is on the order of

atmospheres to hundreds of milliseconds when the plenum pressure is at tens of torr. Pneumatic valves were chosen because of their relatively low cost; the response time gained by piezo valves was not deemed worthwhile when the flow characteristics of the capillaries limited any quickening of response that might be made. Figure 2.3 shows parameter traces for a Nitrogen injection calibration shot (no plasma, gas in vessel entirely due to the puffing). The valve on a capillary was pulsed for 100 msec at 0.0 sec. The two delays are seen in these plots. The 'Gas Injected', as measured by the high resolution differential gauge, does not begin to show response until about 100 msec (the delay resulting primarily from the mechanical delay of the air valve). For the gas to appear in the vessel takes even longer, as shown in the vessel pressure scope. Additionally, while the differential gauge shows the gas being ejected from the NINJA plenum rather quickly, the vessel pressure gauge shows that the gas spends a long time making its way through the tube, both in terms of the injection commencement and the 'dribbling' of the gas out of the tube which ensues for a time scale much longer than that of the valve pulse. What effectively happens when the pneumatic valve is pulsed is that the volume in the hand valve fills up (volume of about 5 cm^3), then acts as a repository for gas feeding into the capillary even once the pneumatic valve is shut. Gas will continue to dribble into the chamber until all present in this trapped volume and in the capillary itself has been evacuated.

One can use viscous flow theory to show that this injection behaviour is endemic to the system. Combining the Poiseuille equation with

Figure 2.3: Nitrogen Injection Calibration Shot (No Plasma)

NINJA Plenum Pressure (torr)

Output from NINJA Plenum (torr-litres)

Gas Pulse

Vessel Pressure (mtorr)

Gas Pulse

.... Mechanical Valve Delay
- - - - Capillary Flow Delay

Time (sec)
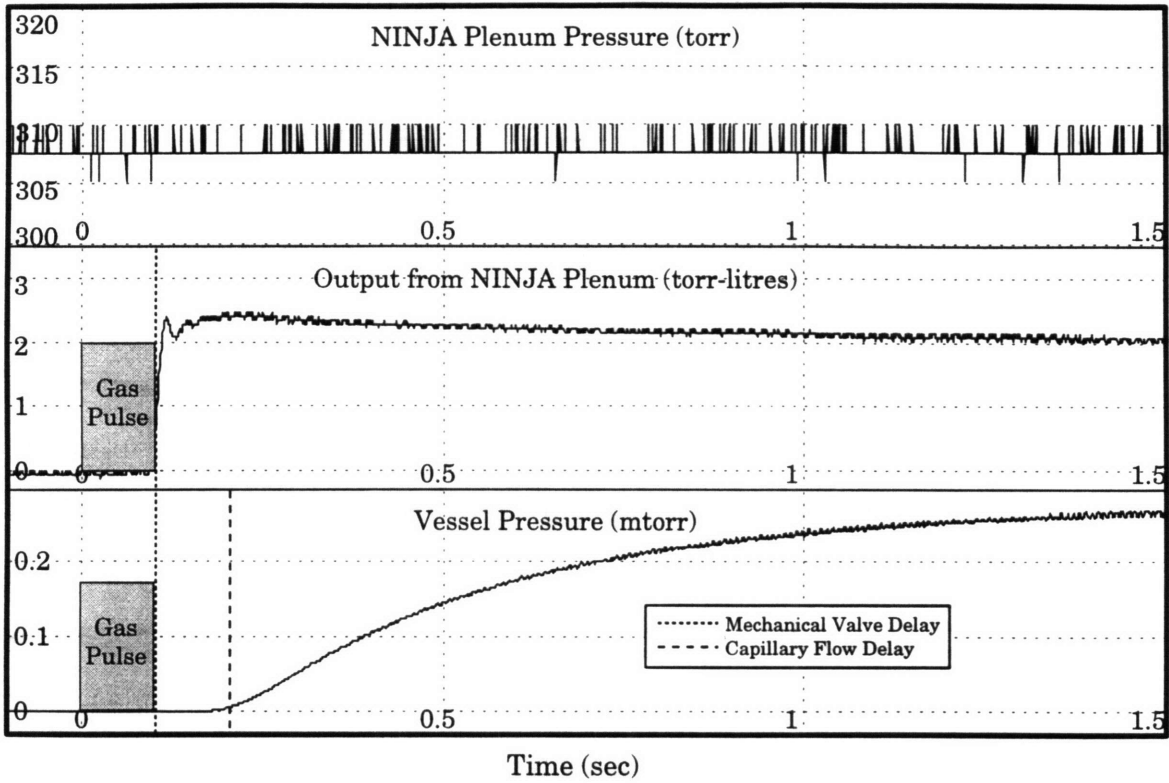
Figure 2.4: Modeling of a Nitrogen Injection

.5s

1.0s

.005s   .035s   .1s   .25s

Pressure (torr)

Distance along Capillary (m)
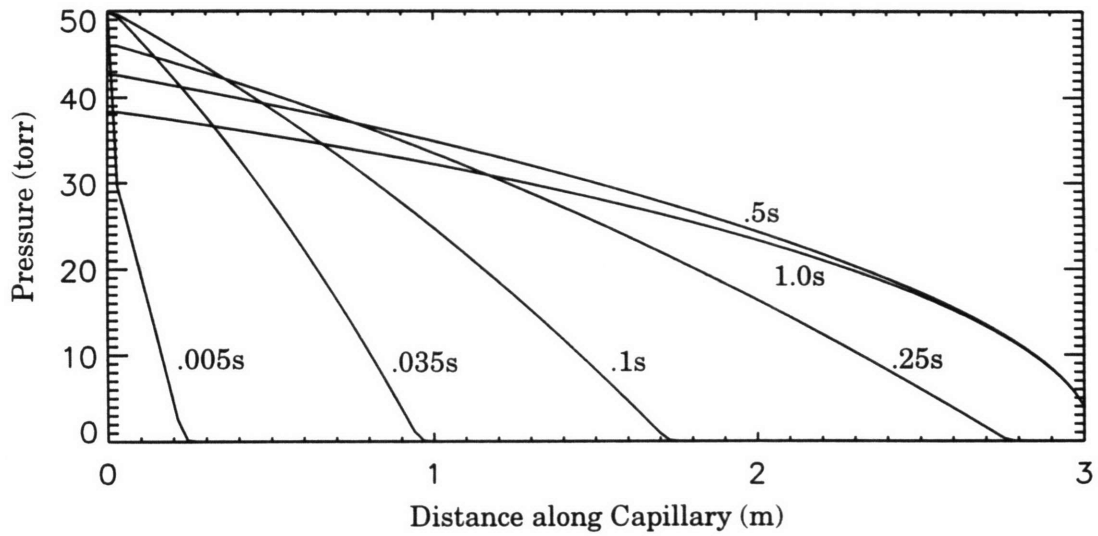
continuity gives the nonlinear diffusion equation:[3]

$$\frac{\partial p(z,t)}{\partial t} = \frac{r^2}{16\eta} \frac{\partial^2 p(z,t)^2}{\partial z^2}$$

(2.1)

where p is the gas pressure, r the radius of the capillary, η the dynamic viscosity of the gas, t is time, and z is the distance long the capillary. This can be solved with the pressure boundary conditions at the plenum and in the vessel, and the initial conditions of the pressure all along the capillary being the same as that in the vessel. Including molecular flow appropriately in solving for the capillary pressures makes little difference in the solutions. Figure 2.4 shows the pressure profiles at a number of different times found by solving the above diffusion equation. These solutions are for a plenum pressure of 50 torr of Nitrogen and a valve pulse of 100 msec begun at 0.0 sec. For this case, one can see that it takes about 300 msec for the gas to reach the end of the tube. Once the gas begins entering the plasma chamber, it dribbles out very slowly, as witnessed here by the small difference in the pressure profile of the capillary between .5 and 1.0 seconds.

It should be noted that such modeling can in theory be employed to calculate the time history of the gas being injected by NINJA into the vessel for a given shot. Because of the difficulty in obtaining the exact value of some constants (mechanical delay of the valve, capillary lengths, trapped volume in the hand valve, etc), the injections are instead calibrated using shots with no plasma. At the end of a run in which NINJA is used, the injections are reproduced without plasmas, yielding the time history of the injection with the use of an in-vessel pressure gauge. An example of this is given in figure 2.3.

---

[3]H. Lamb, Hydrodynamics, Cambridge, UK: the University Press, 1895, chapter XI.

2.1.2 Plume Imaging

The system for imaging the emission created in the vicinity of the puffing location is composed of three parts: the first for gathering the image and optically filtering it appropriately, the second for the conversion of the optical images to a video signal, the third for archiving the images. It should be noted that while the second is more or less dedicated to plume imaging, the first and third are shared, being used primarily for spectroscopic diagnostics. The complete system is diagrammed in figure 2.5.

At each of the locations indicated in figure 2.1, a C-mount camera lens projects an image of the plasma onto a coherent fiber bundle. The bundle then leads to a quartz window, taking the image outside the machine to the CCD camera. The fiber optic intermediary between the view and the camera is installed for a number of reasons, space constraints and the avoidance of neutron and gamma radiation distortions on the CCD being examples (the C-Mod vessel provides shielding for the CCD). Optical interference filters, located between the quartz window and the CCD, are used to isolate wavelengths desired to be viewed. Six filters are used in the plume experiments: Carbon-II (515 nm peak transmission wavelength, 20 nm bandpass), C-III (465, 3.5), Nitrogen-II (463, 1.5), N-III (451, 1.5), Helium-I (588, 3), He-II (469, 2), and H-Alpha (656, 4). The filters are installed on filter wheels which allow remote selection between 6 filters at a time.[4]

---

[4]For more information on the imaging system and its applications, see C. Kurz, "Tomography of Light Emission from the Plasma Edge of Alcator C-Mod", Doctoral Thesis, MIT Department of Nuclear Engineering, PFC/RR-95-5, May 1995.

Figure 2.5: Schematic of Plume Imaging System

Alcator C-Mod Machine Cell

C-Mod Vessel

Filter Wheel

CCD

Imaging Fiber

Video BNC

Control Cable

MACECAD
RECEIVER

Video Fiber

Control Fiber

Alcator C-Mod Control Room

Video Monitor

PC Image Archiving

MACECAD
TRANSMITTER

Video BNC

Video Output BNC

MACECAD
CONTROL
UNIT
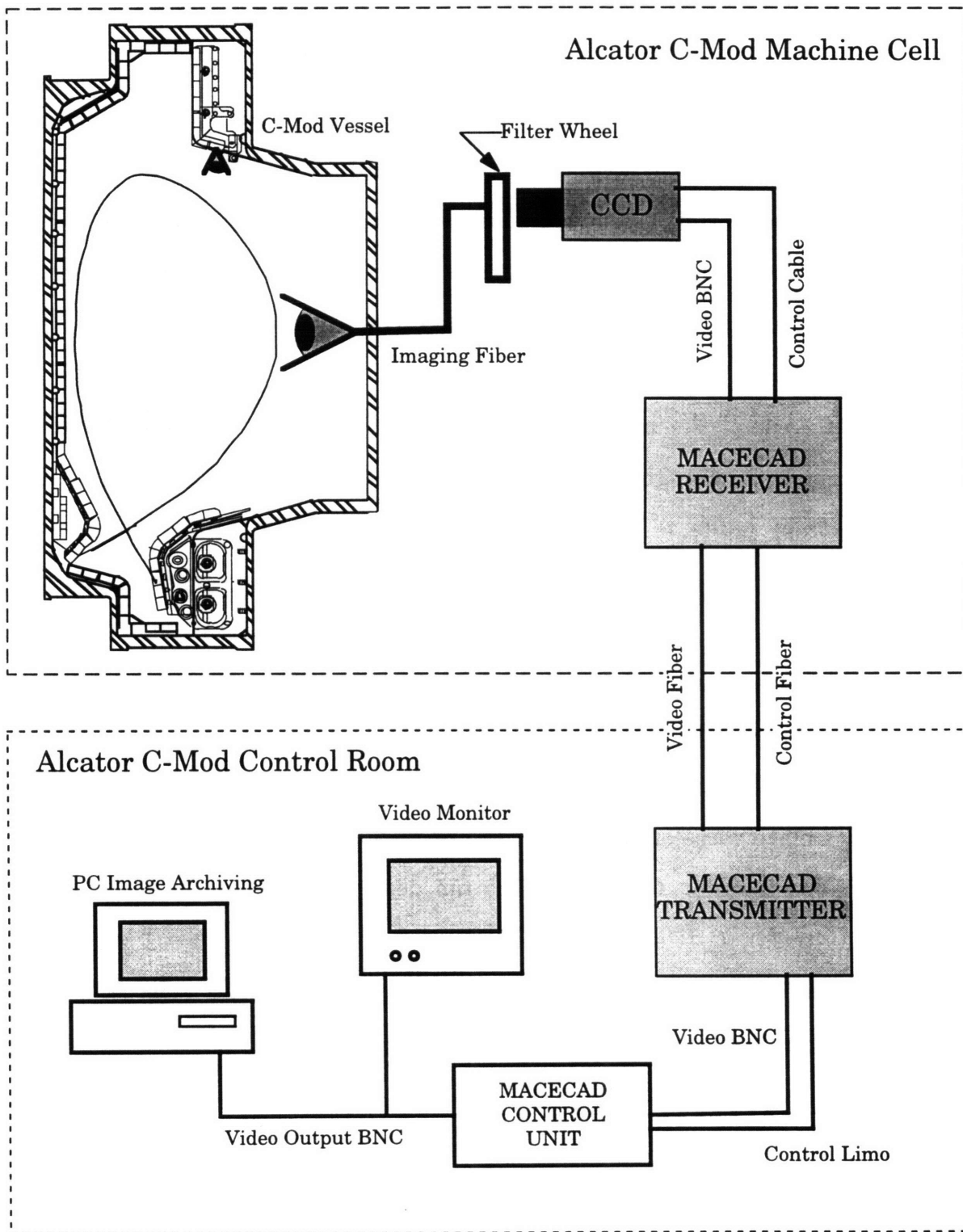
Control Limo

The bundles lead to modified CCD cameras (Hitachi KP-M1's) which convert the images to black-and-white digital video signals.[5] The cameras take 60 frames per second at 480x640 resolution and are controlled by Multiple Automatic Camera Exposure Control and Display (MACECAD) units developed and produced at Culham Laboratories in England (hence 'Culham cameras'). MACECAD sets the exposure time on the camera, using the brightest point inside a user defined rectangle in the image as its guide. When the brightness of the point exceeds or falls below user set limits, the exposure time is either doubled or halved on the next frame, as appropriate (from a minimum of .13 up to 16.6 msec). The exposure time of a given frame is overlaid on the image itself, giving automatic recording of the setting with the recording of the image. The system has a variable gain, allows for manual control of the shutter speed, and has a number of other features which make it attractive for the uses of this experimental program.[6] The MACECAD unit, located outside of the Alcator cell, uses fiber optic cables to exchange video and control signals with the CCD unit, located near the C-Mod vessel at the end of the imaging bundle.

The video images output by the CCD/MACECAD are displayed and recorded. Much of the plume imaging data has been recorded on videotape, an approach which is simple and relatively low cost, but which makes it necessary to redigitize the images through PC video cards for data analysis, a painful process which inevitably leads to loss of image quality. A system which can record the digital images directly has now been installed.

---

[5]"Operation Manual: KP-M1 Black and White CCD Camera", Hitachi Denshi, Ltd.
[6]See D.H.J. Goodall and M.E. Price, "Plasma Boundary Observations using an Asynchronous CCD Camera with Automatic Exposure Control", Journal of Nuclear Materials, 196-198(1992), pp. 1047-52; and D.H.J. Goodall, "Instructions for Operating MACECAD (Multiple Automatic Camera Exposure Control and Display)", UKAEA, Jun 1994.

Though allowing for the recording of only 30 frames per second, this system provides superior image quality and allows more direct and much easier manipulation of the images. The images are taken real-time by a PC video card frame grabber and stored on the PC hard drive. They are archived on optical disks which allow for easy transfer to the C-Mod workstations for viewing and analysis.[7]

2.2 Langmuir Probes

The primary Langmuir probe systems for Alcator C-Mod are shown in figure 2.6. There are two: divertor flush-mount probes and a fast-scanning probe. Because the Alcator edge region is relatively cool, the Langmuir probes, owing to their simplicity, give reliable and comparatively low cost measurements of electron density and temperature, plasma potential, and a decent gauge on the plasma flow velocity.[8] The measurements of these probes provide the backbone of edge diagnosis in C-Mod.

The flush probe array, a descendent of the DENSEPACK array on Alcator C,[9] consists of 10 triplets of probes on the outer divertor plate and 6 on the inner. A diagram of these triplets is given in figure 2.7. The probes are placed in groups of three, positioned to be on the same flux surface, to give the probes maximum flexibility in implementation. In theory, the probes could be used for fluctuation measurements or in double or triple-probe modes. Fluctuation measurements have yet to be attempted, and the

---

[7]A. Allen, et al, "The High Resolution Video Capture System on the Alcator C-Mod Tokamak", Rev Sci Instrum, to be published.

[8]For a concise description of Langmuir probe theory see I.H. Hutchinson, Principles of Plasma Diagnostics, Chapter 3, New York: Cambridge University Press, 1987.

[9]B. LaBombard and B. Lipschultz, "DENSEPACK: An Array of Langmuir Probes in the Limiter Shadow Plasma of the Alcator C Tokamak Fusion Experiment", Rev Sci Instrum, 57(1986), pp. 2415-24.

Figure 2.6: Alcator C-Mod Langmuir Probes

Fast-Scanning Probe

Inner Probe Array

Outer Probe Array

S.S. Support Plate   **Molybdenum Tile**

Key

Holes for Tile
Fastener

Tile
Fastener

diameter 3 mm

Belleville
Washers

6.6 mm
Toroidal Spacing

Molybdenum Probe
flush to surface
or with a "domed"
projection of 0.5 mm

Probe "Triplet":
- two flush probes
- one domed probe

Flame-Sprayed
Ceramic-Coating

Triaxial
Cable

<u>Side Cross-Section of
Probe/Plug/Tile Assembly</u>

<u>Plasma-Facing View of
a Probe Triplet in Tile</u>

Figure 2.7: Flush-Mount Probe Triplet Assembly

use of multiple probe methods have proved impossible because of cross-talk between adjacent probes (an interesting phenomenon in itself which has yet to be adequately investigated or explained). Two of the probes in each triplet are kept flush with the surface, the third is installed to protrude slightly. The protrusion is meant to overcome the effects of the very shallow grazing angle (on the order of 10 degrees) of the magnetic field on the divertor plate. In figure 2.7, this protruding probe is shown to be domed (with an approximately .5 mm projection). In late 1995, these domed probes were replaced with flat probes angled at about 10 degrees. Also in late 1995, the originally molybdenum probe wires, as shown in the figure, were replaced with tungsten. The normal mode of operation for each triplet is to sweep the protruding probe through its I-V characteristic (once every 10 msec) while the probes flush with the surface are kept in ion saturation or allowed to float electrically.[10]

The fast-scanning probe is a Langmuir system designed to measure parameter profiles across flux surfaces right up to, and on occasion inside, the LCFS. A low mass pneumatic piston with a stiff return spring is employed to drive the probe in and out of the plasma. From its rest position beneath the divertor tiles, the probe has an excursion time of about 100 msec, with a turnaround time from the point of maximum insertion on the order of milliseconds. When fired, the probe moves about 5", while the carriage on which the probe resides can move about 6", giving flexibility in the placement of the probe and the setting of its point of maximum insertion into the scrape-off layer. Figure 2.8 shows a diagram of the probe head. It is pyramidally shaped to reduce incident heat flux while positioning the

---

[10]For a more complete though less current description of the flush-mount probes see B. LaBombard, et al, "First Results from the Divertor Probe Array in Alcator C-Mod", Bulletin of the APS, 38(1993), Nov, 3S6.

Four 1.5 mm dia. tungsten wires, cut to match pyramidal surface

North

East

West

South

B-Field

15.875mm

View Along Axis of Pyramid

Side View of Pyramidal Probe Head

Axis of Pyramid

22 degree vertex angle
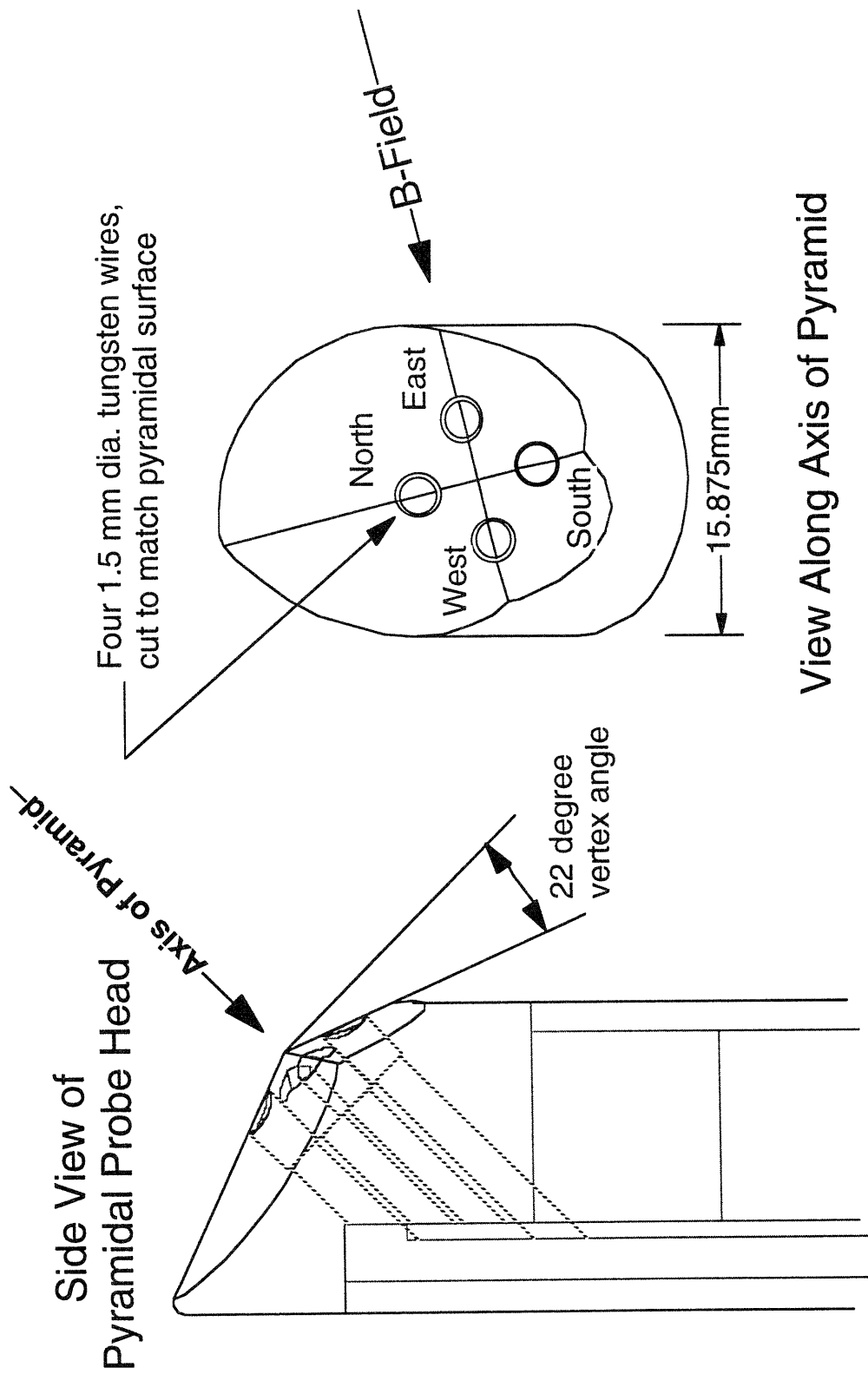
Figure 2.8: Fast-Scanning Probe Head Geometry

probe tips appropriately. Four Langmuir probes reside in the four vertices of the pyramid. They are placed to lie on the same flux surface, with one probe facing completely upstream along the field, one facing completely downstream, and the other two with their surface areas split between the two. The wires are filed to be flush with the surface of the probe head. Though originally made of molybdenum, the probe wires were replaced with tungsten in mid-1995. The head is designed to withstand a heat flux of 50 kW/cm^2. While the probe can in theory be used in double- or triple-probe mode, such operation has been found ineffective, and the probes are generally swept individually (a complete I-V characteristic every .3 msec), allowed to float, or kept in ion saturation. The implementation of the scanning probe as a Mach probe has met with moderate success. While the velocities are not regularly calculated because of the uncertainty in which flow model to use (more on this in chapter 6), using the ratio of the upstream and downstream ion currents gives a relative gauge of the flow, and well identifies the flow direction (these measurement are important for comparison with the NINJA/Culham diagnostic observations). Scrape-off widths of millimeters are typically measured with the scanning probe, with widths as high as 2-3 cm occasionally reached in high density shots.[11]

Using the above two diagnostics in tandem (flush-mounts and scanning probe) has given some of the most interesting measurements made on C-Mod. An illustrative example was given in figure 1.10. The combination yields parameter measurements at different locations on the same flux surface. Such measurements are relatively rare on tokamaks.

---

[11]For more complete though less current description of the fast scanning probe see:

D. Jablonski, et al, "First Results from the Alcator C-Mod Reciprocating Probe System", Bulletin of the APS, 38(1993), Nov, 3S7.

J. Weaver, "The Development of a Reciprocating Langmuir Probe System for Alcator C-Mod", Bachelor's Thesis, MIT Department of Physics, May 1992.

The definitive characterization of plasma detachment, and other phenomena on C-Mod, by the density and temperature profiles along the field lines in the SOL is interesting and unique. For recording edge measurements, and to a lesser extent, core parameters, an edge database has been created. On each shot, time slice(s) are chosen for which the Langmuir probe and various other diagnostic measurements are extracted from the general C-Mod data-tree (which resides in a CD-ROM jukebox), and put into a well structured, easily manipulated format (stored on hard disk, which allows for much fast access time). The construction of this time slice database has proved invaluable for the analysis and characterization of the edge.[12]

2.3 Other Diagnostics

Alcator C-Mod has a large array of diagnostics, the measurements of nearly all of which this thesis relies upon to some extent. Below is given an abbreviated account of a few of them:

An extensive array of electrical loops for measuring magnetic field, magnetic flux, and plasma current are installed on C-Mod. These diagnostics are critical for diagnosing and controlling the plasma.[13] Reconstruction of the magnetic flux surfaces with these measurements is done using the EFIT code,[14] providing a generally reliable diagnosis of the magnetic geometry.

The primary device for diagnosing the density profiles of the central plasma is a custom built two-color interferometer system (TCI). Ten CO_2

---

[12]B. LaBombard, private communication, Feb 1996.
[13]R.S. Granetz, et al, "Magnetic Diagnostics in Alcator C-Mod", Rev Sci Instrum, 61(1990), pp. 2967-9.
[14]L.L. Lao, et al, "Reconstruction of Current Profile Parameters and Plasma Shapes in Tokamaks", Nuclear Fusion, 25(1985), pp. 1611-22.

and four HeNe channels are used, with a spatial view of the plasma (from a major radius of 62 to 78 cm) shown in figure 2.9. The measurements are employed for both reconstruction of the plasma density profile and as the signal for feedback control on the plasma density.[15]

A high resolution, time-resolving, absolutely calibrated, grazing incidence spectrometer for monitoring impurity radiation in the central plasma (and hence impurity levels) in the 5-110 nm range is installed. The system is referred to as either the VUV or McPherson (after its main component supplier) spectrometer. Its viewing range across the central plasma is shown in figure 2.9. It has spatial resolutions of approximately 1 cm poloidally and 15 cm toroidally.[16]

A five-chord high-resolution x-ray spectrometer has been designed and built for monitoring emission between .28 and .40 nm, covering the entire range of helium- and hydrogen- like Argon. The viewing range of the spectrometer chords is shown in figure 2.9. The system has a spatial resolution of 3 cm, and each chord can monitor a 12 pm wavelength range at a time. The system is used for monitoring Argon levels in the core plasma, and deducing ion temperatures from measurements of the Doppler broadening of the resonance lines.[17]

Edge neutral pressure measurements are made with six separate gauges, their poloidal positions shown in figure 2.10. Pressure in the lower divertor is measured with a pair of fast linear gauges custom built for use in the high magnetic field at their in-situ location. The measurements of

[15]T.C. Luke, "Measurement of Particle Transport Coefficients on Alcator C-Mod", Doctoral Thesis, MIT Department of Physics, PFC/RR-94-12, Oct 1994.
[16]M.A. Graf, "Impurity Injection Experiments on the Alcator C-Mod Tokamak", Doctoral Thesis, MIT Nuclear Engineering Department, PFC/RR-95-6, Jun 1995.
[17]J.E. Rice and E.S. Marmar, "Five-chord High-Resolution X-ray Spectrometer for Alcator C-Mod", Rev Sci Instrum, 61(1990), pp. 2753-5.

TCI Interferometer

VUV Spectrometer

X-Ray Spectrometer
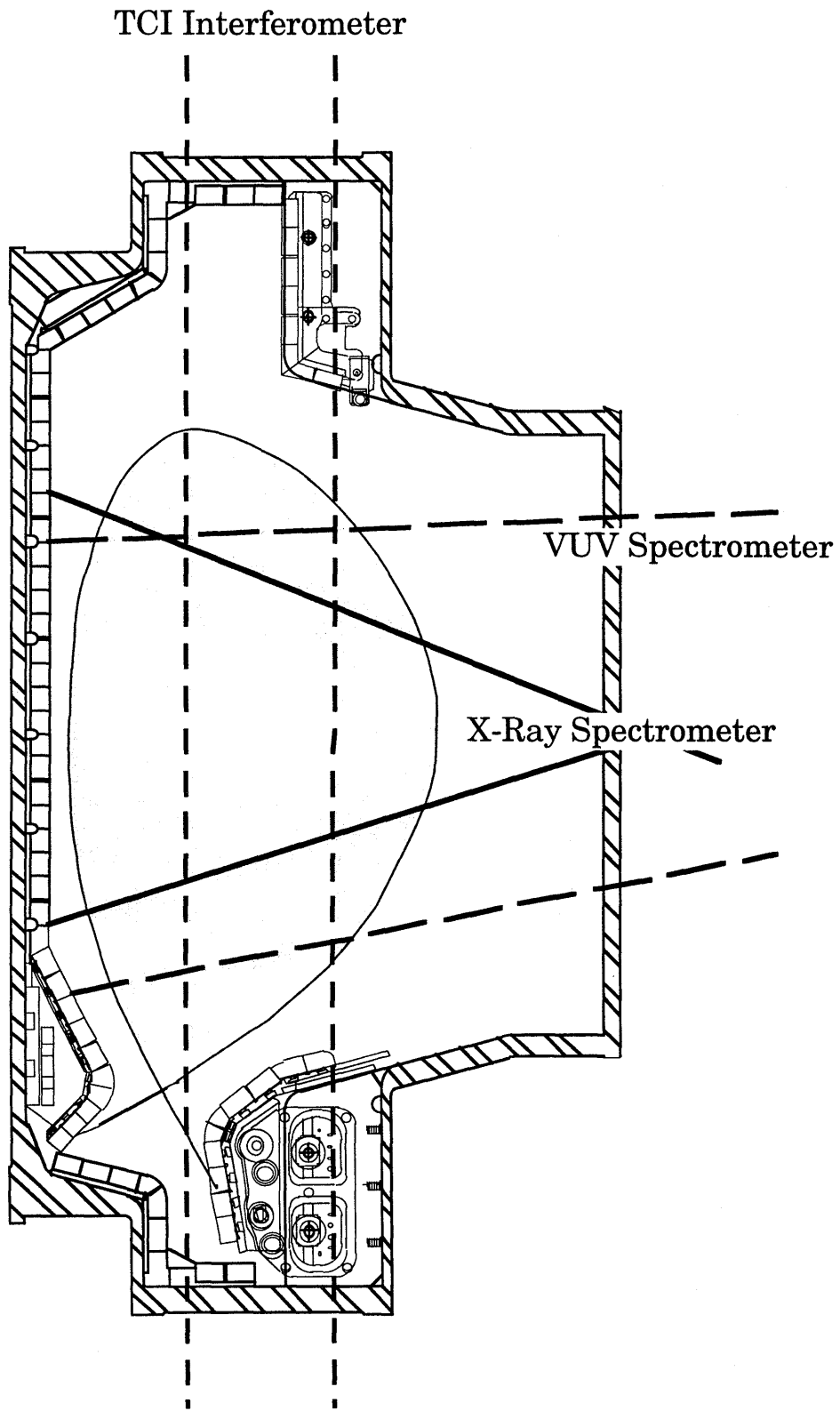
Figure 2.9: Extent of Chords of three C-Mod Core Diagnostics
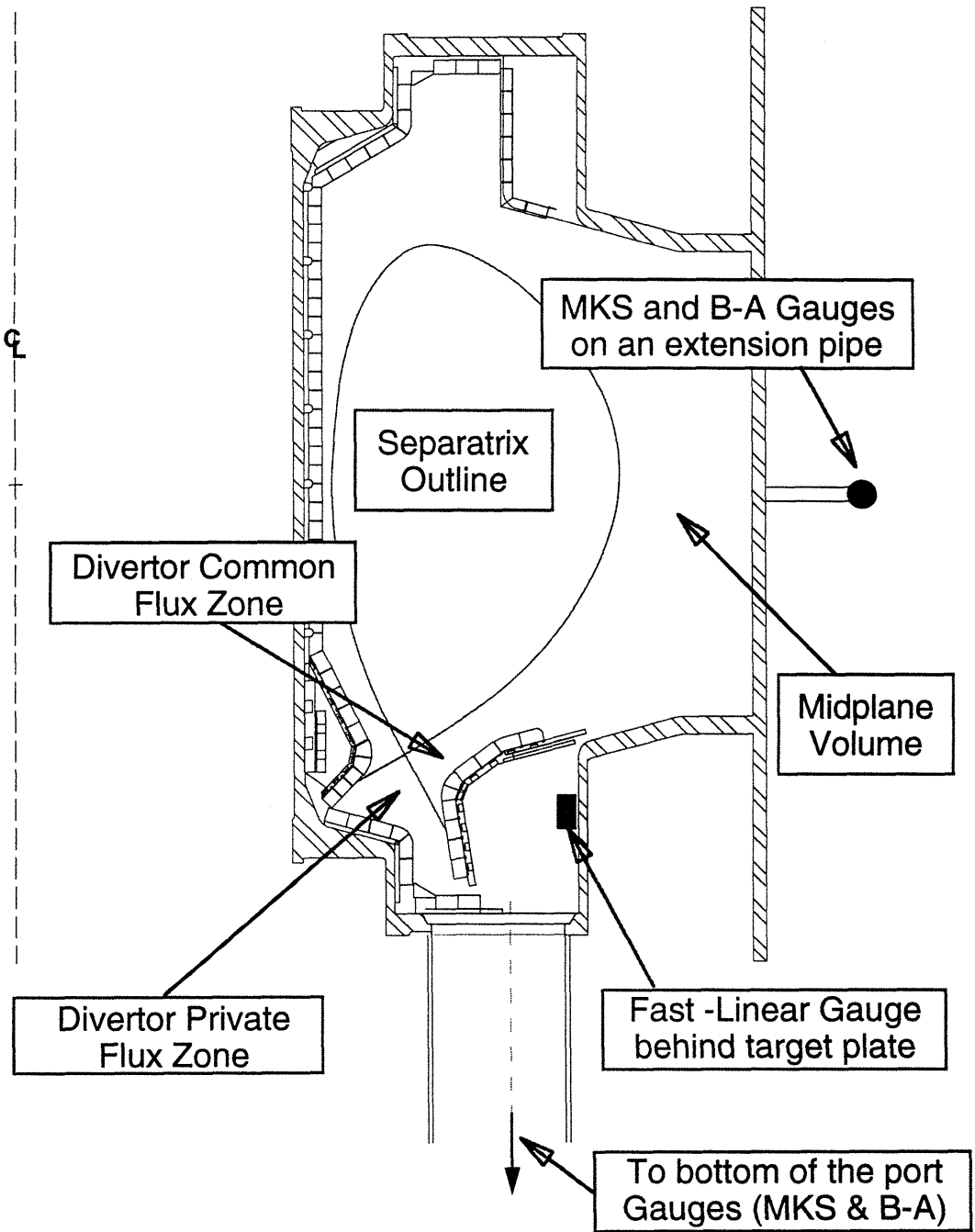
Figure 2.10: Neutral Gauge Locations

CL

MKS and B-A Gauges
on an extension pipe

Separatrix
Outline

Divertor Common
Flux Zone

Midplane
Volume

Divertor Private
Flux Zone

Fast -Linear Gauge
behind target plate

To bottom of the port
Gauges (MKS & B-A)

these are complemented by more accurate but slower time response Bayard-Alpert (B-A) ionization and MKS-626 capacitance manometer gauges, located at the bottom of a diagnostic port of the machine. There are also B-A and MKS gauges located on the outboard midplane on an extension pipe for measuring pressure in the main plasma chamber (as opposed to the divertor region).[18]

[18]A. Niemczewski, "Neutral Particle Dynamics in the Alcator C-Mod Tokamak", Doctoral Thesis, MIT Nuclear Engineering Department, PFC/RR-95-8, Aug 1995.

Chapter 3
Screening

This chapter provides an overview of two groups of experiments performed on C-Mod utilizing the NINJA system. The first involves comparing the effect of fueling the plasma through different capillaries, the second investigates the screening properties of recycling and non-recycling impurities puffed into the chamber. Figure 3.1 shows the capillaries utilized (the NINJA capillaries on the top of the machine have not been used) in C-Mod experiments thus far. They are labeled A through L for easy reference. The standard Alcator divertor configuration ('vertical target') shown in the figure is that used in the experiments unless otherwise noted. In addition to the NINJA capillaries, a piezo valve on the primary C-Mod gas system is employed in experiments described in the second section. It is located at the outboard midplane at the same toroidal location as the capillaries.

3.1 Deuterium Fueling

The C-Mod run on 5 March 1995 was devoted to a simple set of experiments which, while not in keeping with the impurity puffing focus of this thesis, are mentioned because of the important aspect of edge transport

Figure 3.1: Utilized NINJA Puffing Locations

Magnetic Separatrix

A
B
C
D
E
F
G
H
I
J
K
L
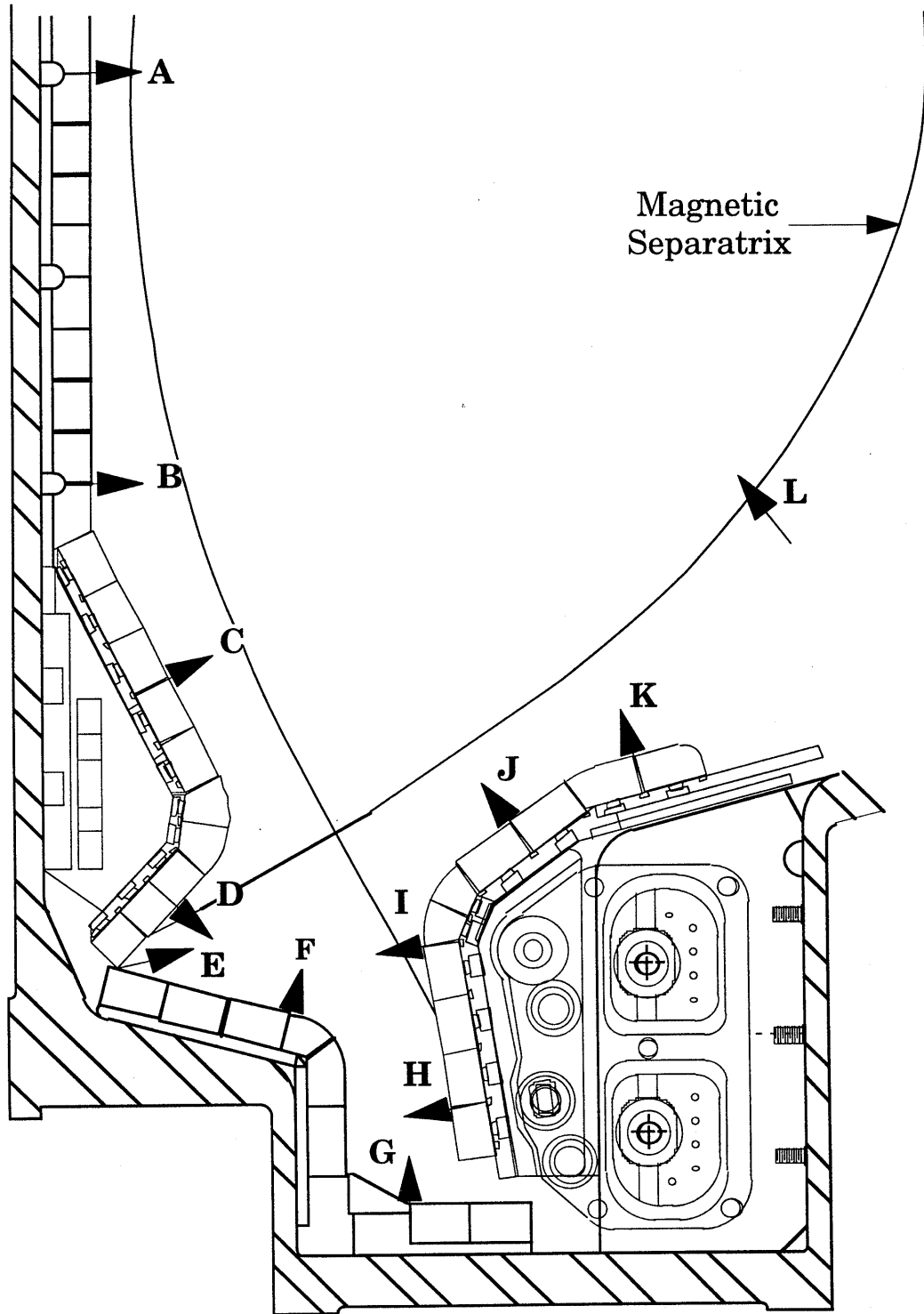
they uncovered. The run involved repeating a 'basis' shot throughout the day, varying only the size and location of a deuterium puff introduced through NINJA. The basic finding was that there was no discernible difference on confined plasma or edge conditions between similarly sized puffs through different capillaries. This implies that fueling properties are entirely a function of puffing quantity. This result is important because of the desire one might have for the opposite to be the case. It would be convenient to control the neutral pressure in the divertor somewhat independent of the central plasma density, or, more specifically, to control the plasma conditions at the divertor plate independent of conditions in the central plasma, and vice-versa. This set of experiments showed that such a goal cannot be attained through selective edge fueling, at least not in Alcator C-Mod. For otherwise similar discharges, the edge parameters were seen to be strictly related to central parameters independent of where the plasma was fueled from.

Figure 3.2 provides a summary of three representative discharges of the run with time histories of selected parameters. The first column gives the basis shot, performed throughout the day, without NINJA puffing. The shots were standard 800 kAmp, 5.3 Tesla on axis, single null diverted Deuterium discharges. The second row gives the total number of electrons in the central plasma, as measured with the TCI, the third row the neutral pressure at the outer midplane, as measured with the ionization gauge, the bottom row the divertor pressure as measured with the bottom MKS gauge. The horizontal axis is time in seconds. The second and third column show the time history of these parameters for injections of two different quantities through a capillary on the inner divertor (location C on figure 3.1). The integrated time history of the injection is given in the first row. For both of
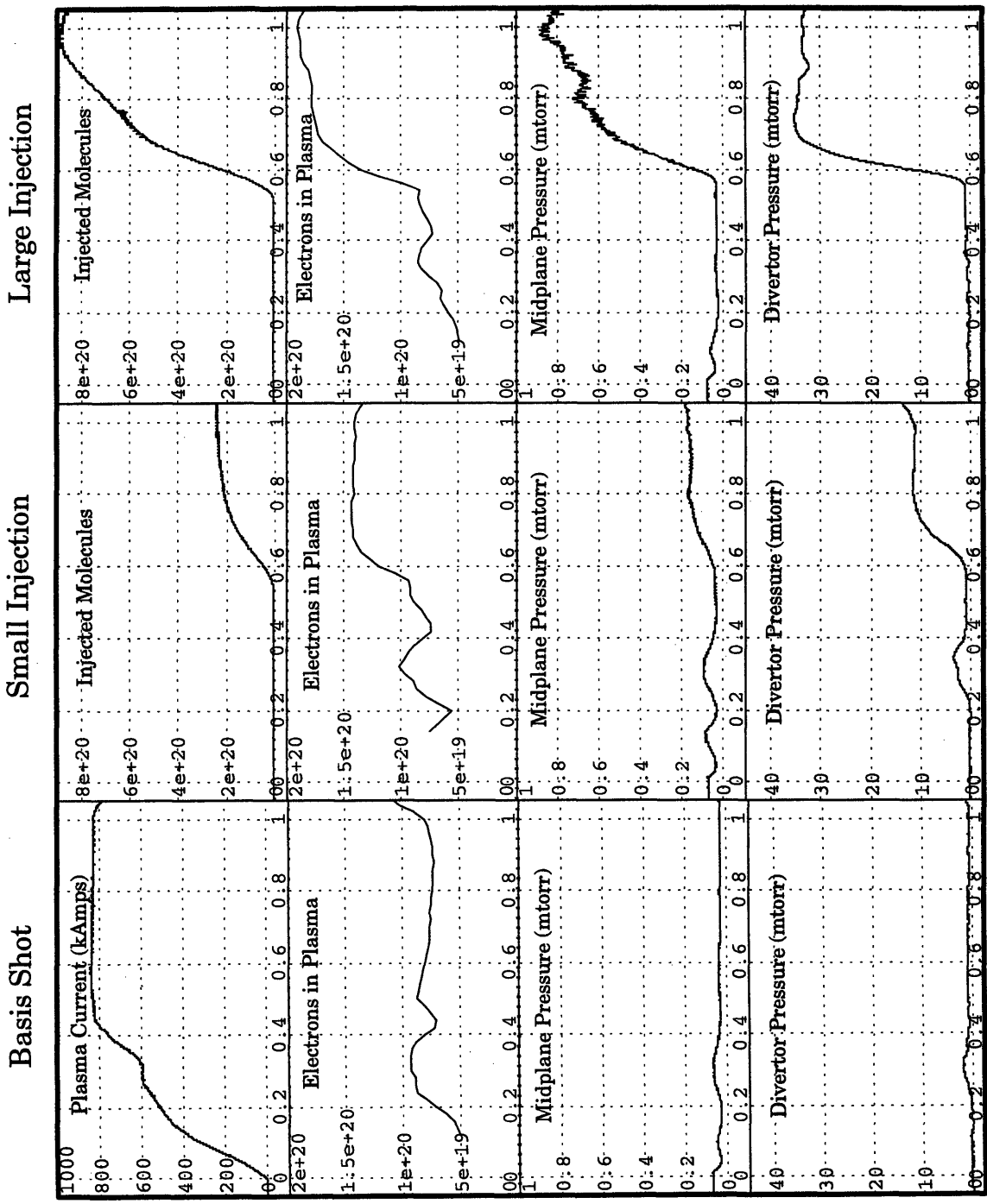
Figure 3.2: Example Shots from NINJA Fueling Run

these shots, the NINJA injection is a large fueling source for the plasma, and raises the edge neutral pressures substantially. While the basis shot has the edge plasma in the sheath limited regime, the puffing in the 'Small Injection' case takes the edge plasma into high-recycling, and the 'Large Injection' causes the divertor to detach (for discussion of these regimes, see section 1.3.1).

Shots with similar puffing quantities were run with four other capillaries as well, giving a basis for comparison between the locations. The time history of the injection (shown in the first row of figure 3.2) for the different locations can be assumed equal for the sake of this comparison (small differences do exist because of different capillary lengths from the plenum). Figure 3.3 compares two of these locations, in the private flux zone (F) and at the inner-wall midplane (A). The top plot is of confined electrons in the central plasma, the bottom of the compression ratio (defined as the ratio between the bottom MKS and side ratiomatic gauges). Little difference is apparent between the shots. At least for these two parameters, and this puffing rate, fueling at the midplane and in the private flux zone looks identical (this goes for other central and edge parameters as well). In lieu of making similar plots for the other shots, table 3.1 summarizes their results. The numbers given for confined electrons and compression ratio are the average of these values between .85 and .95 seconds. The pattern of little difference between puff locations extends to all capillaries at both small (taking the edge into high recycling) and large (inducing a detached divertor) injection rates. For the small injections, the number of confined electrons varies between 1.34 and 1.41×10^{20} and the compression ratio from 60.8 to 73.4. For the large injections, confined electrons varies between 1.72 and 1.85×10^{20} and the

Figure 3.3: Time Histories for Small Injection Case
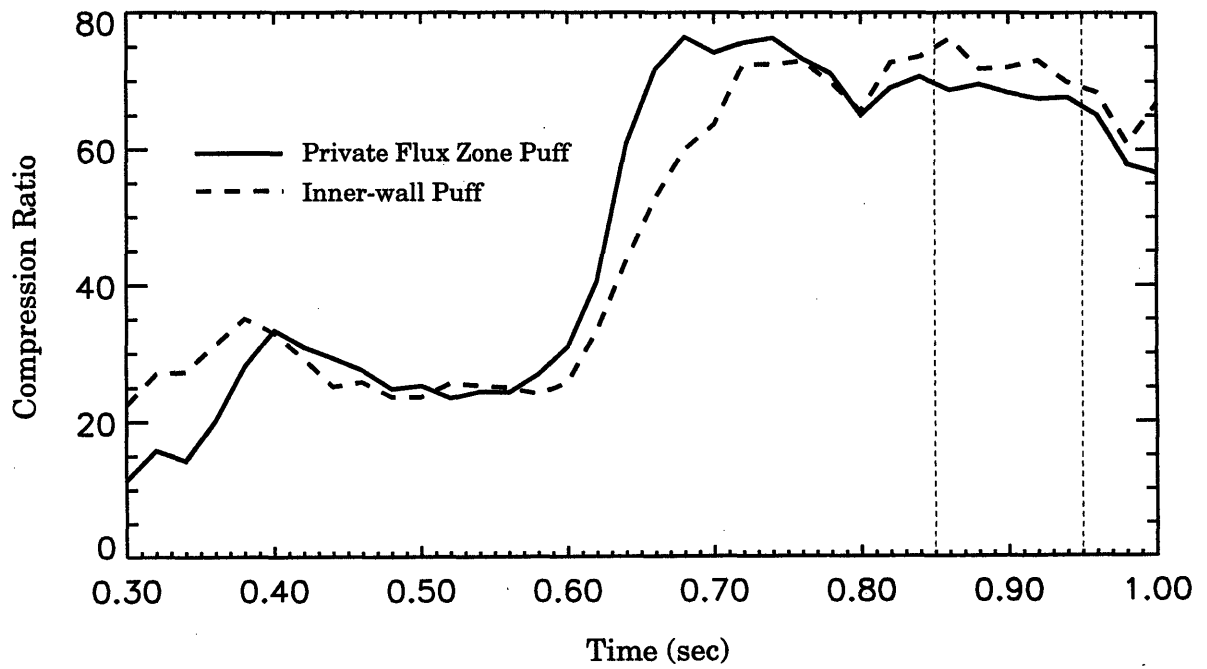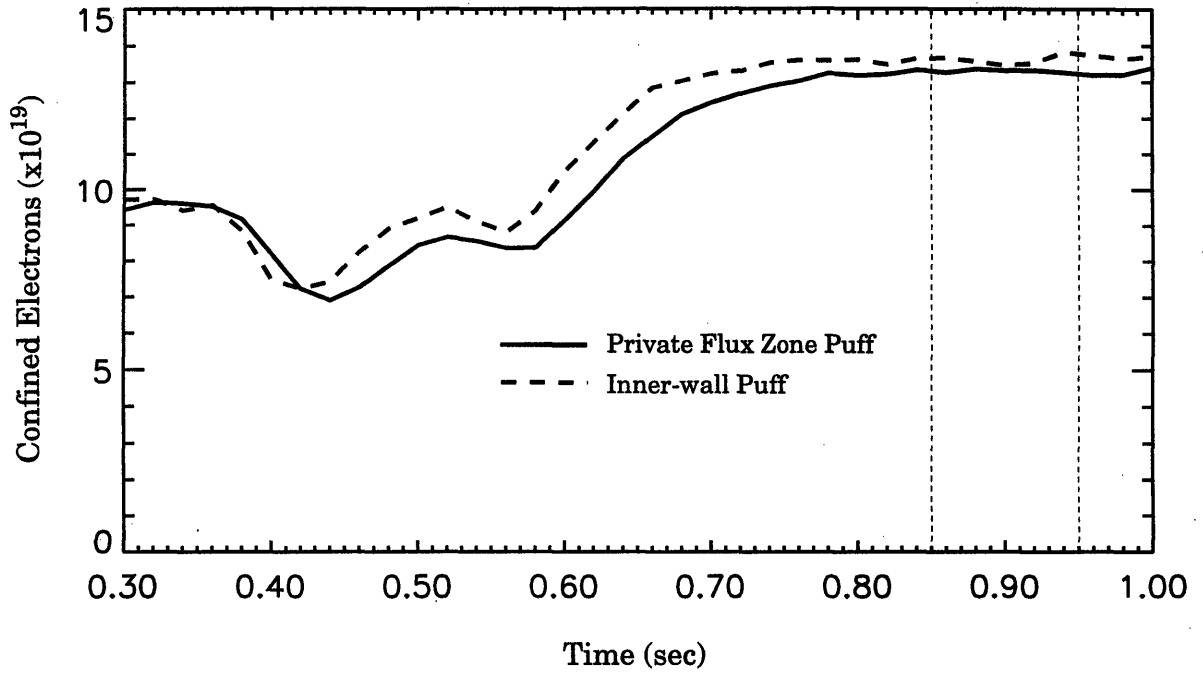
Table 3.1: Comparison of Puff Locations

Location	Small Injection		Large Injection	
	Confined e's	Comp Ratio	Confined e's	Comp Ratio
Priv Flux (F)	1.40×10^{20}	68.4	1.85×10^{20}	51.9
Out Div (I)	1.38×10^{20}	70.5	1.72×10^{20}	51.3
Out Div (K)	1.34×10^{20}	60.8	1.74×10^{20}	49.2
Inr Wall (A)	1.36×10^{20}	69.7	1.76×10^{20}	49.8
Inr Div (C)	1.41×10^{20}	73.4	1.85×10^{20}	45.4

compression ratio from 45.4 to 51.9. These variations are within measurement uncertainties, indicating that the shots were, for all intents and purposes, identical.

To explain why this is so, one can do a simple calculation of the flux of deuterium ions striking the divertor plates (integrating the particle flux as measured by the flush-mount probes over the plate surfaces). This flux is typically on the order of 10^{23} ions/sec.[1] Even for the large injection case, the atoms injected per second was on the order of 10^{21}. Consequently, one would expect recycling to dominate the fuel source, as is observed in these experiments. Put another way, the plasma throws around neutrals and ions far too quickly for the fueling location to make a difference. (Unless one introduces a very large quantity of fuel in the core plasma in a very short period, as one can do with Deuterium pellet injection on C-Mod.)

3.2 Impurity Screening

The screening properties of the edge have been investigated with two recycling (Argon and Neon) and two non-recycling (Carbon and Nitrogen) impurities. The impurities were injected at various locations (Carbon was introduced with methane puffing), and the quantity of that impurity residing in the central plasma monitored. The first section below provides an overview of the results of these screening experiments. The second section discusses a simple fluid model constructed to clarify some of the physics basis behind non-recycling impurity screening behaviour.

---

[1]For a discussion of this, as well as a much more complete treatment of the relations of fueling, neutral transport, and edge and confined plasma properties, see: A. Niemczewski, "Neutral Particle Dynamics in the Alcator C-Mod Tokamak", Doctoral Thesis, MIT Nuclear Engineering Department, PFC/RR-95-8, Aug 1995; and A. Niemczewski, et al, "Neutral Particle Dynamics in the Alcator C-Mod Tokamak", submitted to Nuclear Fusion.

3.2.1 Results of Experiments[2]

For these experiments, C-Mod was run in Deuterium with a plasma current of 800 kAmps and a magnetic field of 5.3 Tesla on axis in the single-null diverted vertical plate configuration. The impurity radiation in the core was monitored with the VUV spectrometer, and the Argon XVII emission line was observed with the x-ray spectrometer. With the measurements of these two diagnostics, the charge state distribution of the impurity ions, and hence the impurity content of the confined plasma, was calculated with MIST, a one-dimensional core impurity transport code.[3]

During Argon and Neon injections, typically 1-3% of the injected atoms were seen to get into the central plasma. After the injection, the plasma content of the impurity stayed approximately constant for the duration of the shot. A representative Argon puff is shown in figure 3.4, which plots both the number of Argon atoms in the core, and the integrated number of atoms injected as a function of time. The gas was puffed through the midplane piezo valve. The number of confined Argon atoms is shown to be proportional to the integral of the quantity injected, yielding a fueling efficiency (ratio of confined atoms to atoms injected) of about 2.3% (as can be seen in the plot, the error bar on this number is on the order of .5%). Figure 3.5 shows the roughly linear dependence this fueling

[2]For more on these and related impurity screening experiments on C-Mod, see:
   R.S. Granetz, et al, "A Comparison of Impurity Screening between Limited and Diverted Plasmas in the Alcator C-Mod Tokamak", Journal of Nuclear Materials, to be published.
   G.M. McCracken, et al, "Impurity Screening in Alcator C-Mod", Proceedings of the 22nd European Conference on Controlled Fusion and Plasma Physics, Volume II, 1995, pp. 313-6.
   G.M. McCracken, et al, "Screening of Recycling and Non-Recycling Impurities in the Alcator C-Mod Tokamak", Journal of Nuclear Materials, to be published.
[3]R.A. Hulse, "Numerical Studies of Impurities in Fusion Plasmas", Nuclear Technology/Fusion, 3(1983), pp. 259-72.

Figure 3.4: Time Dependence of Confined Argon
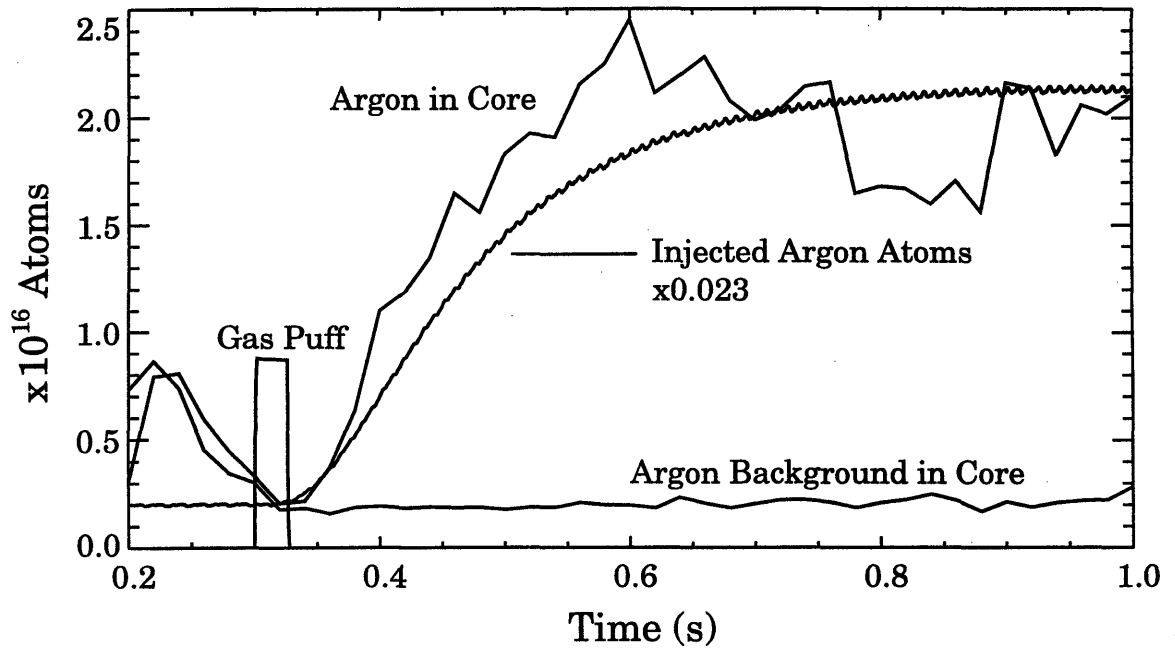

Argon in Core

Injected Argon Atoms
x0.023

Gas Puff

Argon Background in Core

x10^{16} Atoms

Time (s)

Figure 3.5: Argon Fueling Efficiency

% of Injected Atoms Inside the Separatrix

Core Electron Density (x10^{19} per m^3)
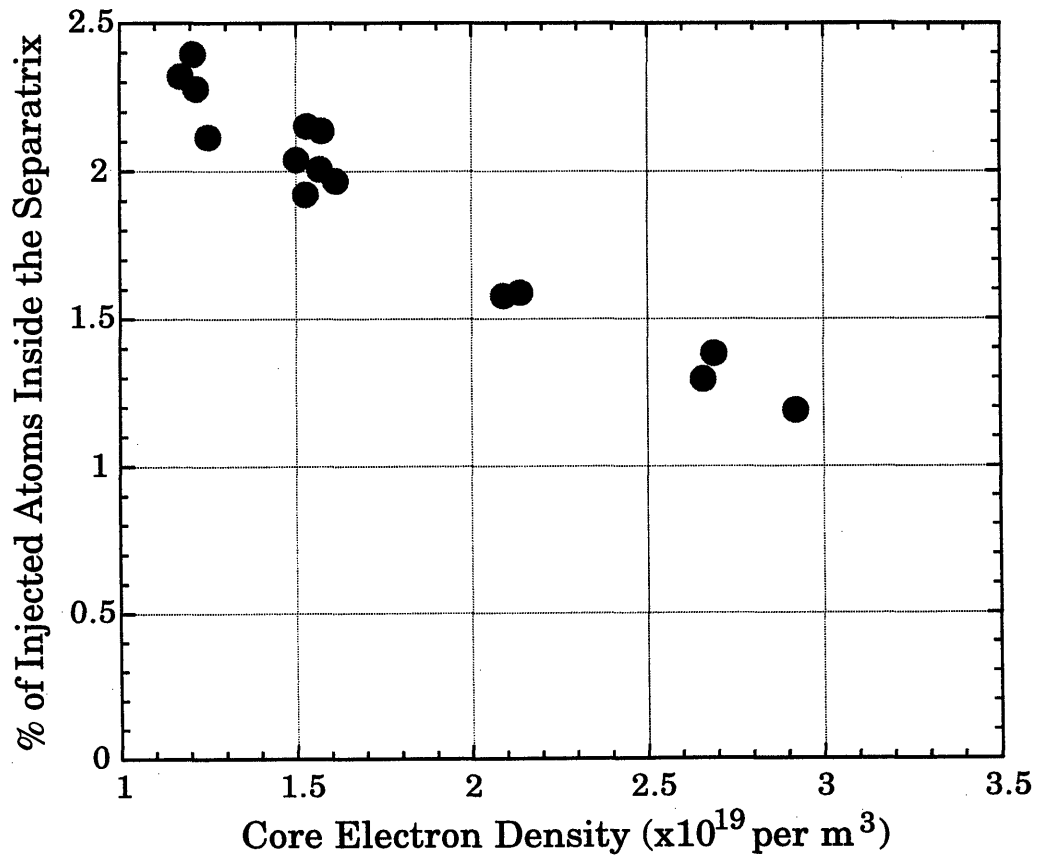
efficiency of Argon is observed to have with the central plasma density, much better screening being seen at higher densities (for these shots, going from about 2.5% at $1 \times 10^{19}/m^3$ to about 1% at a central density of $3 \times 10^{19}/m^3$). The points plotted are for the shots of a particular run (941220), showing a remarkably consistent behaviour. Across run days, while the same general trend is observed, there is much greater scatter in the fueling efficiency data, indicating that it is sensitive to not only the particular plasma conditions of the shot, but also to wall conditioning. Similar dependence was seen in Neon experiments. As was the case for the Deuterium experiments described in the last section, little difference was observed to exist for fueling efficiency between puffing locations.

One could characterize the recycling impurities (as well as Deuterium) as exhibiting 'steady-state' behaviour. When they are introduced, they remain as ions and gases in the plasma chamber, with the properties of the plasma itself determining where and how they reside. The time history, method, and location of introduction have little effect on such parameters as fueling efficiency. The results of the Nitrogen and methane injections provide a stark contrast. Since these impurities are largely non-recycling (meaning a significant fraction of the ions striking a solid surface are not re-emitted), one expects a different behaviour, a behaviour one might characterize as 'transient'. Since the solid surfaces of the chamber effectively act as a pump on these impurities, their time history and method and location of introduction have a significant impact.

Figure 3.6 shows a typical Nitrogen injection through the midplane piezo valve. The Nitrogen content in the central plasma is plotted, as well as the rate of injection (the y-axis is used for both atoms and atoms/sec). It is seen that the Nitrogen content is not proportional to the total amount

Figure 3.6: Time Dependence of Confined Nitrogen
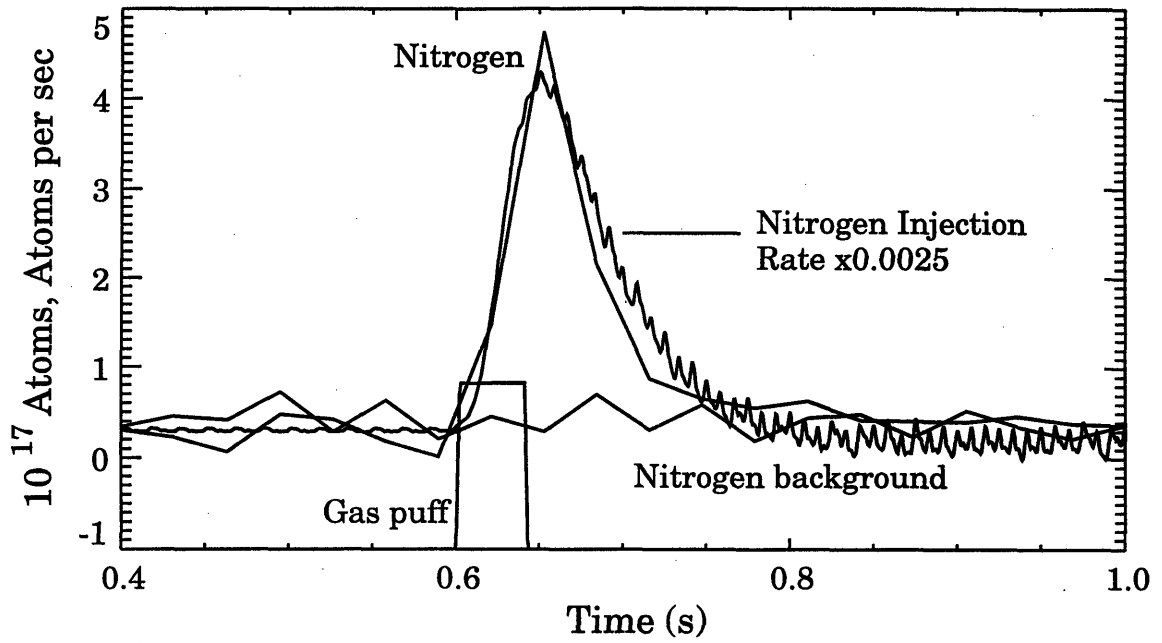
Figure 3.7: Nitrogen Screening in Diverted Discharges
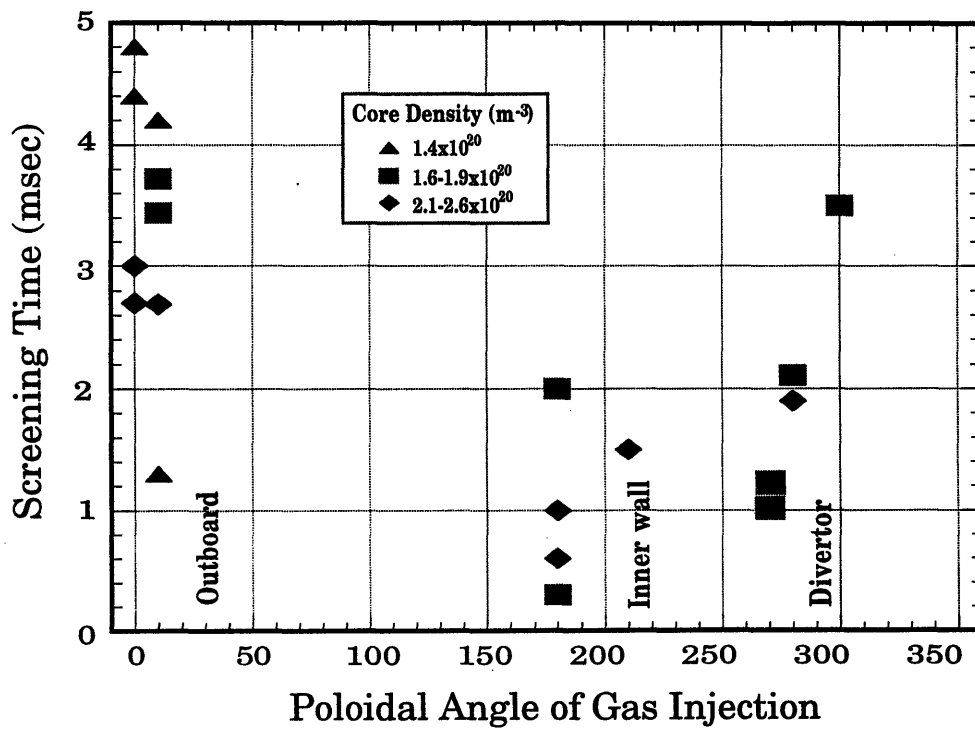
injected, but rather to the instantaneous rate of injection. Instead of the number of impurities reaching the central plasma being characterized by a non-dimensional fueling efficiency, it is instead characterized by a characteristic time (defined by the ratio of the confined plasma Nitrogen content to the injection rate), in this case about 2.5 msec. After the injection, the Nitrogen content decays quickly, with a time constant of about 30 msec, comparable to confinement times measured by laser ablation,[4] and putting an upper bound on the Nitrogen recycling coefficient of .3 (by comparison, that of Argon is essentially unity).

In figure 3.7, the screening time is plotted for an array of shots at varying plasma densities and Nitrogen injection locations. Because the ions make it into the central plasma in such small quantities, measurement of their core densities is difficult, hence the error bars on these values are large. The shots are a collection from experiments performed in 1995 and early 1996 (specifically runs 9505217, 951219, and 960202). Different symbols are used for three different core density ranges, with the screening time plotted as a function of the poloidal angle of the injection location. The outer wall grouping includes puffs from the side piezo and location K, the inner-wall grouping locations A and B, and the divertor grouping locations F, I, and J. While this plot shows quite a bit of scatter in the results, it is seen that the density dependence of the screening time is weak while the dependence with puffing location is rather strong. The screening of the Nitrogen is generally best for injections in the private flux zone, worst for injections in the outer SOL. Similar though less definitive results are observed for Carbon (Carbon tends to be better

---

[4]M.A. Graf, et al, "Spectroscopic Measurement of Impurity Transport Coefficients and Penetration Efficiencies in Alcator C-Mod Plasmas", Rev Sci Instrum, 66(1995), pp. 636-8.

screened than the Nitrogen, making core measurements of Carbon ion densities difficult due to the sparse amount that gets in).

3.2.2 NO-RISC Model

For modeling of injected recycling impurities, the situation is somewhat difficult. A refinement of the Engelhardt model,[5] or, to do it properly, a 3-D impurity transport code such as DIVIMP (see chapter 5) would have to be used. The relative simplicity of non-recycling impurity behaviour suggests the implementation of a fluid model to elucidate the screening observations. The simplicity comes from the fact that the ions which make their way to a solid surface can be considered lost (embedded in the wall, gone from the tokamak plasma). The NOn-Recycling Impurity SCreening (NO-RISC) model uses two one-dimensional continuity equations to relate the screening of impurity ions (essentially, what quantity of some amount injected enters the confined plasma) to the local edge plasma parameters.[6]

The density of the impurity ions is considered to be solely a function of minor radius, i.e. that the ions are transported along field lines quickly enough such that over the surface they inhabit, the density is uniform. This is shown in figure 3.8. On the flux surface, the ions are thought of as having an area in which they reside, extending along the field line to the divertor plate (a connection length L), with the poloidal width, λ, determined by the poloidal cross-field diffusion coefficient. Radially, the ions cannot be considered uniform, but will have their density profile determined by where the injected molecules ionize, the radial cross-field

---

[5]W. Engelhardt and W. Feneberg, "Influence of an Ergodic Magnetic Limiter on the Impurity Content in a Tokamak", Journal of Nuclear Materials, 76-77(1978), pp. 518-20.
[6]G.M. McCracken, private communications, Mar-Apr, 1996.

Figure 3.8: Geometry of NO-RISC Model

Divertor Plate

L

Region of Uniform Impurity Ion Density
(Density has only Radial Dependence)

λ

Puff

Along Magnetic Field Line (in direction of flow)

Across Field (Poloidal)
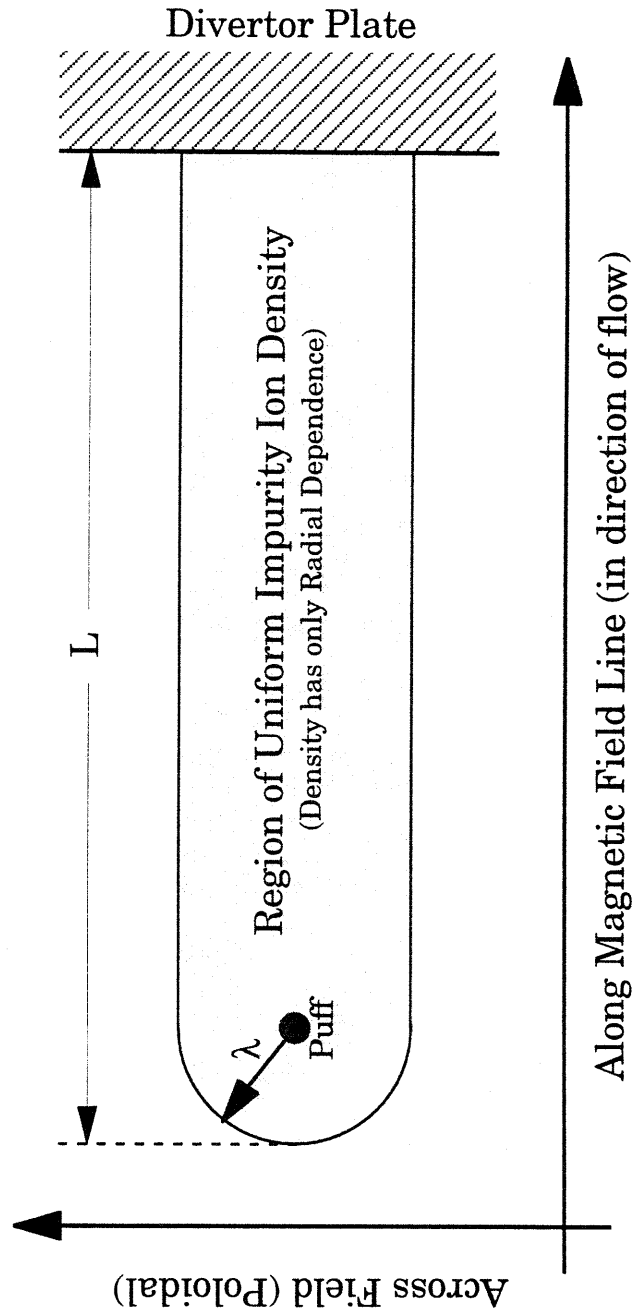
diffusion coefficient (considered anomalous), and the loss of impurity ions to the effective pumping action of the divertor plate.

For an injected impurity neutral species, the radial continuity equation is:

$$\frac{d}{dr}(n_n v_o) = -n_n n_e < \sigma v >_i \qquad (3.1)$$

where n_n and v_o are the impurity neutral density and velocity. The equation represents the attenuation of the molecular flux by ionization. Since the velocity of the neutrals can be taken as constant (no significant charge exchange or other ion-neutral interaction), this can be integrated to obtain the radial neutral density profile, and then multiplied with the rate coefficient to obtain the ionization rate as a function of radius:

$$S(r) = n_o n_e < \sigma v >_i \exp\left[-\frac{1}{v_o} \int_0^r n_e < \sigma v >_i dr \right] \qquad (3.2)$$

for which n_0 is the neutral density at the wall, and v can be taken as the room temperature thermal speed. The neutral density n_0 will be equal to the influx rate of atoms divided by the impurity velocity v_0 (keep in mind that since these are 1-D equations, all ion and atom densities are in units of m^{-1}). The ionization rate is labeled S because it is the source function for the impurity ions. Once the molecules are ionized, they are considered to be distributed evenly over the area shown in figure 3.8.

For the ions (grouped as a whole), the radial transport is taken as entirely diffusive (no pinch or drift velocities), and a loss term due to the ions being lost at the divertor plate is included. For the radial continuity equation, this gives:

$$-D\frac{d^2n}{dr^2} = -\frac{nv}{L} + S(r) \qquad (3.3)$$

where n is the density of impurity ions, v the velocity the ions acquire along the magnetic field, L the distance the ions need travel to reach the divertor

plates, D the anomalous radial diffusion coefficient, and S(r) the source term given by equation 3.2. The loss term in equation 3.3 is taken as the ion density divided by L/v, which is an approximation of the time the ions take to be transported to the divertor plate. For the first boundary condition, the ion density at the wall (r=0) is taken to be zero (n(0)=0). Since the wall is a strong sink, this assumption is reasonable. For the boundary at the LCFS (r=1, at the 'beginning' of the core plasma), the situation is a bit more complicated. When the ions enter the plasma, they are efficiently transported to fill the core to a more or less uniform density. They are transported out of the core fairly uniformly. Hence, for the non-recycling impurity puffing, the flux of the ions into the core can be thought of as local (localized to the area shown in figure 3.8), the flux out of the plasma as global, being uniform over the surface of the LCFS. For a steady state impurity content in the core, these fluxes are equal, hence, assuming the ion density at the LCFS is uniform around the torus, one has:

$$\frac{AD}{\lambda}n(1) = -aD\frac{dn}{dr}\bigg|_{r=1} \tag{3.4}$$

where A is the area of the core plasma, a the area of the impurity influx region, D the perpendicular diffusion coefficient for the impurity ions, and $\lambda \equiv (DL/v)^{1/2}$, the characteristic impurity decay length (same as the λ mentioned above since the diffusion coefficient is taken as the same in the poloidal and radial directions). Equation 3.4 provides the second boundary condition. The area of the plasma can be obtained from magnetic reconstruction results (generally about 7 m²). For the area of the impurity influx region, the estimate is made:

$$a = \lambda L \sqrt{\pi} \tag{3.5}$$

for which L is the distance along the field line from the puff location to the plate (generally about 10 m). This is the area of figure 3.8; the factor of

square root of π is used instead of the more obvious factor of 2 in order to correct for the fact that the density is not exactly poloidally uniform, but rather drops off approximately as a gaussian.

Solving 3.3 with the BC's, one arrives at the equation:

$$n(r) = \frac{\lambda}{2D}\left[e^{r/\lambda}(I_0 - I_1(r)) - e^{-r/\lambda}(I_0 + I_2(r))\right] \qquad (3.6)$$

for which the following are defined:

$$I_1(r) \equiv \int e^{-r/\lambda}S(r)dr \qquad (3.7)$$

$$I_2(r) \equiv \int e^{r/\lambda}S(r)dr \qquad (3.8)$$

$$I_0 \equiv \frac{I_1(1)e^{1/\lambda} - RI_2(1)e^{-1/\lambda}}{e^{1/\lambda} - Re^{-1/\lambda}} \qquad (3.9)$$

$$R \equiv \frac{(A/a) - 1}{(A/a) + 1} \qquad (3.10)$$

While this is a complicated set of equations, it is semi-analytical, and can be solved numerically rather easily. The basic output of the set of equations is the impurity density profile (n(r)), the value at the LCFS, n(r=1), being the value of most interest. With that density, the 'screening time' discussed in the last sectioned is obtained by first multiplying n(1) by the area a, to convert the 1-D density (m^{-1}) to actual density (m^{-3}), then multiplying it by the confined plasma volume, to obtain the number of ions in the core, and finally dividing by the impurity atom influx rate. To obtain this result, the equations need to be given the background plasma density and temperature profiles, the parallel impurity velocity, the perpendicular diffusion coefficient, the distance from the puffing location to the divertor plate, the distance from the midplane to the x-point, and the area ratio (R).

Figures 3.9 and 3.10 show the solutions to these equations for a given set of parameters for both puffing of methane and Nitrogen. The background plasma is given values of 8 eV and $10^{19}/m^3$ at the puff location, with e-folding lengths of 6 and 8 millimeters for temperature and density

Figure 3.9: NO-RISC Case Ion Source Solution
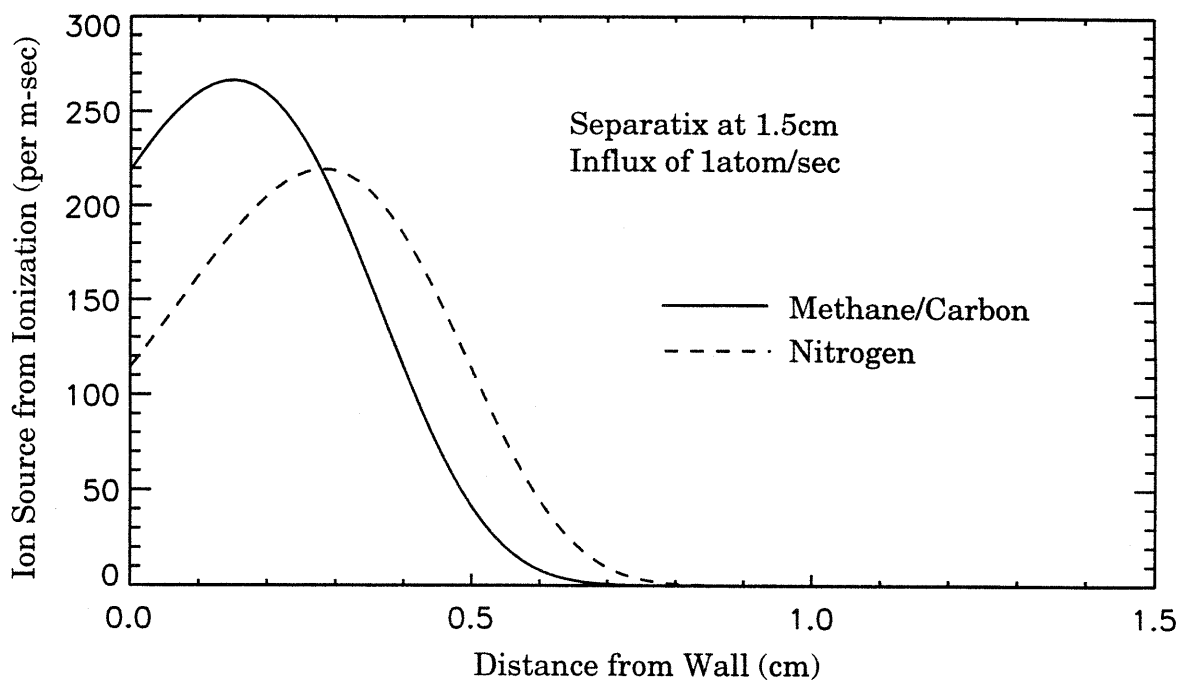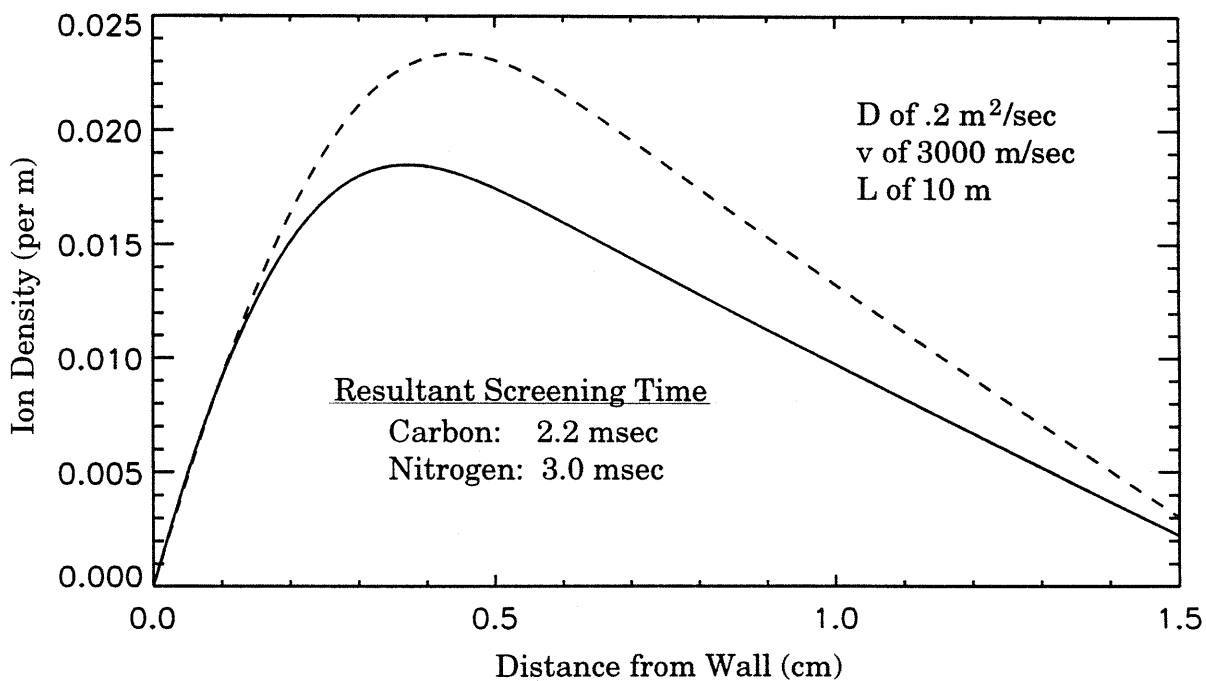

Separatix at 1.5cm
Influx of 1atom/sec

—— Methane/Carbon
- - - - Nitrogen

Figure 3.10: NO-RISC Case Ion Density Solution

D of .2 m^2/sec
v of 3000 m/sec
L of 10 m

Resultant Screening Time
Carbon: 2.2 msec
Nitrogen: 3.0 msec

respectively. L is set to be 10 m, l to 1.5 cm (a typical value for puffing at the inner-wall midplane), D to .2 m²/sec (thought to be a typical value for C-Mod), v to 3000 m/sec (a velocity on the order of the sound speed). For an atomic injection rate of 1.0 per sec, the ion source rate and ion density profiles are presented in the figures.[7] (Thus, for the profiles at any given injection rate, just multiply these curves by that injection rate.) For this case, screening times of 2.2 and 3.0 msec are found for Carbon and Nitrogen respectively (screening time is independent of puff rate). As is observed experimentally, Carbon is better screened (though experiments do seem to show Carbon screening times even lower than this as a fraction of that for Nitrogen).

Solving the equations over a range of parameters yields screening times varying from about .1 msec up to about 10 msec, in the same range of the experimental values shown in figure 3.7. If this can be taken as somewhat of a vindication for the NO-RISC model (looking for perfect agreements would be difficult not only because of all the assumption in the model, but also because of the large uncertainties in the experimental measurements), then this discussion has provided a reasonably clear picture of the transport of non-recycling impurities in the edge region. Additionally, it shows some of the ways in which the screening time can be affected. For example, decreasing the distance to the plate (L), or increasing the distance to the last close flux surface (l) will reduce the screening time. This is why strong puff location dependence can be expected, and specifically why impurity puffing in the divertor or private

---

[7]The methane and molecular Nitrogen ionization rate coefficients used are obtained from integrating cross-sections over a Maxwellian. The cross sections were obtained from K.L. Bell, et al, "Electron Impact Ionization of Molecules", Queen's University of Belfast, 1990 (unpublished).

flux region can be expected to give the best screening (transported quickly to the plate, long way to make it to the core plasma). Modeling of impurity transport in the Alcator edge is ongoing, with emphasis being placed upon the use of DIVIMP (see chapter 5) to obtain the effects of geometry and a fuller treatment of transport phenomena not provided by a model such as NO-RISC.

Chapter 4
Plumes

The basics of impurity plume experiments were discussed in section 2.1. Methane, Nitrogen, and Helium are injected into the Alcator edge region at various locations with the resultant impurity emission at the puffing location observed with one (or both) of the Culham cameras.[1] C-II and C-III line emission has been observed during methane puffing, N-II and N-III during Nitrogen, and He-I and He-II during Helium puffs. To clear any confusion on terminology, C-II refers to emission by the singly ionized Carbon, He-I emission by neutral Helium atoms, and so on. The brightness of the line emission and the density of the impurity charge state are generally taken as synonymous. In other words, the background plasma is assumed uniform over the extent of the plumes such that the density of the charge state will be proportional to its emission. The experiments and their analysis have focused on the inner-wall midplane (location A in figure 3.1) with the outboard midplane Culham Camera. This is has been done for two reasons: it is the puffing location that has the

---

[1]This chapter is an updated and expanded version of D. Jablonski, et al, "Observation of Impurity Injection Plumes in the Scrape-off Layer of the Alcator C-Mod Tokamak", Bulletin of the APS, 40(1995), Oct, 6F3; this chapter as well as the analysis of the next two appear in condensed form in D. Jablonski, et al, "Local Impurity Puffing as a Scrape-off Layer Diagnostic on the Alcator C-Mod Tokamak", Journal of Nuclear Materials, to be published.

best view available of it, and further, the simplified geometry and scrape-off layer characteristics (little variation along a field line being far from the divertor plates) at the inner-wall provide for the most straightforward interpretation and modeling of the plumes.

The experiments have been performed in single-null diverted Deuterium discharges with 800 kAmps of plasma current and a 5.3 Tesla magnetic field on axis. Core densities for these shots have ranged from 1.0 to $2.6 \times 10^{20}/m^3$. Plumes have been recorded in both upper and lower x-point configurations, and in both normal and reverse field discharges. For reverse field shots, the current and magnetic field are run counter-clockwise (CCW) rather than the normally used clockwise (CW) direction. The direction refers to that observed from the top of the machine. In CW configured shots, the ion ∇B drift points downward, in CCW shots it points upward (the discharges in the two configurations show very different behaviour, behaviour often attributed to the direction of the ∇B drift, as well as other magnetic field direction dependent drifts).[2]

An example of an inner-wall midplane plume is given in figure 4.1, showing the outboard midplane Culham camera view of a Nitrogen injection through a N-II filter and the corresponding contour plot. The shape of the plume is typical, comet-like, extending along the magnetic field line towards the strike-point. The plume is seen to fade with distance away from the puffing location, the impurity ions getting ionized to the next charge state (in this case to N-III). Figure 4.2 contrasts plumes in upper and lower x-point shots (the upper x-point shot utilizing the top divertor), in these cases C-II plumes during methane injection. One can see that the

[2]I.H. Hutchinson, et al, "The Effects of Field Reversal on the Alcator C-Mod Divertor", Plasma Phys Control Fusion, 37(1995), pp. 1389-1406.

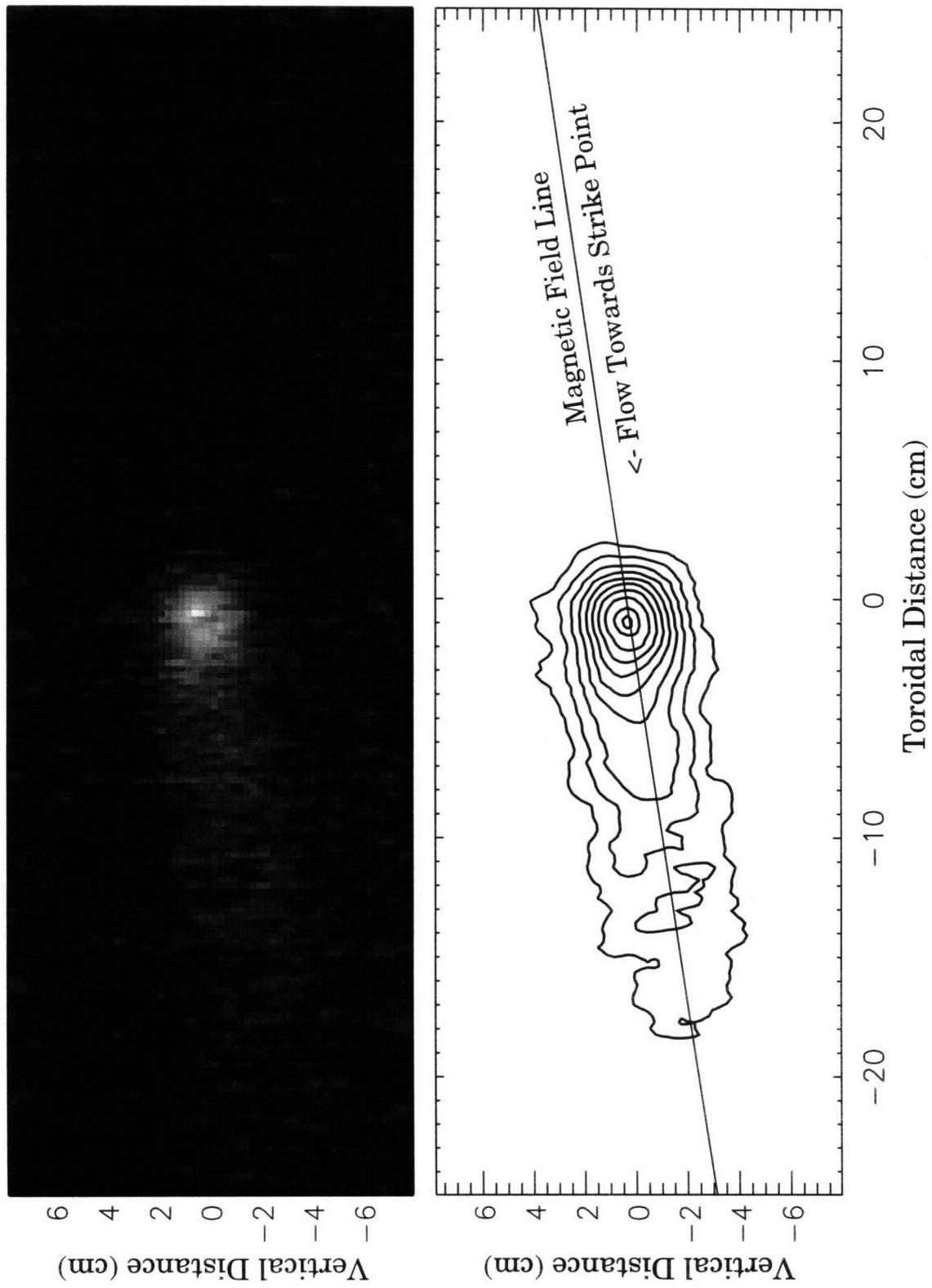Figure 4.1: N-II Emission during Nitrogen Puff at Inner-wall

Figure 4.2: C-II Plumes with Lower and Upper X-Points
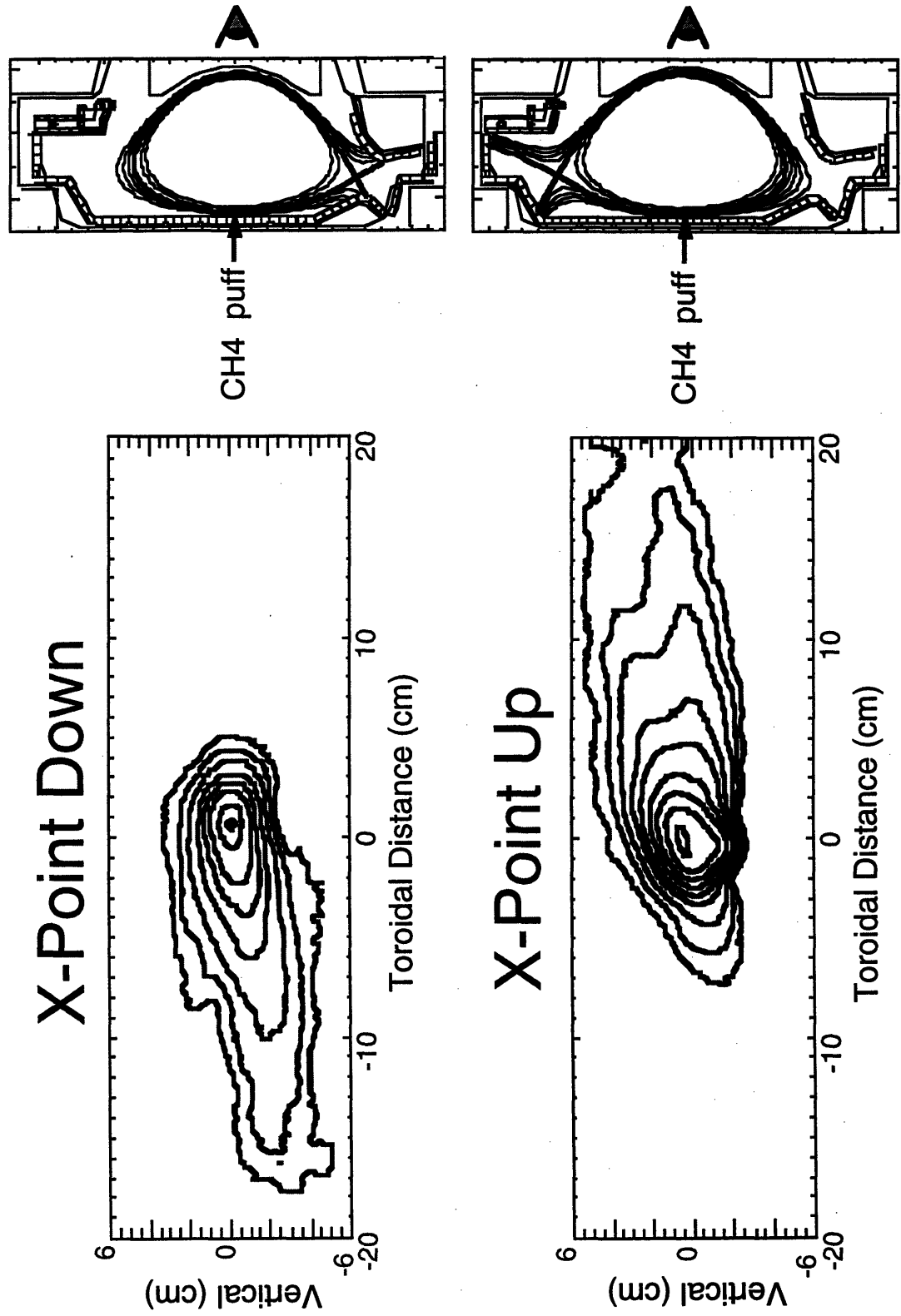
upper x-point shot also displays pluming action along the field line, this time towards the upper strike point. Such behaviour is seen with upper and lower x-points independent of magnetic field direction, and is observed with the Helium impurity ion plumes as well (exceptions will be discussed in chapter 6). It has also been witnessed at the other locations at which plumes have been recorded. The asymmetry is indicative of a background plasma ion flow sweeping the impurity ions along (the velocity being imparted to the impurity ions through coulomb collisions). As discussed in section 1.3.2, a background ion flow towards the closest strike point along the magnetic field is in fact expected. One might posit other ideas on why the plumes do display such asymmetry, perhaps through some kind of local radiative cooling phenomenon. Such suppositions are disproved by the observation that the shape of the plumes does not change with the quantity of the impurity injected.

This does bring up another issue however: that of 'trace' injection. Ideally, these impurity puffs would be trace, i.e. non-perturbative to the background plasma. For the methane injections, this appears to generally be the case, no discernible changes to plasma parameters are seen when Carbon has been introduced. For Nitrogen and Helium puffs however, disturbances are observed. To see the Helium emission with the Culham Cameras, quantities need to be puffed (roughly 5×10^{19} atoms/sec) which make the Helium NINJA injection a not insignificant fueling source for the plasma, giving it a Helium minority of a few percent. A high Helium minority is not deleterious to the discharges, in fact pure Helium discharges are often run in C-Mod purposely, but the plasma characteristics are slightly altered. Nitrogen does not need to be puffed more strongly than methane to be seen (roughly 1×10^{20} atoms/sec), but

Nitrogen tends to be less well screened from the central plasma, usually inducing detachment when introduced in these experiments, even in low density discharges (continuously detached H-Modes have in fact been induced recently in C-Mod with NINJA Nitrogen puffing).[3] Note that the Nitrogen and methane puffing rates are higher than that for Helium. Even so, Helium makes it into the core plasma in large amounts while Carbon and Nitrogen do not (if either were puffed heavily enough to make it into the plasma in as large of quantities as Helium, the plasma would disrupt in short order). This phenomenon has to do with Helium's low mass (giving it a relatively high thermal velocity) and low ionization cross-section relative to the other two gases, and to the aspects of recycling versus non-recycling impurity behaviour discussed in the last chapter (injected Carbon and Nitrogen are effectively pumped out of the chamber by the solid surfaces while Helium, a recycling impurity, is not).

Figures 4.3 and 4.4 show impurity plumes at locations other than the inner-wall midplane. As with the plumes shown in figures 4.1 and 4.2, these indicate background Deuterium flows toward the appropriate strike-points. Figure 4.3 shows an C-II image taken during simultaneous methane puffing at the inner-wall midplane and on top of the divertor nose (locations A and C in figure 3.1) during an upper x-point discharge. Both plumes show flow towards the upper-strike point. Notice the slightly different angle of the two, resulting from the difference in magnetic field angle at the locations. In figure 4.4, simultaneous Nitrogen puffs at the inner and outer divertor (locations C and J) are performed while viewed with the top Culham Camera through a N-II filter. It is seen rather

---

[3]B. Lipschultz, et al, "Modification and Control of Divertor Detachment in Alcator C-Mod", Journal of Nuclear Materials, to be published.
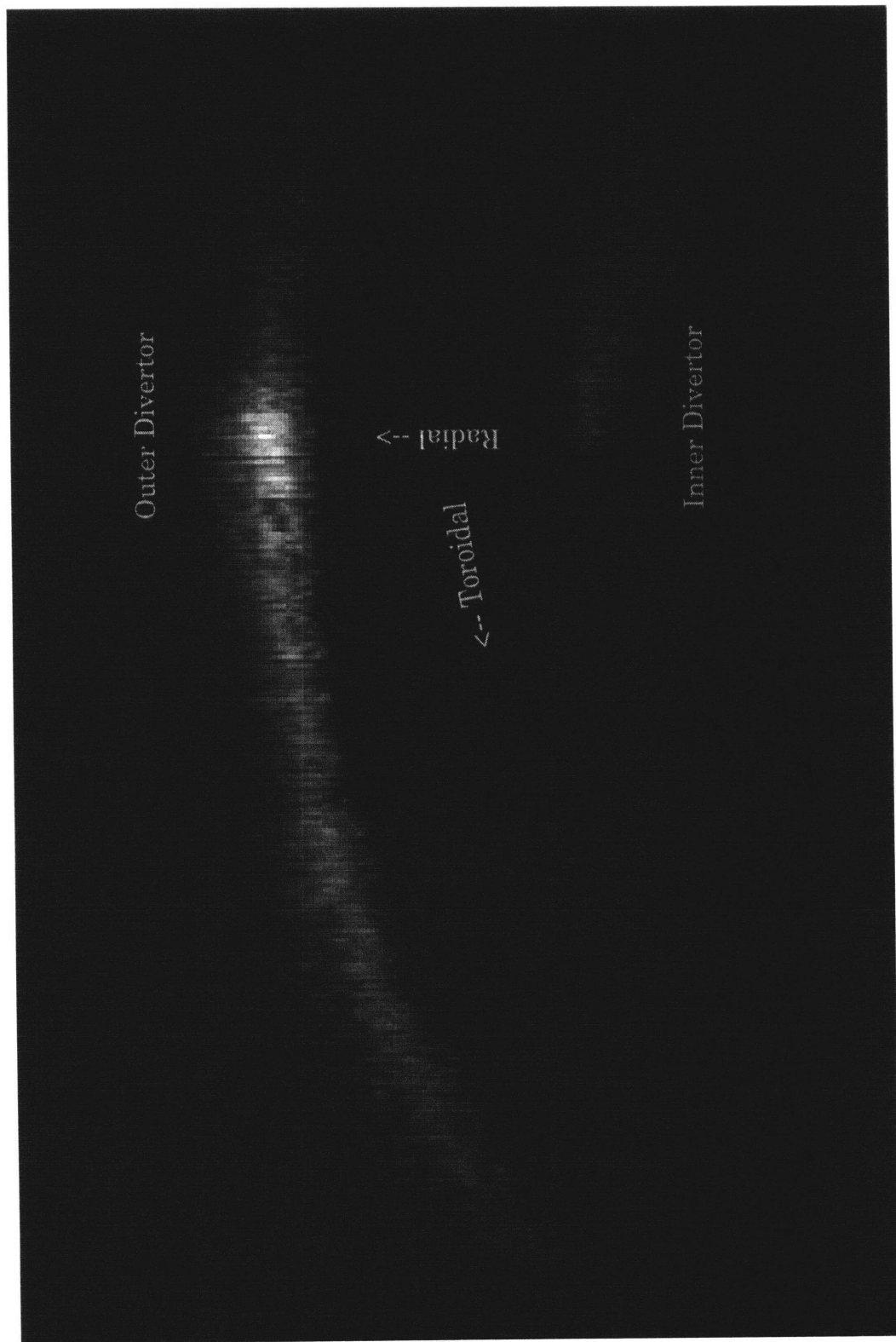
Top of Machine
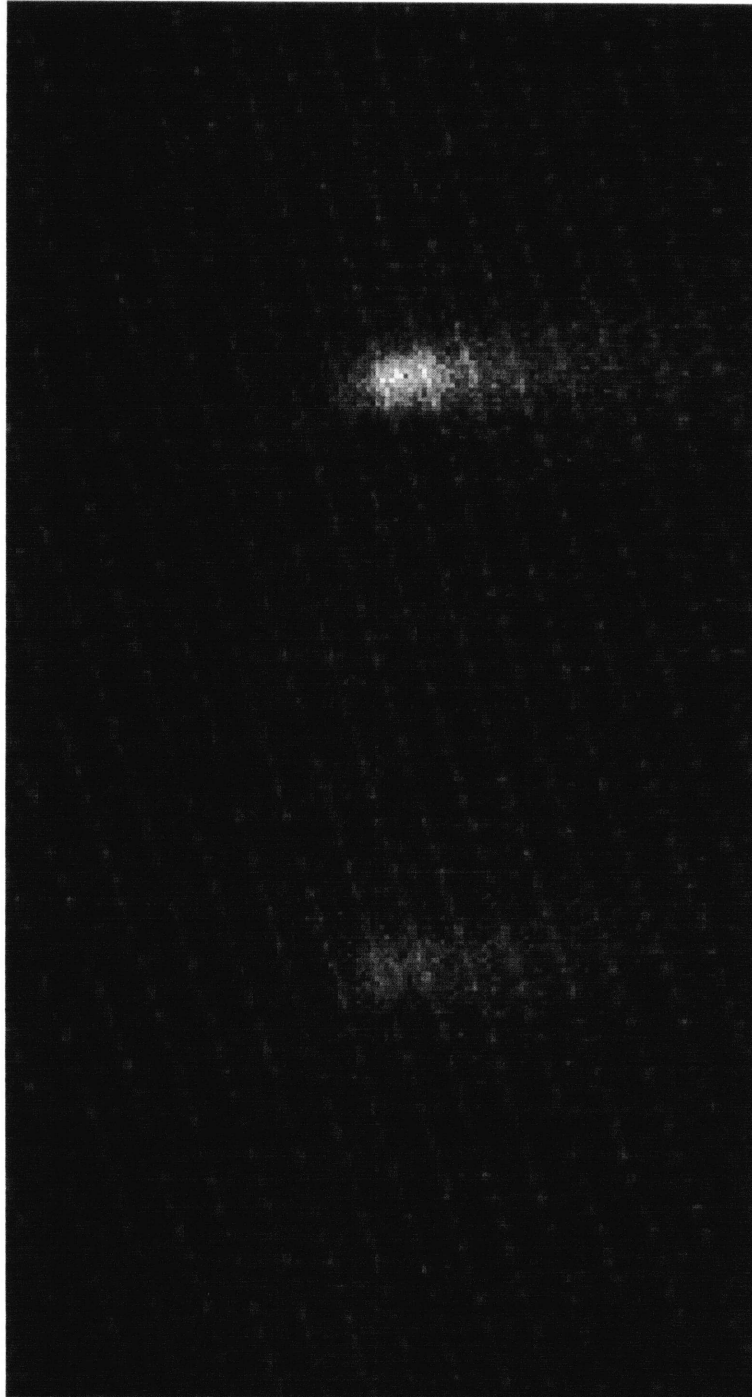
Bottom of Machine

Figure 4.3: Carbon-II Plumes at Inner-wall Midplane and on Inner Divertor Nose

Figure 4.4: Nitrogen-II Plumes in the Lower Divertor

Outer Divertor

Radial -->

<-- Toroidal

Inner Divertor

dramatically that the plumes flow in opposite directions, the outer divertor plume CCW, the inner divertor plume CW. The geometry is such (with the current and magnetic field in the standard CW direction) that each plume is pointing towards the respective strike point (indicating the expected background Deuterium ion flow in that direction). The same behaviour is seen at other locations as well, and is even seen in limited shots (in which the inner-wall is used as a rail-limiter), for which the plumes flow along the field towards the nearest point at which the field line strikes a solid surface. One other facet of figures 4.3 and 4.4 is the difference in image quality. The first was recorded onto videotape and later digitized. The second was digitized directly with the PC system discussed in section 2.1.2.

If one integrates the plumes across the magnetic field (to obtain the emission profile along the field line), profiles like those shown in figure 4.5 are obtained. Both C-II and C-III profiles are plotted. Their relative shapes are typical, with the C-III profile being broader. This broadness is a product of the C-III having gone through the C-II charge state (the primary source function for C-III is the ionization of C-III, hence the profile could not be any less broad) and having had a greater amount of time to equilibrate in energy and velocity with the background deuterium ions. Though no C-I or N-I plumes were recorded, He-I emission was observed during Helium injections at the inner-wall midplane. The profile of one of these He-I plumes is shown in figure 4.5. The emission pattern of neutral Helium is circular in shape, a symmetric gaussian in profile with a FWHM of about 3.5 cm, as shown in the figure. The C-I and N-I emission patterns, while not observed, are thought to be very close to that of the He-I, an assumption somewhat backed-up by modeling with the DIVIMP code (see chapter 5).

Figure 4.5: Impurity Ion Emission Profiles
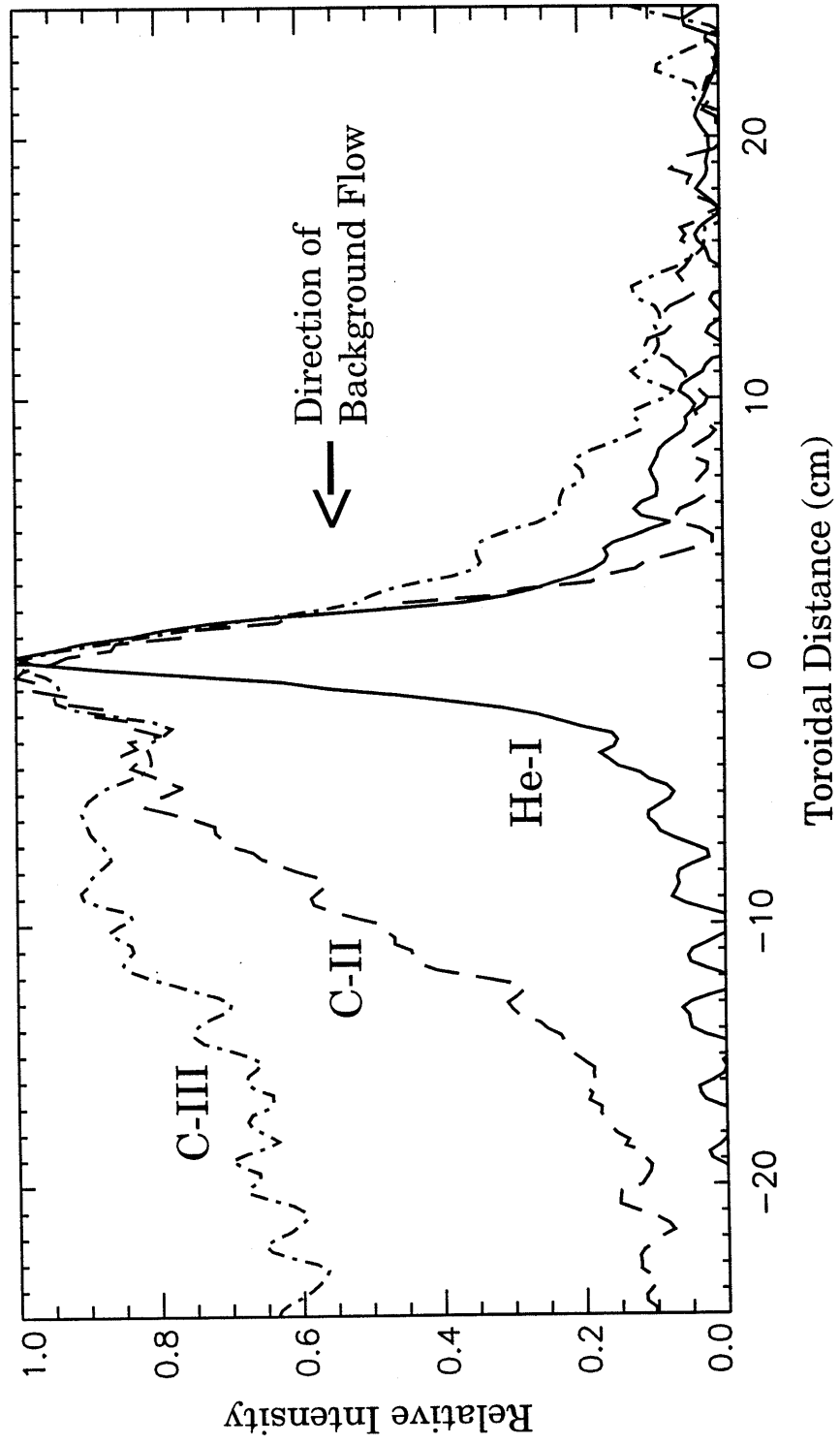
As discussed in section 1.3.2, in addition to the forces pushing the impurity ions along the field line, there are forces which push them perpendicular to it. If one compares the axis of the plume tail with the magnetic field line, deviations are generally seen, indicative of perpendicular ion drift. This is dramatically displayed in the relatively symmetric C-III plume in figure 4.6. The deviation in this case is upward on both sides of the puffing location, indicating an upward drift. Notice also that the plume axis changes as one moves away from the center, beginning with a larger angle relative to the field line and asymptoting to a shallower one. The parallel velocity of the ions increases as they move away from the center and equilibrate in temperature and velocity with the background. With a constant perpendicular drift, a bird of prey type shape in the particle trajectories is produced, as is witnessed in the figure.

On a somewhat different topic, figure 4.7 shows the D-Alpha emission recorded by the side Culham camera during a Deuterium puff at the inner-wall midplane. The shape is similar to those of the impurity plumes. Two major differences need be pointed out however. The first is that this is neutral emission, meaning that if it is flow that is inducing this shape, it must be imparted from the background to the neutrals through charge exchange and/or elastic collisions.[4] The second is that very high Deuterium puffing rates need to be used to observe the plume tail (10^{21} molecules/sec or higher). At lower injection rates the plume tail is not seen. This does not necessarily mean it is not there, it may just not be visible (the center of the plume saturates the camera in figure 4.7; the ratio of the brightness at the center to that along the tail is much higher than the

---

[4]For further discussions of ion-neutral coupling in the C-Mod edge, see B. LaBombard, et al, "Evidence of Strong Plasma-Neutral Momentum Coupling in the Alcator C-Mod Divertor", <u>Bulletin of the APS</u>, 40(1995), Oct, 3P34.

Figure 4.6: Magnetic Field Deviation of a C-III Plume
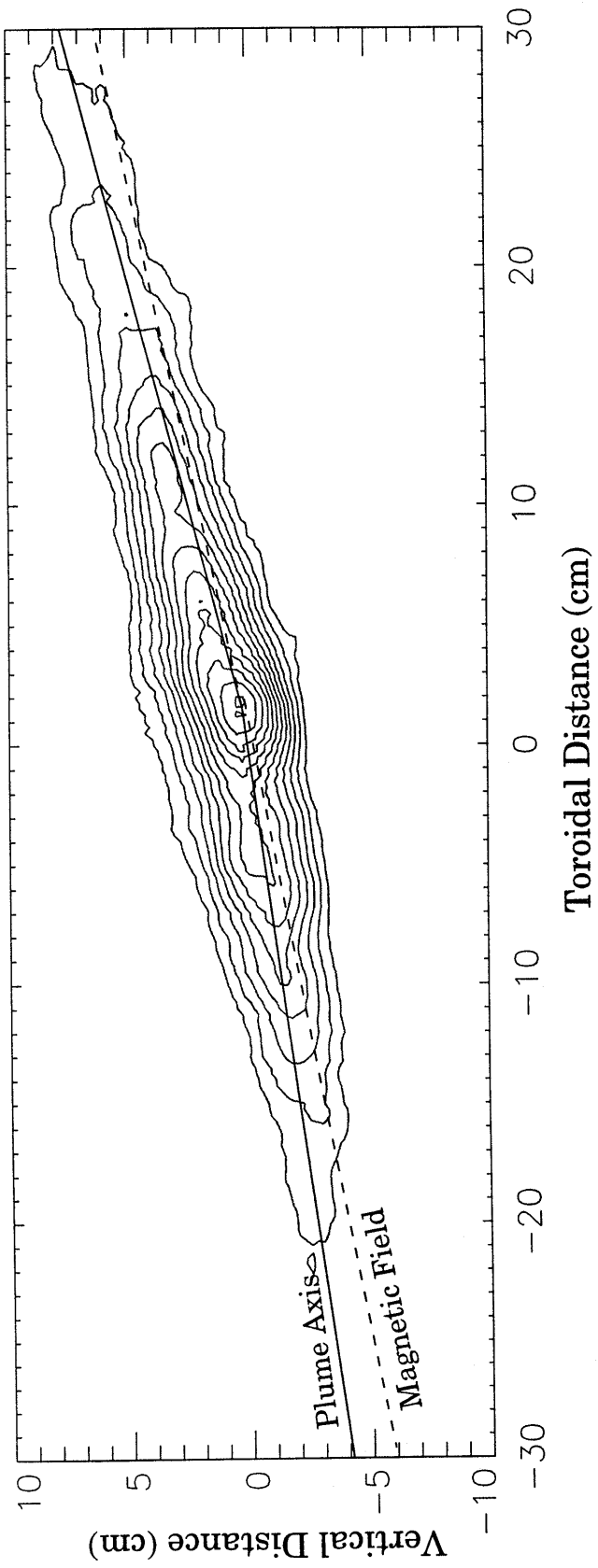
Figure 4.7: D-Alpha Plume during Deuterium Injection at Inner-wall
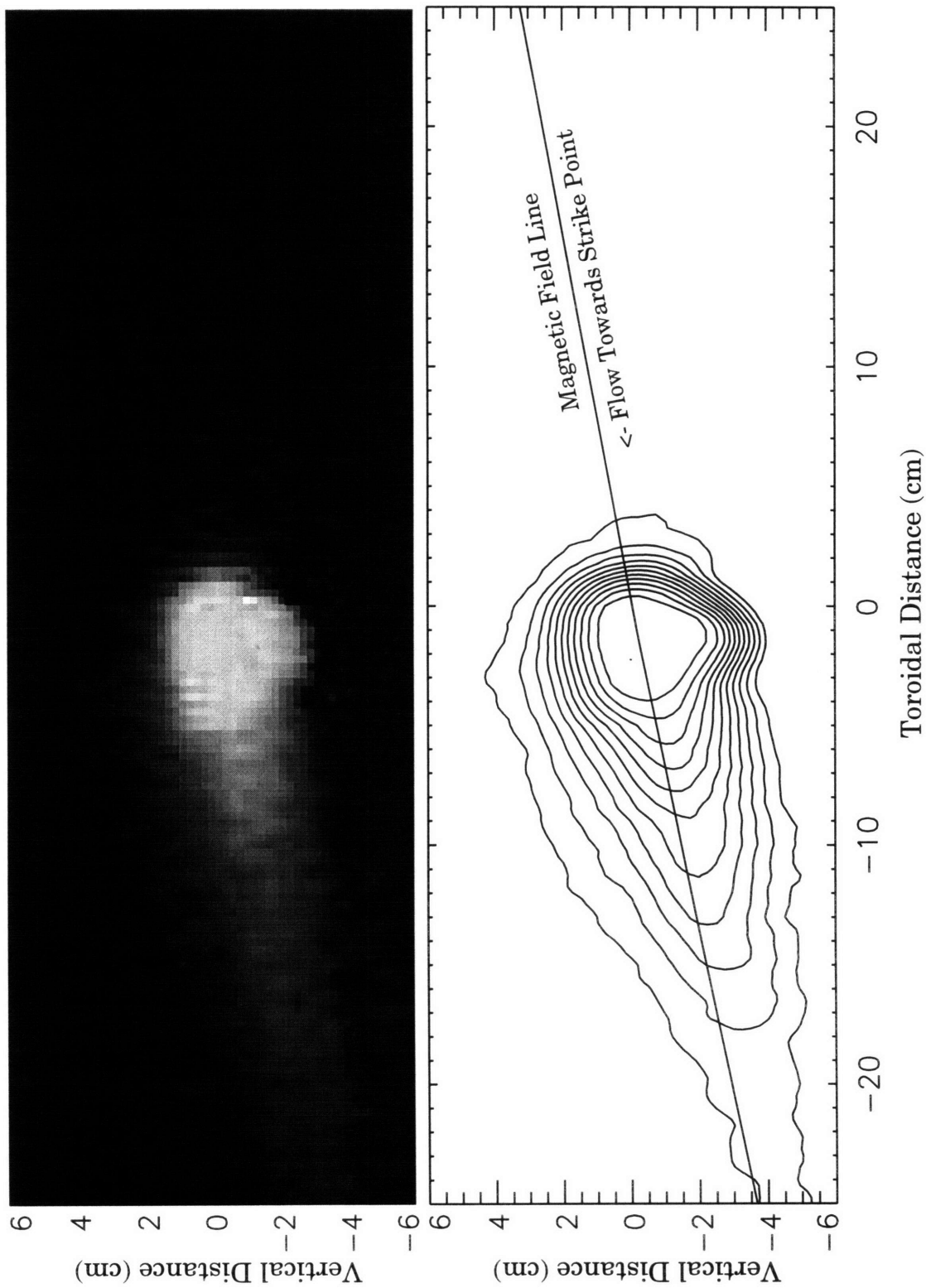
image would indicate). The phenomenon is likely worthy of further study, but it would require a camera of higher resolution and dynamic range so that both the peak and the tail could be recorded simultaneously.

Chapter 5
Models

A fluid model has been constructed to extract information about the background plasma from the shape of the impurity plumes discussed in the last chapter. To benchmark this model, a Monte Carlo code is employed. The construction of the fluid model is discussed in the first section, DIVIMP, the Monte Carlo code, in the second, and the benchmarking between the two is described in the third.

Both models make use of the simplified geometry in the region of the NINJA capillary at the inner-wall midplane (location A in figure 3.1). The magnetic field lines there are approximately parallel to the wall, making the use of a simple slab geometry possible, as shown in figure 5.1. The three Cartesian dimensions chosen are: parallel to the field line/toroidal (x), perpendicular to the field line/poloidal (z), and radial (r). The origin is chosen to be the puff location. An additional simplification used in both models is to assume that because the location is far from the strike-points, the parameters of the background plasma are uniform on each flux surface, only dependent upon the radius (r).
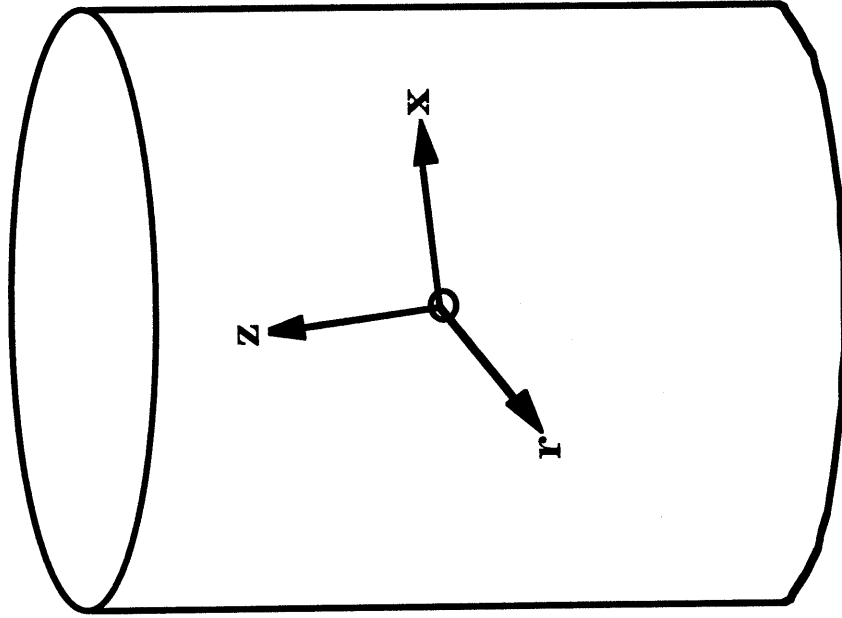
Figure 5.1:
Axes for Slab Geometry

x: Toroidal (par to $\underline{B}$)

z: Poloidal

r: Radial

Origin: Puff Location
of IWM Capillary

Alcator C-Mod Central Column (Inner-wall)

5.1 Plume Fluid Model

As viewed through the side Culham camera, the transport of the injected impurity ions appears two dimensional (the radiation being integrated over the radial). This leads one to implement a two dimensional model to characterize its shape. To get to the starting equations, a number of assumptions need be made, the first being the use of a fluid model in the first place. Because the impurity density is relatively low, the impurity ions cannot be properly considered self-collisional, hence the fluid characterization can be brought into question. While the impurity ions do not have high self-collisionality however, they do have high collisionality with the background plasma ions. Because this cross-collisionality somewhat validates the use of local fluid parameters to describe the impurity ions, a fluid approach is on firmer footing than one may at first think. Ultimately, the test of the utility of the model is whether it seems to provide useful information (it does), whether or not the characterization is strictly proper.

The next assumption is that the background plasma is uniform and two dimensional. The first of these is reasonable in light of the strike-point being far away (on the order of 10 m). The second is made out of necessity, as the camera system integrates over the emission profile in the radial direction. Both of these assumptions are necessary to be able to take the impurity ion density as proportional to their emission. By taking these factors into account we effectively assume that the neutral impurity atoms launched from the capillary are all ionized at a flux surface which has uniform background density and temperature, that the ions remain on that flux surface, and that their behaviour can be characterized with a fluid picture. This picture, while leading to the equations that follow, is of

course not the case in reality. In reality, the two-dimensional plumes observed are radially integrated emission profiles. The 'uniform' plasma parameters over the extent of the plume are in reality those values in some radially averaged sense (one can derive expressions for these averages, but the expressions are complicated and of no effective use).

The steady-state continuity, momentum and energy equations utilized for an impurity ion charge state are:

$$\nabla \cdot (\underline{\Gamma}) = S_n - nn_e < \sigma v >_i \tag{5.1}$$

$$\frac{\partial}{\partial x}(nv_x^2 + \frac{nT}{m}) = S_p + \frac{n}{m}F_x - nv_x n_e < \sigma v >_i \tag{5.2}$$

$$\nabla \cdot (\frac{1}{2}nv^2\underline{v} + \frac{5}{2}\frac{nT}{m}\underline{v}) = S_E + n\frac{T_D - T}{\tau_T} +$$

$$\frac{nv_x}{m}F_x - (\frac{1}{2}nv^2 + \frac{3}{2}\frac{nT}{m})n_e < \sigma v >_i \tag{5.3}$$

The cross-field (z) momentum equation is not included (it will not be needed). Unscripted variables (n, v, T, Γ, m, and Z) refer to the values for the impurity ions. The S terms are the sources, coming from ionization of the lower charge states. n_e and T_D are the background plasma electron density and ion temperature, both assumed constant. The loss terms result from ionization to the next charge state, the rate being a function of the background plasma density and electron temperature.[1] The forces exerted upon the impurity ions along the field lines is represented by F_x. This includes those forces discussed in section 1.3.2, specifically the friction with the background plasma (form given in equation 1.2), the electric field force (equation 1.10), and the background temperature gradient forces (equation 1.11). The pressure gradient force is already included in the left hand sides of equations 5.2 and 5.3. F_x can also be thought to include all other

---

[1]The ionization rate coefficients for most of the modeling are obtained from K.L. Bell, et al, "Atomic and Molecular Data for Fusion, Part I", UKAEA Report CLM-R216, 1982. For some of the comparisons of the fluid model with DIVIMP, the ADAS coefficients are used, ref: H.P. Summers, "Atomic Data and Analysis Structure (ADAS)", JET, 1994.

momentum sources and sinks, such as the cross-field source of parallel momentum, which has been left out of the left hand side of equation 5.2. Only those forces along the field line are included in equation 5.3 since forces perpendicular to it cause no change in the ion energy. For the τ's, which are the equilibration times of the impurity ions with the background plasma temperature and velocity, the Spitzer times are employed, which, for a background plasma of Deuterium, are:[2]

$$\tau_v = \frac{A^2 T_D}{9.57 \times 10^{-14} n_e (2+A) Z^2 \ln \Lambda} \qquad (5.4)$$

$$\tau_T = \frac{A T_D}{1.93 \times 10^{-13} n_e Z^2 \ln \Lambda} \qquad (5.5)$$

where A is the mass of the impurity ions in amu, n_e the density in m^{-3}, T_D the Deuterium ion temperature in eV, and the times are in units of seconds.

There are two assumptions made to reduce the number of parameters that are needed to solve these equations. The first is to assume that the Deuterium and electron temperatures of the background plasma are equal. This is not necessary substantiated by experimental reality, but there is currently no measure of edge measurement of ion temperature on C-Mod, and the ratio of electron to ion temperature is not known. The second is to fold all of the forces given by F_x into the frictional force to create an 'effective' background deuterium velocity:

$$v_D^{\text{eff}} = v_D + Ze\tau_v E_x + \tau_v \alpha_e \frac{\partial T_e}{\partial x} + \tau_v \beta_i \frac{\partial T_i}{\partial x} + \dots \qquad (5.6)$$

with the term F_x being replaced by the frictional force term given in equation 1.2. The effective Deuterium velocity assumes the value necessary to have all the momentum source given by the frictional term. (If friction is

[2] L. Spitzer, Jr., Physics of Fully Ionized Gases, New York: Interscience Publishers, Inc., 1956, pp. 76-81.

the dominant force, as it is expected to be, the effective Deuterium velocity will essentially be the same as the Deuterium velocity.) Henceforth, the 'eff' superscript will be dropped, taken as understood.

Note that the equations, unlike those used for the NO-RISC model discussed in section 3.2.2, are only for an impurity ion charge state, not for all the impurity ions. Though the equations can be solved for any charge state, the analysis is limited to singly ionized impurities. Because the impurity neutrals ionize at room temperature (assuming no significant charge exchange, recombination, or dissociation energy), the momentum and energy source terms can be set to zero. The particle source term is taken as a circular gaussian with a FWHM of 3.5 cm (as discussed in chapter 4, such is the shape of the neutral emission for injected impurities). It should be noted that while the shape of the particle source term is known (or presumed to be known), its absolute value is ambiguous. Because of this, only the shape of the density (n) profile can be determined. Plots of impurity density that follow will be normalized to unity at the peak value.

5.1.1 Parallel Solution

To obtain the parallel set of equations, 5.1 and 5.3 are integrated across the field line (z direction). The impurity density (and hence perpendicular flux) are taken to go to zero as positive or negative infinity are approached in the z direction, causing the perpendicular terms on the left hand sides of equations 5.1 and 5.3 to drop out. This will be strictly true only if recombination is ignored (so that as one moves away from the region of the source, all the impurity ions for the charge state become ionized to

higher charge states). Dropping the x subscripts, one essentially arrives at the one-dimensional continuity, momentum and energy equations:

$$\frac{d}{dx}(nv) = S_n - nn_e < \sigma v >_i \qquad (5.7)$$

$$\frac{d}{dx}(nv^2 + \frac{nT}{m}) = n\frac{v_D - v}{\tau_v} - nvn_e < \sigma v >_i \qquad (5.8)$$

$$\frac{d}{dx}(\frac{1}{2}nv^3 + \frac{5}{2}\frac{nT}{m}v) = n\frac{T_D - T}{\tau_T} +$$

$$nv\frac{v_D - v}{\tau_v} - (\frac{1}{2}nv^2 + \frac{3}{2}\frac{nT}{m})n_e < \sigma v >_i \qquad (5.9)$$

where n, T, v, and S_n are understood to be poloidally integrated values. Three inputs are needed (n_e, T_D, and v_D) to solve the equations for the three outputs (profiles of n, T, and v along the field line). Boundary conditions are a bit problematic because of the distance from the plate coupled with the geometry used for the problem which is essentially that of an infinite slab. One is forced to use boundary conditions at plus and minus infinity where the density (n) and the derivatives of temperature and velocity (T and v) go to zero. A coordinate transformation is performed to make the values at infinity accessible, namely

$$\frac{x}{L} = \frac{y}{1 - y^2} \qquad (5.10)$$

where L is a constant defined to give the desired discretization. This transform is convenient, mapping y=0 to x=0 and y=±1 to x=±∞. After the transform, the equations can be solved using a packaged Newton routine.[3]

The shapes of the profiles found with these equations will be determined by the competing effects of the loss terms (from ionization) and the Spitzer times. Figure 5.2 shows the relative size of the ionization rate

---

[3]The equations are solved in the IDL (Interactive Data Language) programming language, version 4, a derivative of APL produced by Research Systems, Inc, Boulder Colorado. The Newton routine used is essentially that described in section 9.7 of W.H. Press, et al, Numerical Recipes in C: The Art of Scientific Computing, New York: Cambridge University Press, 1992.

Figure 5.2: Rate Coefficients for C-II Ions
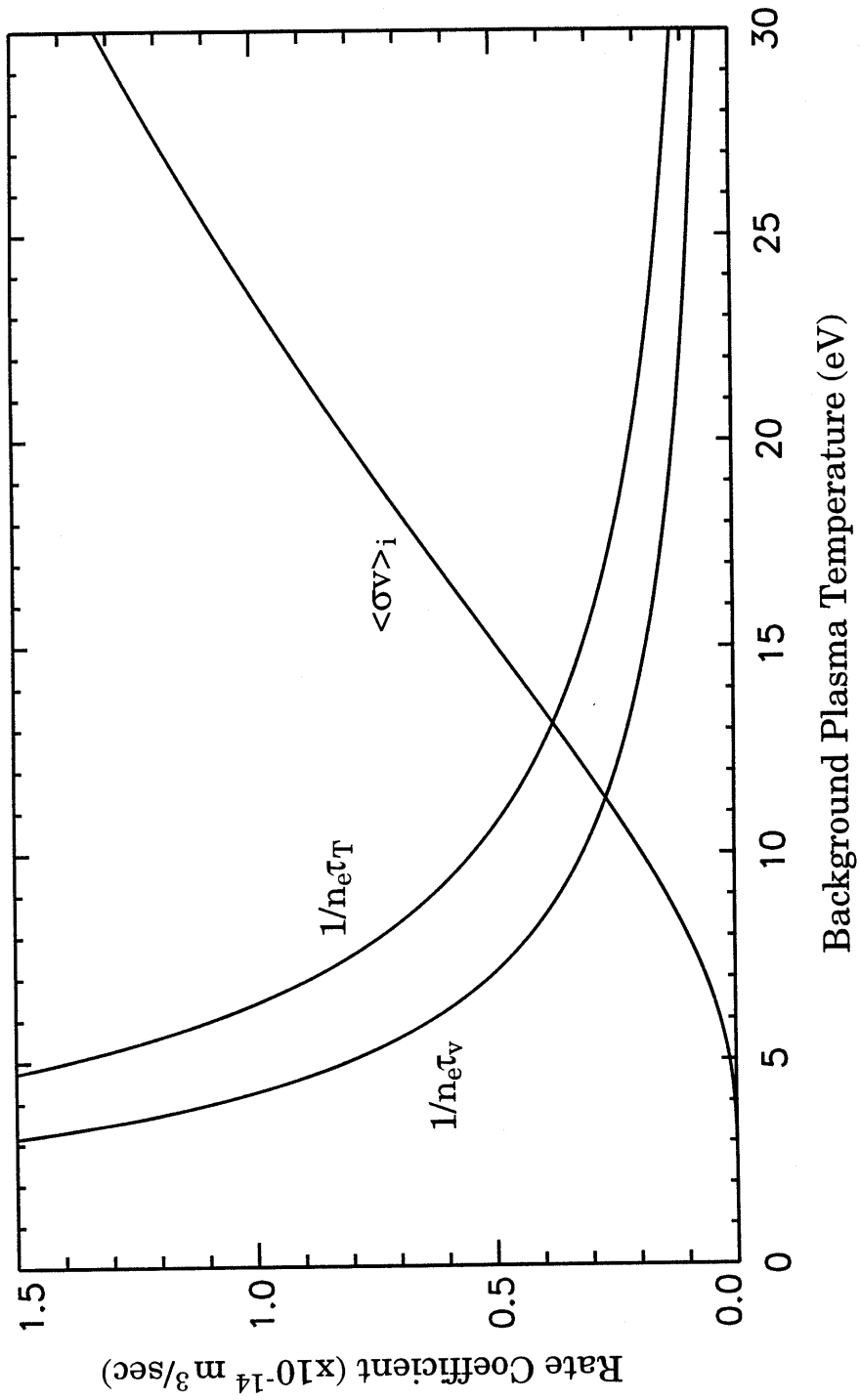
coefficient and the $1/n\tau$'s for the Spitzer times for the C-II ions. At low temperature, the Spitzer 'rates' are seen to be much larger than the ionization rate, leading one to expect the ions to quickly equilibrate in density and temperature with the background, giving a broad density profile. At high temperature, where the Spitzer rates are lower and the ionization rates higher, the opposite is expected, with narrow density profiles due to the C-II ions becoming ionized before picking up much velocity or energy from the background.

Figure 5.3 gives the calculated profiles for two cases of C-II ions, both with background densities of $5\times10^{19}/m^3$ and background Mach numbers of .1 (Mach number is defined in section 1.3.2), but one with an 8 eV electron temperature, the other with 15 eV. The density profile of the 8 eV case is seen to be much broader, as expected. Both profiles show a degree of asymmetry resulting from the background Deuterium flow. The temperature and velocity profiles show the 8 eV case to approach equilibrium with the background deuterium much quicker (over a shorter distance). The impurity temperature asymptotes to that of the background ions. The velocity approaches a value governed by the interaction of the impurity pressure gradient force and the coulomb collisionality.

To obtain a clear picture of the asymptotic values, limits of equations 5.7-9 can be found. Far from the source, the particle source term can be neglected (assumed to drop off as a gaussian), and, as mentioned above, the gradients of temperature and velocity approach zero. Using these limits,

Figure 5.3: C-II Ion Profiles for Background $5 \times 10^{19}/m^3$ and Mach .1

Temp of Case
—— 8 eV
– – – 15 eV

Relative Density

Velocity Relative to Background

Temp Relative to Background

Toroidal Distance from Puff Location (m)
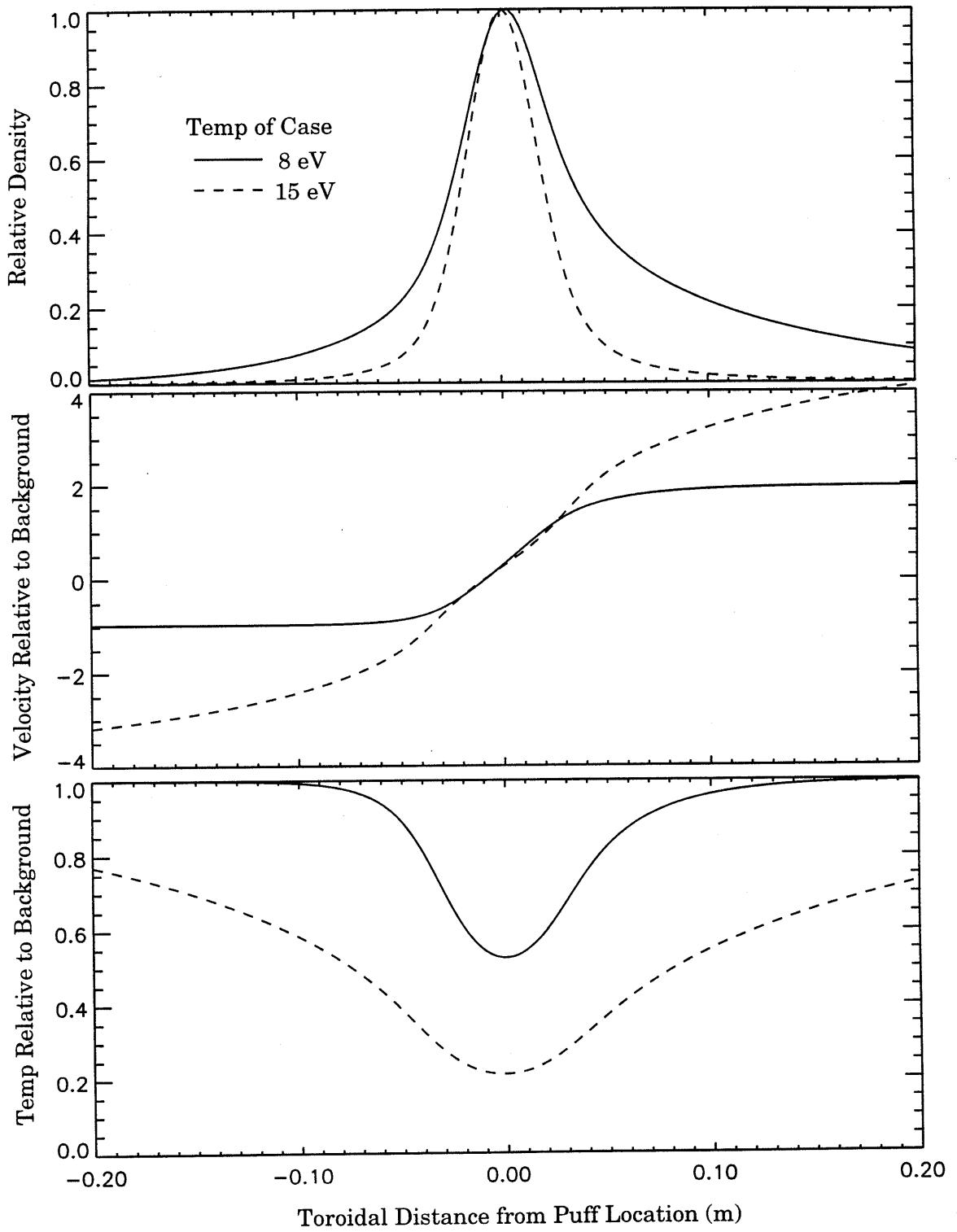
the equations reduce to:

$$T = T_D \tag{5.11}$$

$$M = \frac{1}{2} M_D (\frac{m}{m_D})^{1/2} \pm \frac{1}{2} [M_D (\frac{m}{m_D})^{1/2} + 2n_e \tau_v < \sigma v >_i]^{1/2} \tag{5.12}$$

$$n \propto \exp[-(\frac{m}{T_D})^{1/2} \frac{n_e < \sigma v >_i}{M} x] \tag{5.13}$$

where the Mach number in the expression for density is that given in 5.12. As was seen in the cases of figure 5.3, the temperature asymptotically approaches that of the background. For velocity, the positive solution corresponds to that at plus infinity, the negative solution to that at minus infinity. For cases with no background flow, the impurity velocity is governed only by the pressure gradient force (represented by the second term under the square root in 5.12), giving the same asymptotic value in both directions (with change of sign). A positive background flow increases the asymptotic impurity velocity in the upstream direction, and decreases the (absolute value of) velocity in the downstream direction. The density profile approaches an exponential in each direction, with the decay constant governed by the asymptotic value of velocity.

For analysis of experimental impurity density (emission) profiles, these fluid equations need be solved essentially in reverse. Values of background n, T, and v need be found to produce a profile most closely matching that of the experiment, hence leading to the extraction of these plasma parameters from the plumes. To make the extraction more manageable, the density is assumed to be specified. The density is chosen because of the three parameters, the impurity profile is least sensitive to the background density. While the impurity density profile varies a great deal with the background temperature, the variance with plasma density is much less pronounced (being off on density by 50% is far from catastrophic

for the solved impurity density profile shape whereas being off on temperature by that amount is). How a background density is chosen will be discussed in section 5.3 and in the next chapter.

5.1.2 Perpendicular Solution

For analyzing the perpendicular profile of the impurity ions, only the continuity equation (5.1) is employed. The impurity ion flux is posited to have a diffusive and a drift component, so that:

$$\Gamma_{\perp} = nv_{\perp} - D_{\perp}\frac{dn}{dz} \tag{5.14}$$

As will be discussed below, the drift component of flux is found to dominate the diffusive, so while this form of diffusion may be brought into question, any potential criticism is moot. The parallel impurity ion flux is taken to go to zero at positive and negative infinity along the field line, as was the poloidal flux in the perpendicular direction in the equations discussed in the last section. Hence, inserting equation 5.14 into the continuity equation, and integrating along the field line so that the x dependent terms drop out, one arrives at the one-dimensional perpendicular equation for the impurity ions:

$$-D\frac{d^2n}{dz^2} + v\frac{dn}{dz} + n_e < \sigma v >_i n = S_o e^{-(z/\lambda)^2} \tag{5.15}$$

where the perpendicular subscripts have been dropped, and the gaussian form of the source function inserted. For a FWHM of 3.5 cm, $\lambda = 2$ cm. Because the diffusion coefficient and drift velocity are posited as specified and constant, density is the only variable to be solved for in equation 5.15. Momentum and energy equations are unnecessary.

Equation 5.15 has the virtue of having an analytic solution. Upon integration, with D, v, S_o, and the ionization rate constant, the solution for the impurity density profile is found:

$$n = \frac{\lambda \sqrt{\pi} S_o}{2(\alpha_1 - \alpha_2)D} [e^{\alpha_1 z} e^{(\lambda \alpha_1/2)^2} (1 - \text{erf}(\frac{z}{\lambda} + \frac{\lambda \alpha_1}{2})) +$$

$$e^{\alpha_2 z} e^{(\lambda \alpha_2/2)^2} (1 + \text{erf}(\frac{z}{\lambda} + \frac{\lambda \alpha_2}{2}))] \qquad (5.16)$$

for which the constants of integration are:

$$\alpha_1 = \frac{v}{2D} + [(\frac{v}{2D})^2 + \frac{n_e <\sigma v>_i}{D}]^{1/2} \qquad (5.17)$$

$$\alpha_2 = \frac{v}{2D} - [(\frac{v}{2D})^2 + \frac{n_e <\sigma v>_i}{D}]^{1/2} \qquad (5.18)$$

Since only the form of the density profile is sought (and since the absolute value of the source function is not known), the front factors of equation 5.16 can be ignored. Given the values of electron density, the ionization rate coefficient, the drift velocity, and the diffusion coefficient, the impurity ion density is a straightforward function of z.

Figure 5.4 gives representative plots for the density (n) profile, as defined by equation 5.16, for cases of $5 \times 10^{19}/m^3$ and 12 eV background density and temperature, a diffusion coefficient of .5 m^2 /sec, and drift velocities of 0, 1000, and 5000 m/sec. The case of no drift is symmetric. The asymmetry and width of the profile expands with increasing velocity. The profile shape is determined by the values of plasma density and temperature and the drift velocity. While the diffusion coefficient theoretically plays a role, in practice it is insignificant. To see why, one need only compare the characteristic diffusion length, $(D/n_e <\sigma v>_i)^{1/2}$, with the λ (2 cm) of the source. With typical values, the diffusion length is on the order of 1 mm; no reasonable value of D will make much of a difference in the perpendicular profile. For the benchmarking in section 3, D is set to the

Figure 5.4: Poloidal C-II Density Profiles for Background $5 \times 10^{19}/m^3$ and 12 eV, D of .5 m^2/sec
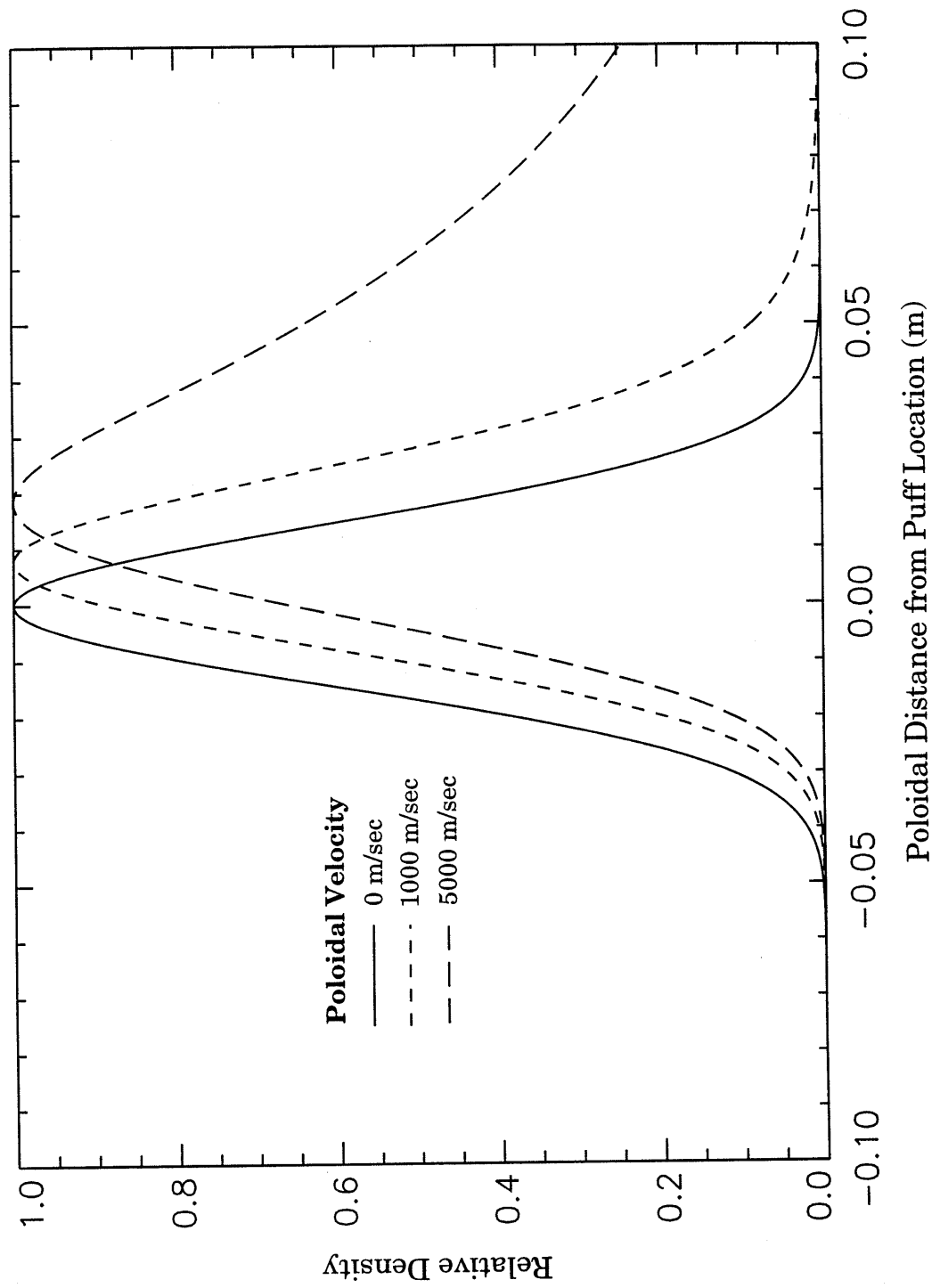
same value used by DIVIMP, while in the experimental analysis in the next chapter, a value of .1 is used.

For a given plume, the task of unfolding the parameters (impurity density, Deuterium parallel velocity, and the perpendicular drift velocity) with the fluid model is now straightforward. A background plasma density is first chosen. The parallel equation discussed in the last section is then utilized to find the background temperature and velocity. With this temperature and the chosen density, the poloidal drift velocity is determined with the perpendicular equation. Two facts should be reiterated. First, while the parallel velocity found by the fluid solution is that of the background deuterium ions, the perpendicular drift velocity derived is the drift velocity of impurity ions in question, not that of the Deuterium ions (if the cause of the drift is known, whether ExB or otherwise, the Deuterium drift velocity can then be inferred). Secondly, the parameters found are not those for a particular flux surface, but rather a radially integrated average.

5.2 Divertor Impurities Code (DIVIMP)[4]

DIVIMP is a Monte Carlo code used to describe the transport of impurity ions in a tokamak plasma. With a given background plasma and geometry, it tracks individually launched impurity ions or neutrals, following the impurity through successive ionization levels until the

---

[4]Information for this section was obtained from:

 J.D. Elder and P.C. Stangeby, "The DIVIMP User Manual", University of Toronto IAS, 1995.

 S. Lisgo, private communications, Dec 1995 - April 1996.

 P.C. Stangeby and J.D. Elder, "Calculation of Observable Quantities using a Divertor Interpretive Code, DIVIMP", Journal of Nuclear Materials, 196-198(1992), pp. 258-63.

 P.C. Stangeby and J.D. Elder, "A Guide to the DIVIMP Code", University of Toronto IAS, 1995.

particle leaves the edge, either by making entry into the plasma core or by deposition on a solid surface. For ionization, charge exchange, and other atomic processes, the ADAS coefficients are employed.[5] Motion parallel to the magnetic field is taken to be governed by classical coulomb collisions and cross-field motion is described by anomalous diffusion coefficients and drift velocities. Surface interactions can also be followed (sputtering, etc).

For impurity plume modeling, a much scaled down version of DIVIMP is employed (basically a scaled down version of Limiter Impurities/LIM,[6] DIVIMP's predecessor). A simplified 1-D or 3-D slab geometry is used and it is assumed that the background plasma parameters are solely a function of radius (r). Impurity ions are launched from the injection location (inner-wall midplane) and followed until they reach the central plasma, become embedded in the wall, or reach an ionization state which is not of interest. For given values of the background plasma, the shape of the plume in 3-D can be produced for whichever ionization states are desired. These 3-D plumes can then be integrated radially to obtain the 2-D view equivalent to that observed by the Culham camera, and further integrated to obtain parallel and perpendicular profiles. For this experimental program, the primary use of DIVIMP is as a benchmark on the solutions to the fluid model described in the last chapter. Further work on the tracking of injected impurities in the complex geometry of Alcator C-Mod, to calculate fueling efficiency properties and the like, is being performed, but will not be discussed in this thesis.

---

[5] H.P. Summers, "Atomic Data and Analysis Structure (ADAS)", JET, 1994.
[6] P.C. Stangeby, et al, "Monte Carlo Modeling of Impurity Ion Transport for a Limiter Source/Sink", Nuclear Fusion, 28(1988), pp. 1945-62.

For the scaled down DIVIMP code used for plume analysis, besides the inherent Monte Carlo and three-dimensional aspects of the model, the code follows the impurities in a way similar to the fluid model described in the last section. The time an impurity ion spends in each charge state is determined by:

$$t = \frac{-\ln(\xi)}{n_e < \sigma v >_i} \tag{5.19}$$

where ξ is a random number between 0 and 1. Transport of the neutrals is followed simply by extrapolating their trajectory until ionization (interactions such as charge exchange are ignored). Parallel transport of the ions is followed via velocity diffusion, with the change in the velocity at each time step governed by:

$$\Delta v = < \Delta w > \Delta t + (< \Delta w^2 > \Delta t)^{1/2} \xi_g \tag{5.20}$$

where $<\Delta w>$ and $<\Delta w^2>$ are Spitzer collision coefficients and ξ_g is a random number with a gaussian distribution about zero. Essentially, $<\Delta w>$ represents the frictional force term (equivalent to the first term on the RHS of equation 5.8), and $<\Delta w^2>$ the pressure gradient term (equivalent to the second term on the LHS of equation 5.8). A Spitzer relation comes into play with the pressure gradient term since the change in temperature of the impurity ions along the field line will be governed by their equilibration with the background plasma ions (a phenomenon introduced in the fluid model by the first term on the RHS of equation 5.9). As was done with the parallel fluid equations, the electric field force and other momentum source terms are folded into the background ion velocity in the manner described by equation 5.6. For definitions and full discussions of these Spitzer coefficients, the reader is referred to chapter 5 of "A Guide to the DIVIMP Code", referenced above.

Perpendicular transport is followed via anomalous diffusion plus drift; for each time step:[7]

$$\Delta z = \pm(2D_\perp \Delta t)^{1/2} + v_\perp \Delta t \qquad\qquad (5.21)$$

The sign of the first term on the RHS of equation 5.21 has equal probability of being positive or negative. The diffusion coefficient and drift velocity of the equation need to be specified. For perpendicular transport radially, the same form is used (with the drift velocity set to zero). The time steps are set to be much smaller than any of the relevant processes. Though superficially different from a fluid analysis, the approach turns out to be largely equivalent (though of course allowing for much easier analysis in multi-dimensions). It need be stressed that DIVIMP is not a kinetic model, but rather, at root, it is a three dimensional Monte Carlo 'fluid model'.

5.3 Benchmarking[8]

DIVIMP has been utilized as a cross-check on results produced by the fluid model. This benchmarking has had two phases: the first involved using DIVIMP in a 1-D configuration to reproduce the fluid results (as a very basic cross-check); the second involved producing full 3-D plumes with DIVIMP to check that the temperature and velocities found with the fluid model have a basis in reality. Since the two model paradigms are largely equivalent, the cross-check is not a validation of assumptions. Checking against DIVIMP does not certify the efficacy of the fluid approach. It is, however, a check against a model with a proven track record, and one which does account for phenomena which the fluid model cannot (the three

---

[7]It may not seem obvious that the factor of two under the root should be there. It appears upon the proper treatment of diffusion as a random walk process, ref: P.G. Shewmon, Diffusion in Solids. New York: McGraw-Hill Book Company, 1963, section 2.3.

[8]DIVIMP calculations discussed in this thesis were performed by S. Lisgo, Dec 1995-April 1996.

dimensional nature of the transport of the injected impurity and partial collisionality).

The 1-D comparison involved following only parallel transport with DIVIMP, launching C-II ions from a gaussian profile, such as is done with the fluid code. Three of the cases performed, with various background temperatures, densities, and velocities, are shown in figure 5.5. The same parameters were given to both models, and, as is shown in the figure, the match between the two was very good. As discussed in the last section, this agreement is not surprising. Compressed to one-dimension, DIVIMP has what are more or less equivalent terms governing its following of the impurity ion transport to those terms governing the impurity fluid in equations 5.7-9.

Figures 5.6-5.12 detail two benchmarking cases involving the use of DIVIMP with its full 3-D capabilities. For both cases, DIVIMP is given radial profiles for plasma density and temperature, then allowed to construct a full 3-D C-II ion plume. These plumes are then integrated radially to give a 2-D plume contour (equivalent to the experimentally seen plumes shown in figures 4.1, 4.2, and 4.4; note that the DIVIMP plumes which are plotted below do not have that same tilt as the experimental ones, since the field line angle is not accounted for). In turn, these contours are integrated poloidally and toroidally to yield parallel and perpendicular profiles for analysis by the fluid model. The purpose of running these cases is to use DIVIMP to imitate the experimental situation, namely the situation in which the plumes observed result from radial integration over the impurity ion density/emission.

For the first case (labeled case A in the figures), flat radial plasma profiles are employed: a temperature of 12 eV, density of $1 \times 10^{19}/m^3$,

Figure 5.5: 1-D Comparisons of DIVIMP and Fluid Model

Background
$5 \times 10^{19} \mathrm{m}^{-3}$
10 eV
2736 m/sec

—— Fluid Model
– – – DIVIMP

Background
$5 \times 10^{19} \mathrm{m}^{-3}$
18 eV
13000 m/sec

Background
$1 \times 10^{19} \mathrm{m}^{-3}$
12 eV
13000 m/sec

Distance from Puff Location (m)
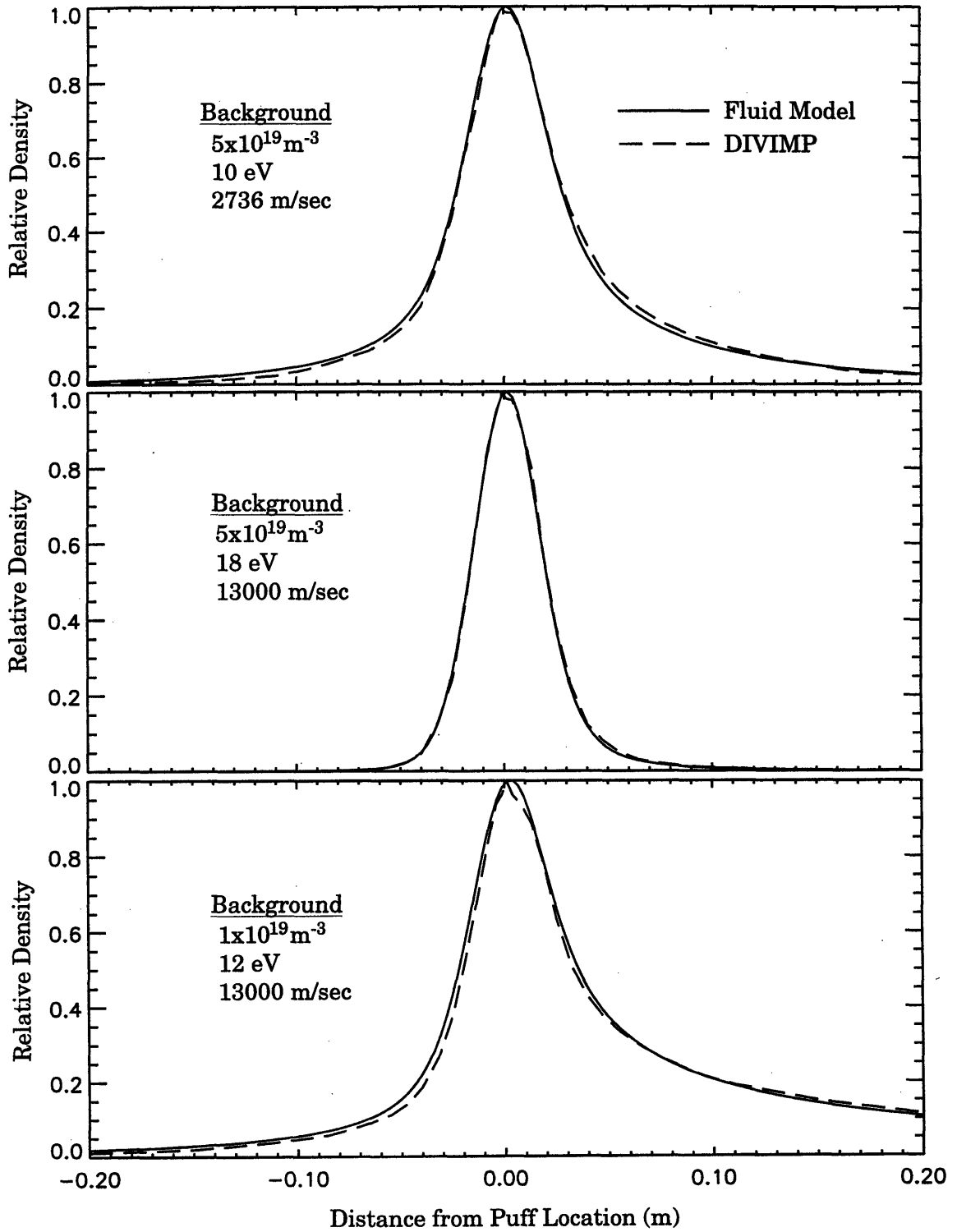
parallel velocity of 13000 m/sec, radial and poloidal diffusion coefficients of 1.0 m²/sec, and a poloidal drift velocity of 1500 m/sec. The two-dimensional plume that results upon radial integration is shown in figure 5.6. In figures 5.7 and 5.8, the perpendicular and parallel density profiles that result upon integrations of the DIVIMP plume are compared with the respective results of the fluid model using the same plasma parameters. The match is not perfect, but it is close. By close, it is meant that to get a best fit one need only slightly alter the parameters given to the fluid model (increase parallel velocity to about 13300, and increase perpendicular velocity to about 1550). For DIVIMP, the only additional physics compared with the one-dimensional case is the inclusion of radial diffusion (no pinch velocity is posited). For these simple flat plasma profiles, while the effect of radial transport is noticeable, it is small.

For the second 3-D case (case B), more physical plasma density and temperature profiles are used, while the same velocities and diffusion coefficients are employed as in case A. The profiles, as well as the resultant radial profile for the C-II ions is given in figure 5.9. The calculated 2-D plume is given in figure 5.10. (The radial C-II profile was found by integrating the plume toroidally and poloidally.) As in case A, the 2-D plume is integrated to give the parallel and perpendicular profiles. This brings up the issue of the interpretation of the plume profile shapes. The impurity density profiles are not on single flux surfaces at uniform density and temperature, but rather are integrations over radial distributions. Indeed, the primary reason for doing this DIVIMP comparison is to test if the radial averages found with the fluid model appear to be meaningful.

Figure 5.6: DIVIMP Case A Plume

Background Plasma Radially Uniform, 12 eV, $1 \times 10^{19} m^{-3}$, D of 1.0 m^2/sec, 13000 m/sec par v, 1500 m/sec perp v
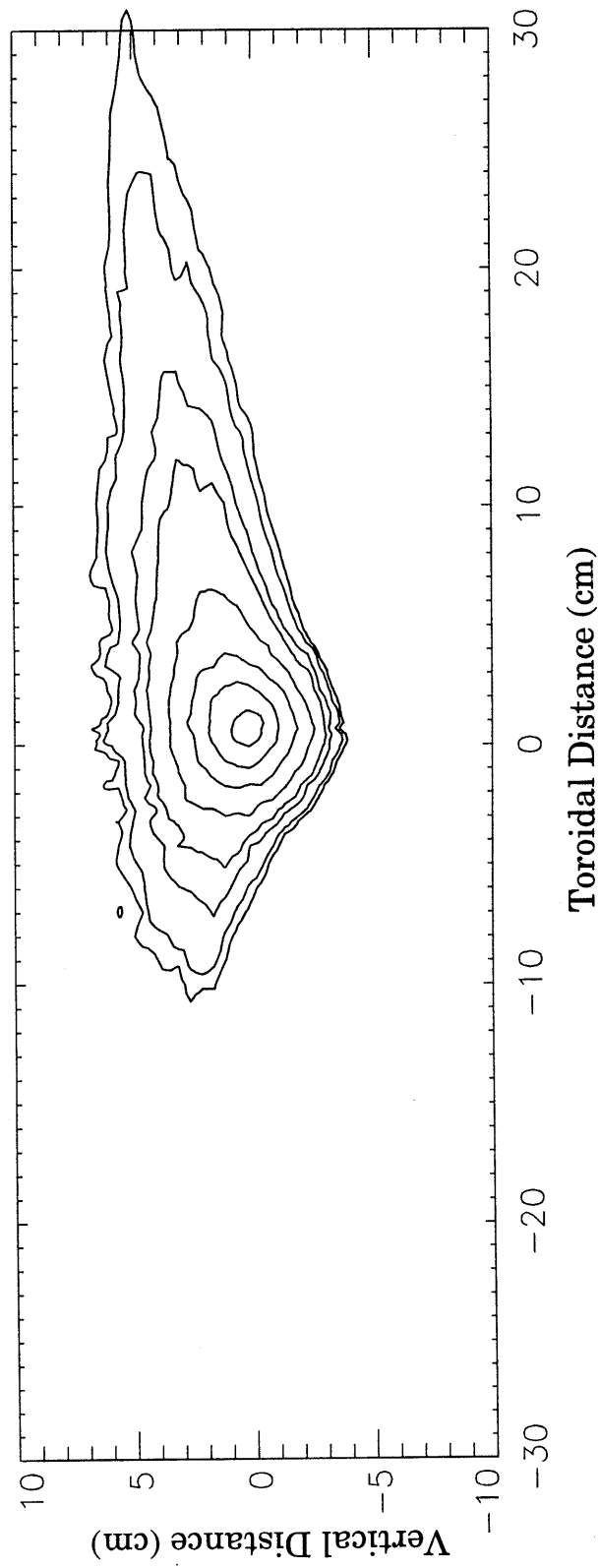
Figure 5.7: Parallel Profile Match to DIVIMP Case A

Fluid Model
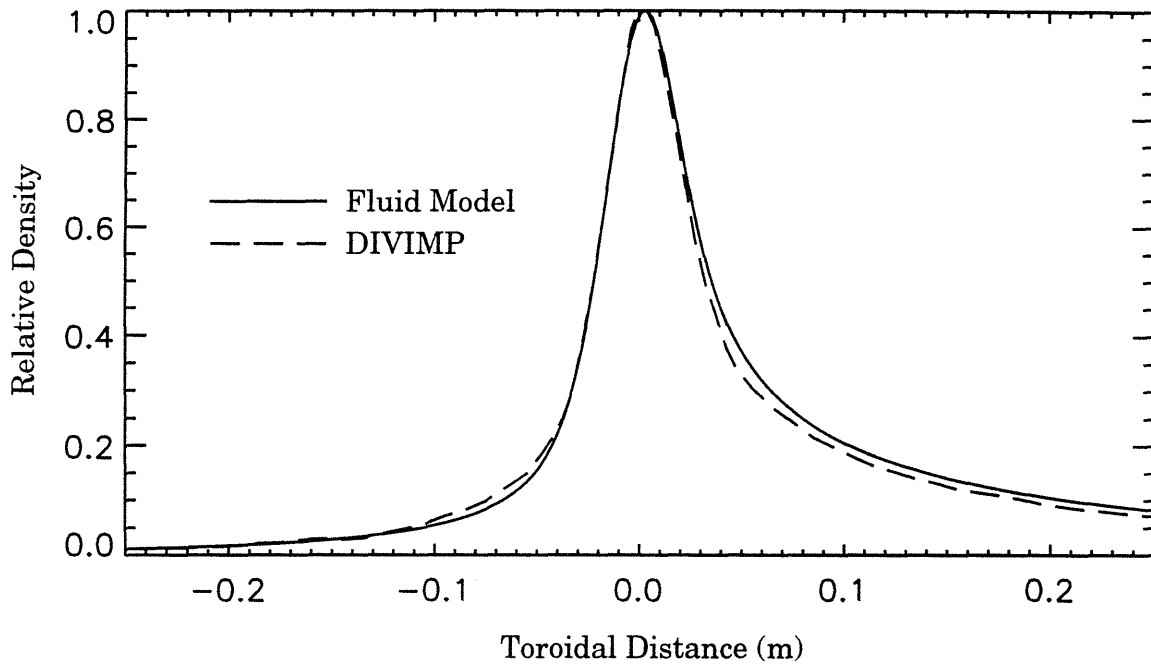
DIVIMP

Figure 5.8: Perpendicular Profile Match to DIVIMP Case A

Fluid Model
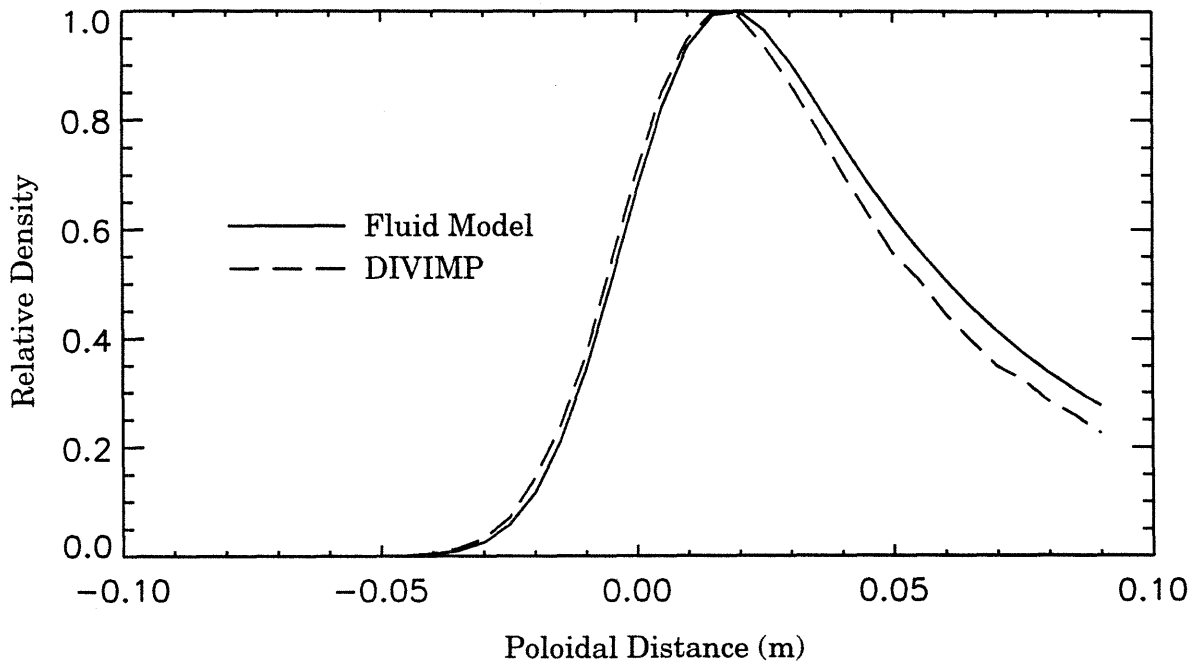
DIVIMP

Figure 5.9: Radial Plasma Profiles for DIVIMP Case B
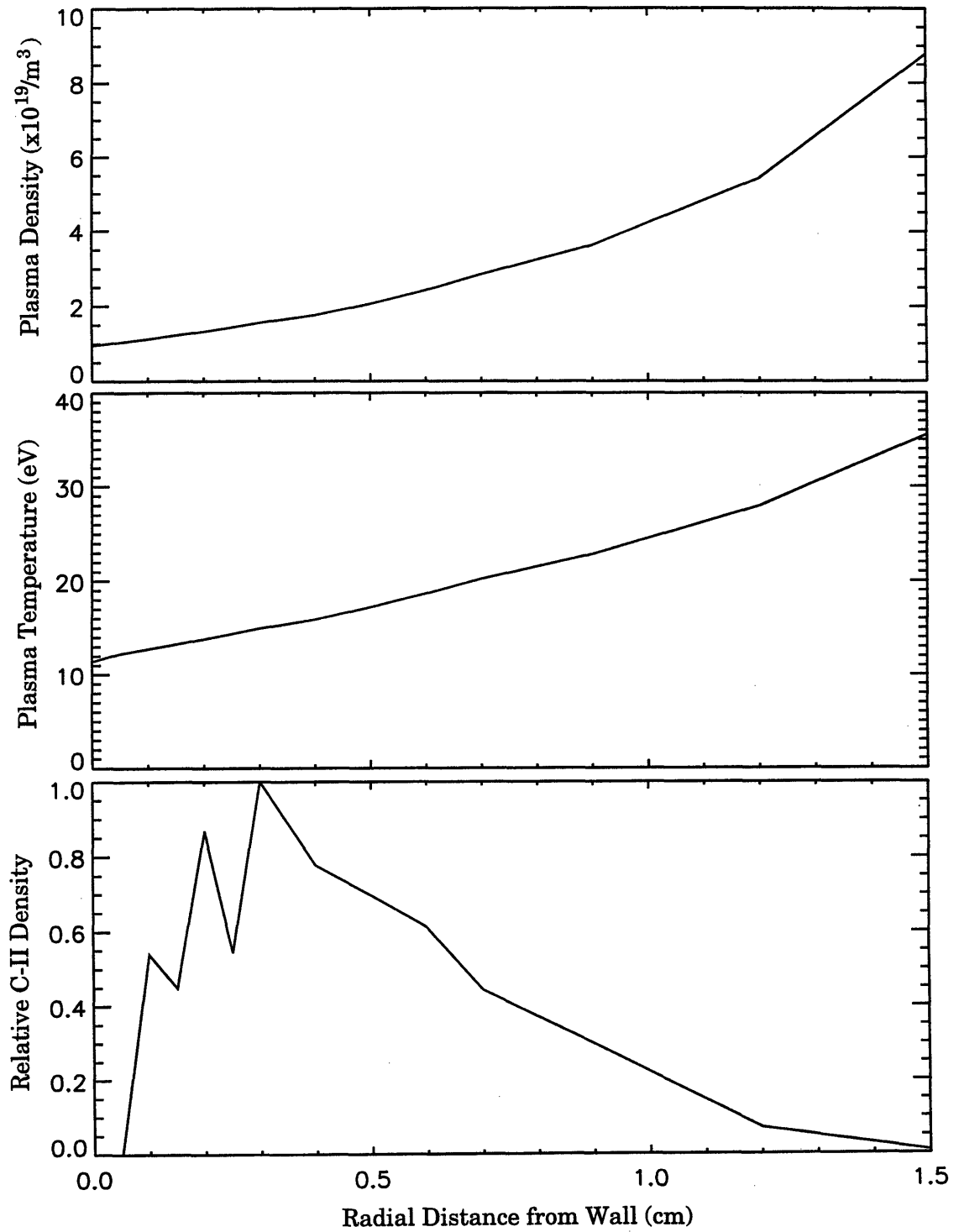
Figure 5.10: DIVIMP Case B Plume

Background Plasma Profiles given in Figure 5.9, D of 1.0 m^2/sec, 13000 m/sec par v, 1500 m/sec perp v
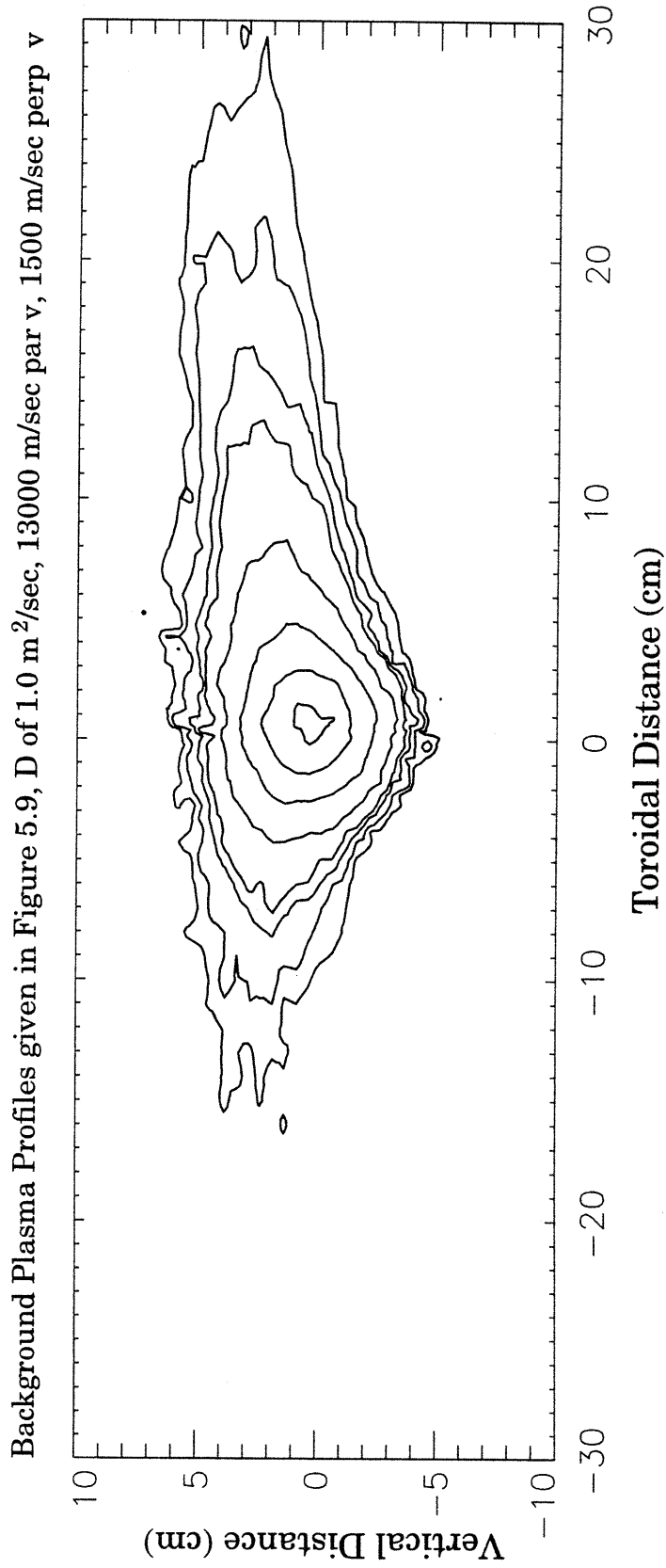
For matching the profiles, a plasma density needs to be used. Looking at the radial C-II profile, a representative (or 'average') radial position is chosen, about .55 cm, for which the plasma density is about $2.3 \times 10^{19}/m^3$ (the fluid model results will not be greatly effected by using a slightly different 'average' radial value). With that density, the best fits to the parallel and perpendicular profiles are given in figures 5.11 and 5.12. The temperature found by the fluid model, 16.2 eV, seems reasonable, it being the value of the background plasma at about r=.5 cm. A parallel velocity of 12400 was matched, rather close to the 13000 m/sec used by DIVIMP. The perpendicular velocity found by the fluid model was a bit further off, 1800 m/sec versus the 1500 m/sec DIVIMP modeled.

With DIVIMP, two effects are seen from the radial nature of the impurity plumes which are not accounted for by the fluid model. The two are radial transport and the non-uniform (radially dependent) plasma parameters. While these effects do cause alteration in the plume shape, they do not seem to be deleterious to the use of the two dimensional fluid paradigm to extract useful information (in fact the radial diffusion coefficient of 1.0 m^2/sec used above is likely a factor of 2 or so higher than the actual value). As long as a reasonable electron density is chosen for input to the model, it appears that the calculated temperature and velocities will be reasonable as well.

Figure 5.11: Parallel Profile Match to DIVIMP Case B

Fluid Model
$2.3 \times 10^{19}/m^3$
16.2 eV
12400 m/sec
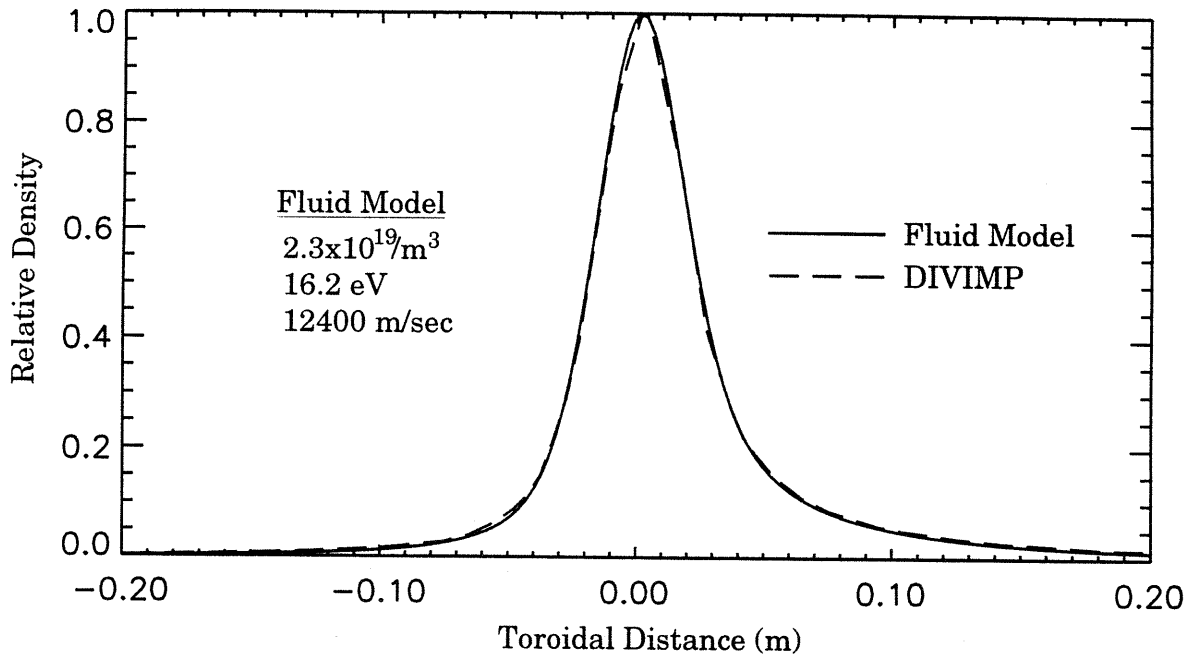
Fluid Model
DIVIMP

Figure 5.12: Perpendicular Profile Match to DIVIMP Case B

Fluid Model
$2.3 \times 10^{19}/m^3$
16.2 eV
1.0 m^2/sec
1800 m/sec
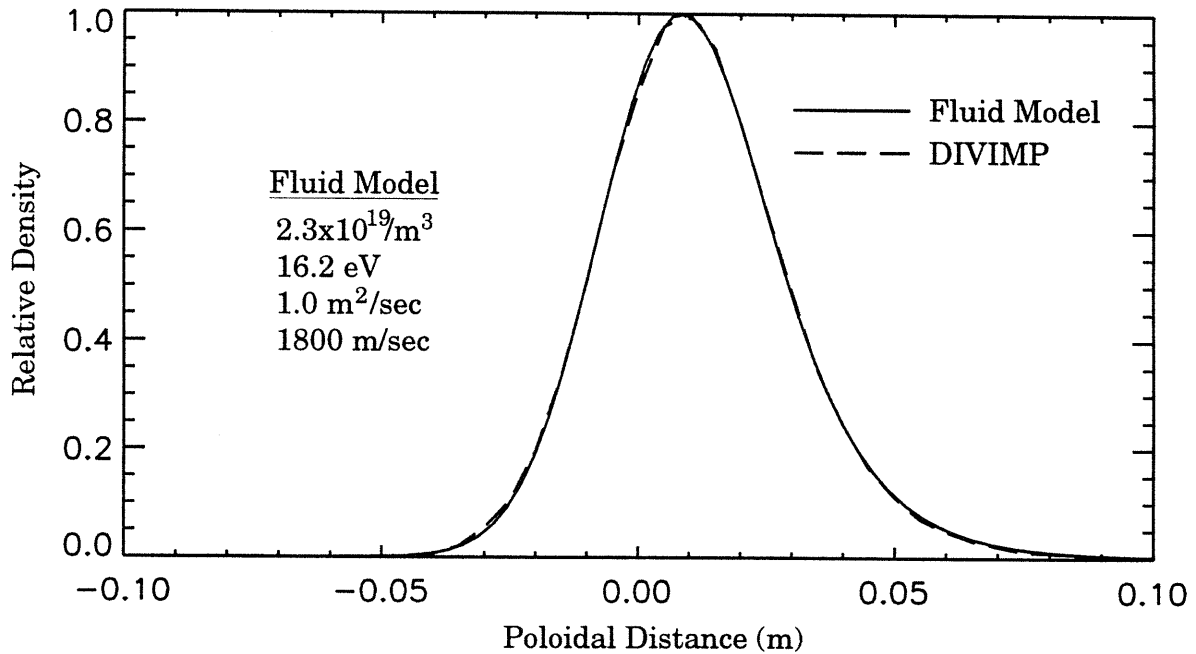
Fluid Model
DIVIMP

Chapter 6
Analysis

The fluid model described in the previous chapter has been applied to plumes produced at the inner-wall midplane (location A in figure 3.1) in three C-Mod runs (950414, 950526, and 951219; plumes observed in run 960208 will be briefly discussed, but have not been modeled). This chapter presents the results of that analysis. In the first section, the method of extracting quantitative information from the plume shapes is outlined, using shot 951219011 as a representative example. Section two presents a summary of the information obtained from applying the fluid analysis to 17 shots. The third section compares the results from run 951219 with scanning probe measurements.

As touched upon briefly in section 1.4, the observation and modeling of plumes produced in the region of an impurity puff is not unique. Though in less extensive experimental programs than that of C-Mod, such work has been performed on DITE, TEXTOR, and DIII-D, for example. The uniqueness of the plume program at C-Mod comes in the use of modeling of the impurity emission patterns to not only test and enhance the knowledge and assumptions of impurity transport, but to also extract knowledge about the background plasma from the plume shapes; i.e. to use plumes as a

scrape-off layer diagnostic. In previous experiments, two approaches have been taken to model these emission patterns: the use of a complex fluid[1] or Monte Carlo[2] code and the use of simple analytic (Spitzer type) relations.[3] The (quasi-) 2-D fluid model described in chapter 5 takes an intermediate approach, namely being more complete and accurate than using simple analytic relations, but still being simple and straightforward enough for ease in code implementation and in interpretation of calculations. It should be noted that, though not implemented experimentally, a somewhat different approach for using plumes as a diagnostic has been proposed and discussed by Stangeby. The approach would involve imaging multiple charge states simultaneously, extracting plasma parameters from the relative widths of the observed profiles.[4]

6.1 Parameter Extraction

As mentioned in chapter 5, a background electron density is required for application of the fluid model to an experimental plume. Scanning probe measurements are utilized in this role. The device provides the only

---

[1] For example: the Braams B2 fluid code was used to model plumes observed on DIII-D, ref:
G.F. Matthews, et al, "Impurity Transport at the DIII-D Divertor Strike Points",
Proceedings of the 18th European Conference on Controlled Fusion and Plasma Physics,
Volume 3, 1990, pp. 229-332. Reference for the Braams code: M.F.A. Harrison, et al
"Plasma Edge Physics for NET/INTOR", Report EUR-FU/XII-361/86/50, CEC, Brussels,
1986.
[2] For example: LIM (DIVIMP's predecessor) was used for plume modeling on DITE and
TEXTOR, refs:
   C.S. Pitcher, et al, "Carbon Impurity Transport around Limiters in the DITE
Tokamak", Journal of Nuclear Materials, 176-77(1990), pp. 191-6.
   G.M. McCracken, et al, "A Study of Impurity Transport in the Plasma Boundary of
TEXTOR using Gas Puffing", Journal of Nuclear Materials, 176-77(1990), pp. 191-6.
[3] For Example: the plumes observed on DITE were analyzed with simple analytic relations
as well, ref: C.S. Pitcher, "Tokamak Plasma Interaction with Limiters", Doctoral
Thesis, University of Toronto IAS, 1987, chapter 10.
[4] P.C. Stangeby and J.D. Elder, "Some Possibilities for Measuring Local Plasma
Parameters in the Edge Plasma by Impurity Injection", Plasma Phys Control Fusion,
33(1991), pp. 1435-52.

reliable measurement of electron density in the scrape-off layer. While one would not necessarily expect the density on a given flux surface to be constant over the poloidal distance between the two locations (the scanning probe is on the outboard of the machine while the recorded plumes are at the inner-wall), one does expect the pressure to be approximately constant (any momentum dissipation in the SOL being concentrated near the divertor plates). A test of the accuracy of the density used will be how well the temperature derived from the plume shapes matches that measured by the probe for the appropriate flux surface. If this agreement is relatively good, then the density used for the model can be considered accurate for the plume location as well. If it is not, then one can perform an iterative process until pressure agreement between the plume and scanning probe measurements is found.

Figure 6.1 diagrams the geometry of the situation. Scanning probe profile measurements are made above the x-point in the lower half of the machine. These measurements are then mapped along the flux surfaces (as calculated by EFIT from magnetic measurements) to be found as a function of ρ, the distance of the respective flux surface from the LCFS at the outboard midplane. The profiles can also be mapped to the inboard to find the measurements as a function or r, the distance of the appropriate flux surface from the inner-wall at the midplane. Figure 6.2 shows such mappings, for shot 951219011, 730 msec into the discharge. The profiles of both density and temperature with ρ and r are plotted. For this particular shot, the scanning probe did not scan all the way to the LCFS, which is why the profiles abruptly end before reaching that point. Each of the profiles contains six points, with the uncertainty in each density and temperature value in the range of 10-20%.
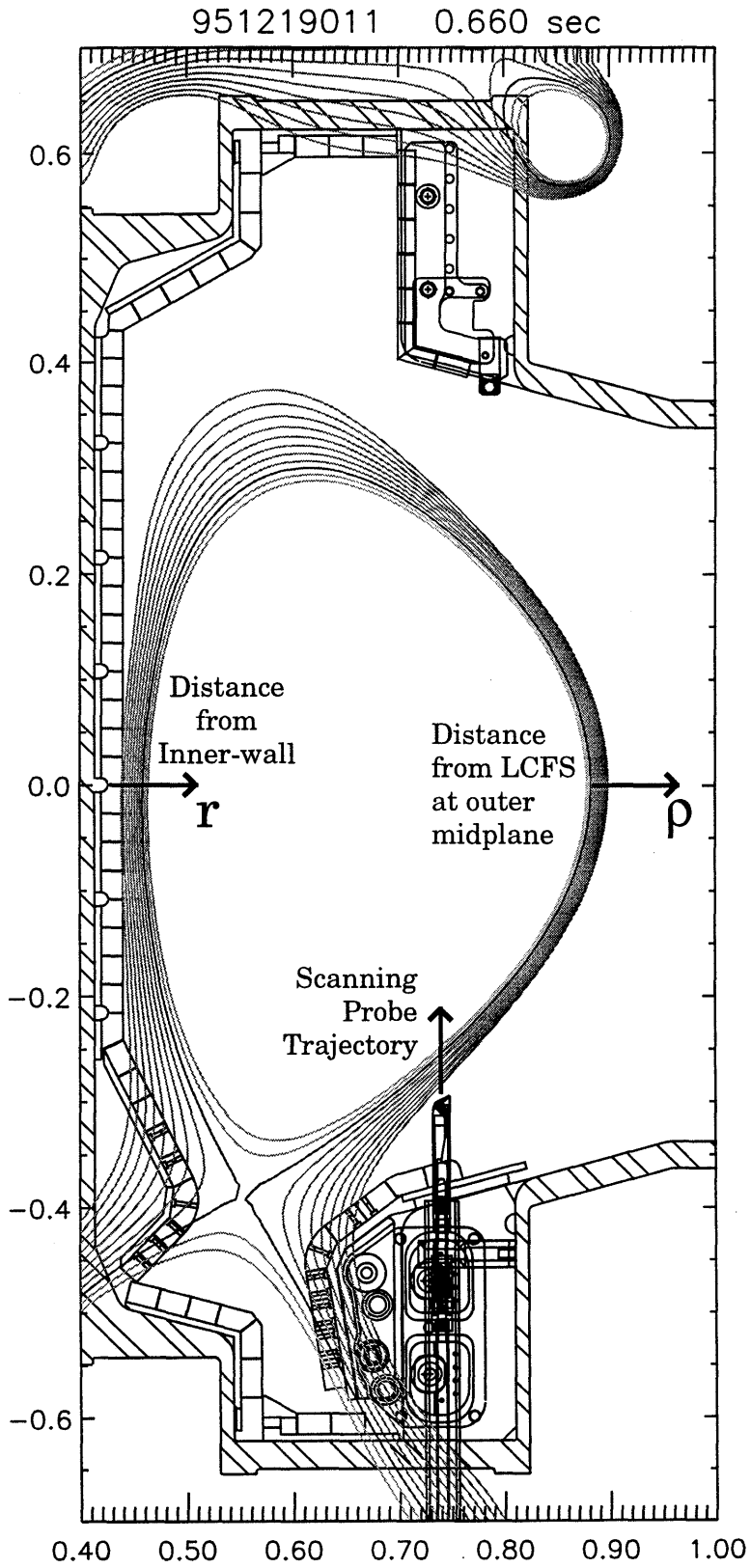
951219011   0.660 sec

Distance from Inner-wall → r

Distance from LCFS at outer midplane → ρ

Scanning Probe Trajectory

Figure 6.1: Mapping of Scanning Probe to ρ and r along Flux Surfaces

(Distances in meters)

The question is still begged of which density value along the profile to use in the fluid calculations. Using the right hand side profiles of figure 6.2, the radial ionization profiles at the inner-wall for a hypothetical neutral puff can be calculated with equation 3.2. This is done for methane, Nitrogen, and Helium (the puff for this particular discharge was of Nitrogen), and plotted in figure 6.3 (for the calculation, smooth spline fits are made through the density and temperature profiles). Methane and Nitrogen ionize close to the wall, with the peak actually occurring at the wall. Because this is the case, both in this shot and in all the discharges analyzed, and because the scanning probe measured profile of density tends to be relatively flat in this region, it is deemed satisfactory to use the value of density at the flux surface of r=0 (at the wall). For Helium, the situation is more ambiguous. A representative location along the ionization profile needs to be chosen. For the two Helium injection discharges analyzed in the next section, the rough midpoint (r of 9 mm) is used. This choice of this representative location seems to be as good as any, and it does appear to produce satisfactory results. Deeming a somewhat different value of r to be a better average will make little difference in the fluid model result. For example, between 0 and 12 mm in the profiles of figure 6.2, density varies from about 6 to 7×10^{19} m^{-3}. This difference would have essentially no impact on the calculations of the fluid model (more on the impact of density uncertainty below). This comes about because the shape of the parallel solution is determined by the relative sizes of the Spitzer equilibration rates and the ionization rate, as discussed in chapter 5. Since both of these are proportional to density, as the density increases, both of these rates increase in tandem. The impurity ions ionize to the next charge state faster, but they equilibrate faster with the background temperature and velocity as well (the

Figure 6.2: Scanning Probe Measurements Mapped to Outer and Inner Midplane for Shot 951219011
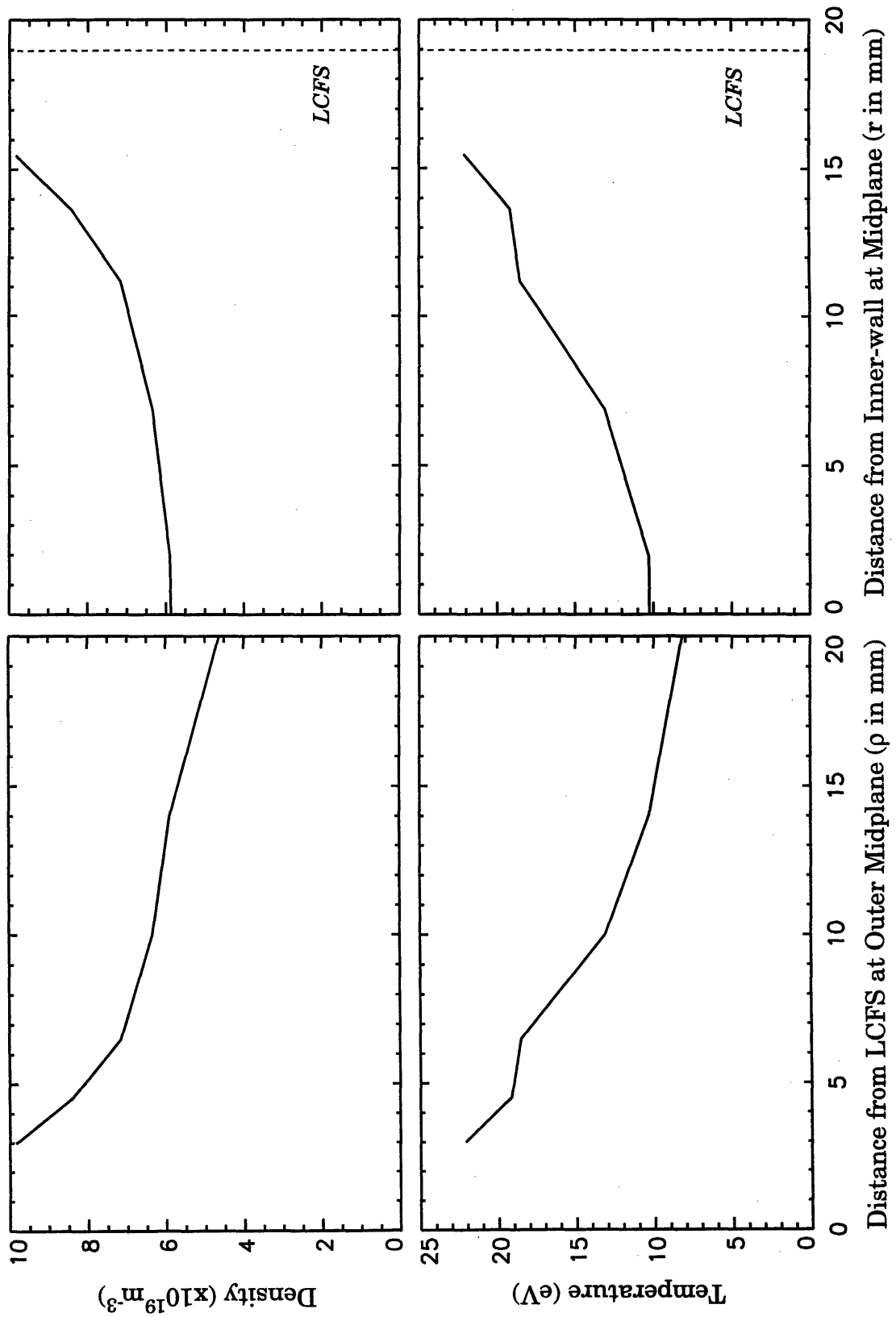
Figure 6.3: Radial Ionization Profiles for 951219011
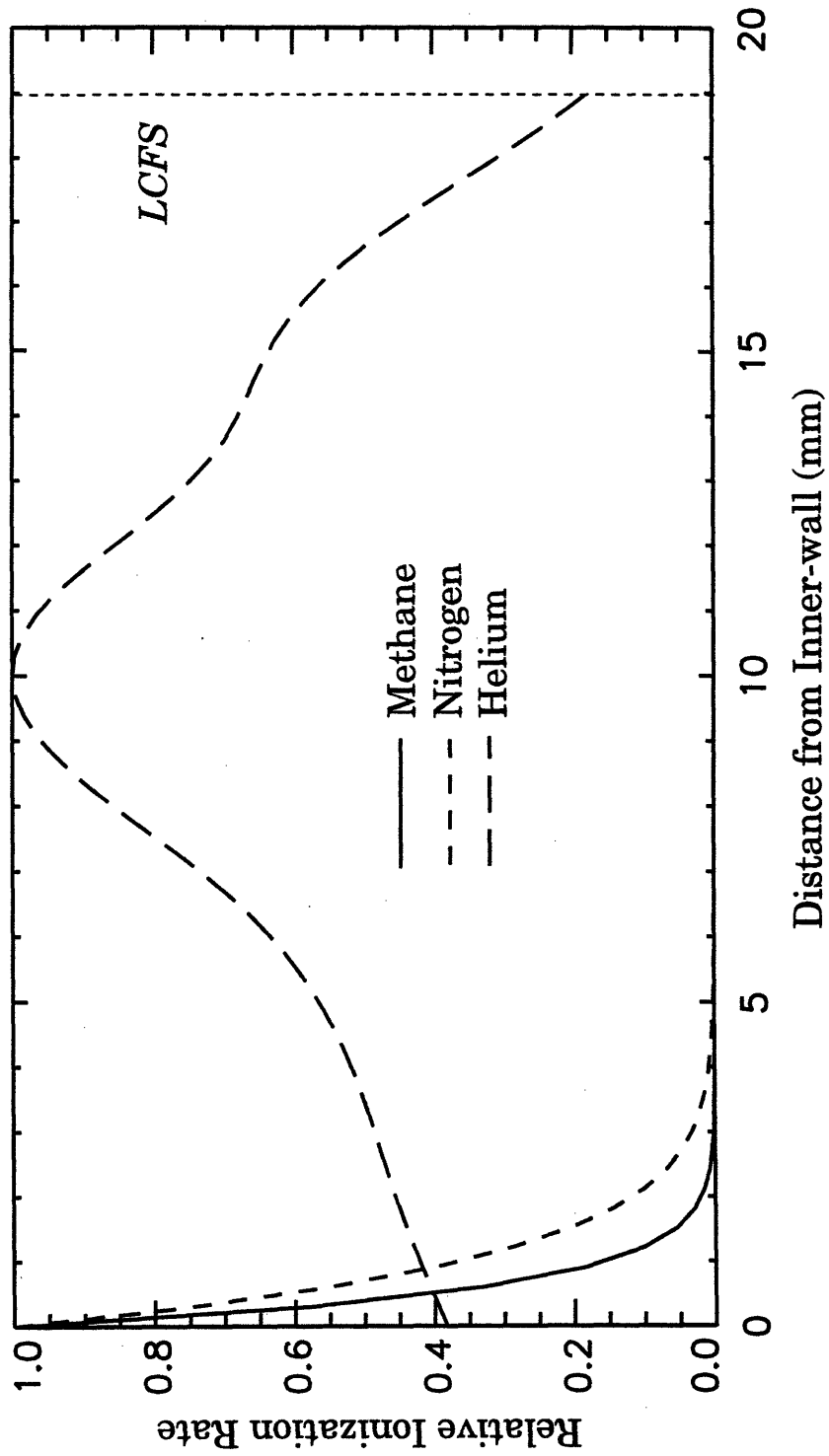
trade-off is not exact, of course, which is why electron density dependence of some degree is observed).

One problem that has been encountered in analyzing the shots from two of the three run days (950414 and 950526) is the existence of a secondary x-point relatively close to the LCFS. In figure 6.4, two magnetic equilibriums are shown, one with such a problem, and one without. In the equilibrium of 951219004, the field lines are seen to be contiguous around the plasma. All field lines in the region between the inner-wall and the LCFS have their strike points on the inner and outer divertor plates (one at each). In the other, that for 950415015, this is not the case. The secondary x-point (for this lower diverted shot, the one on the top of the machine) maps to about 7 mm out from the inner-wall midplane (IWM). This means that in the region immediately in front of the IWM puffing location, the scrape-off layer is effectively double nulled, with two strike-points on the tokamak inboard. Further, this means that these flux surfaces have no communication with those on the outboard of the machine, specifically to those of the scanning probe. While all the implications of this are not clear, one is: the density measurements mapped to this region from the scanning probe are invalid. Undoubtedly, with two strike-points so close, the region is colder than it would be otherwise. If it is cold enough, injected impurity gases may penetrate through it, ionizing in the single-nulled region. While the fluid characterization is as valid for these shots as for those in which a second separatrix is not a factor, there is the problem of having to select a density without a valid measurement. For these shots, the mapped scanning probe density is still used (for lack of a better estimate). Because of this, the solutions are not considered as accurate as those for shots without a second x-point problem. While the relative insensitivity of the

Figure 6.4:
Two C-Mod Equilibriums

Equilibrium on right shows
the secondary separatrix
lying between the LCFS and
the inner-wall (dashed line)

Distances are in meters
Shot number and time indicated
on top of each figure
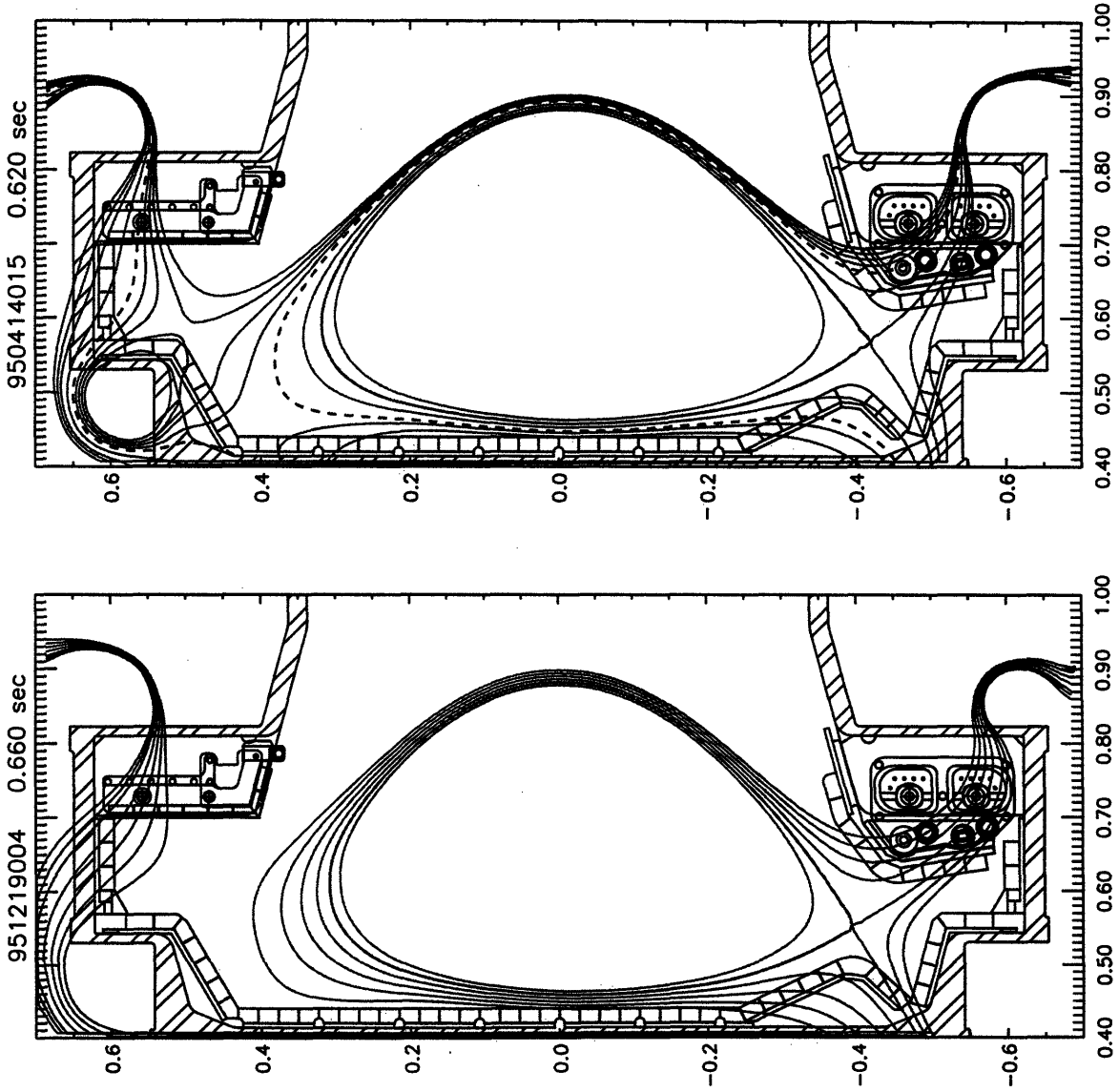
solutions to the electron density ameliorates the error, it cannot eliminate it. If, for example, a density of $1 \times 10^{19} m^{-3}$ is used when the actual density is more like $1 \times 10^{20} m^{-3}$, the fluid solution will be nonsense. Unfortunately, it is not known how far these densities can be considered in error. The problem was identified before run 951219, so that the six plumes analyzed in that run are not plagued with it. For this reason, the analysis in the next two section will focus on those discharges.

A contour plot of a two-dimensional N-II plume recorded during Nitrogen injection at the inner-wall midplane is given in figure 6.5. The image is corrected for the flux surface curvature about the inner-wall (the correction is actually minor for distances less than 20 cm from the puff location). The shot in which the plume was recorded, 951219011, had a 800 kA plasma current and a 5.3 Tesla magnetic field on axis. At the inner-wall in this configuration, the magnetic field angle is about 8 degrees (from horizontal), as indicated on the figure. The plume extends along the field line towards the lower divertor of this lower x-point shot (the magnetic equilibrium of the discharge is given in figure 6.4). The plume is integrated across the field line for analysis with the parallel fluid equations and along the field for analysis by the perpendicular. For electron density, the scanning probe measurement of $5.6 \times 10^{19} m^{-3}$ at the IWM flux surface is used.

Best fluid model fits to the profiles are shown in figures 6.6 and 6.7. A background plasma density and Mach number of 10.2 eV and -.40 are identified with the parallel solution. A 365 m/sec poloidal impurity ion drift velocity is found with the perpendicular (as discussed in chapter 5, the perpendicular diffusion coefficient is set to .1 m^2/sec for all analyzed shots). The Mach number is reasonable, and the temperature does in fact closely

Figure 6.5: N-II Plume for Shot 951219011
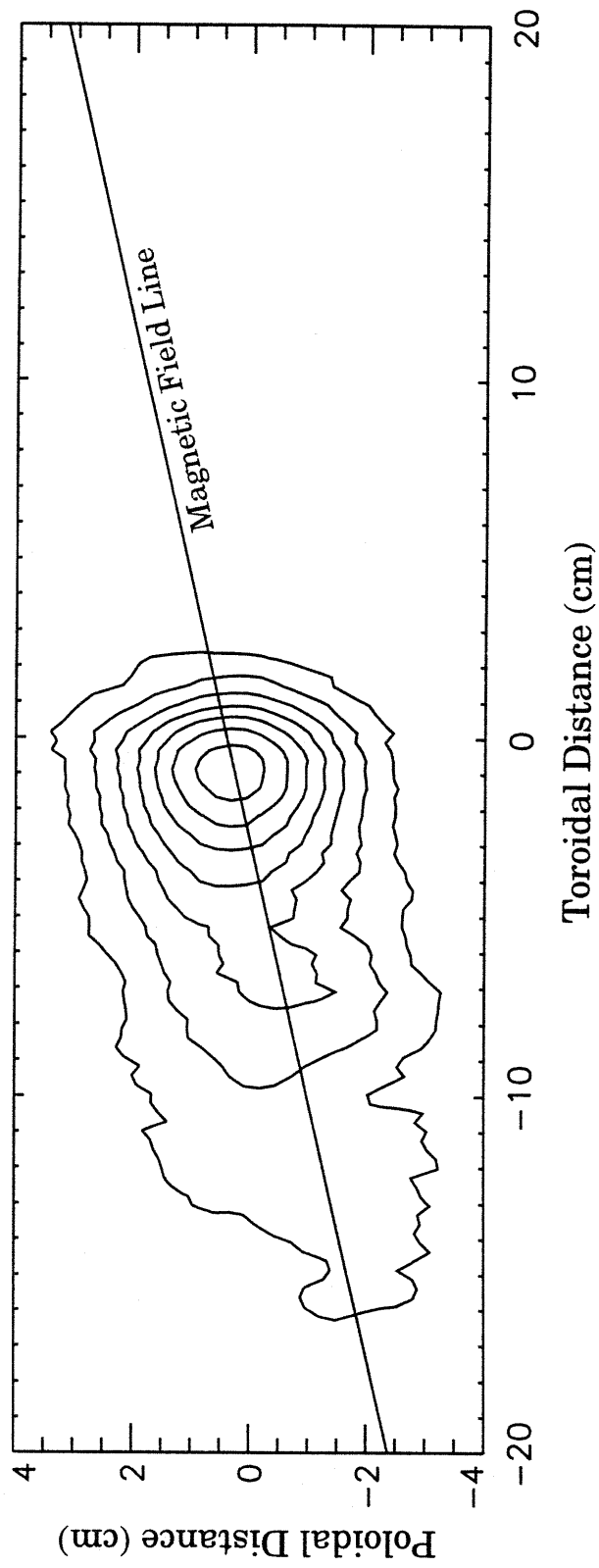
Figure 6.6: Parallel Fluid fit to Shot 951219011

$5.6 \times 10^{19}/m^3$
10.2 eV
Mach -.40

Relative Density

Distance along Field Line (m)
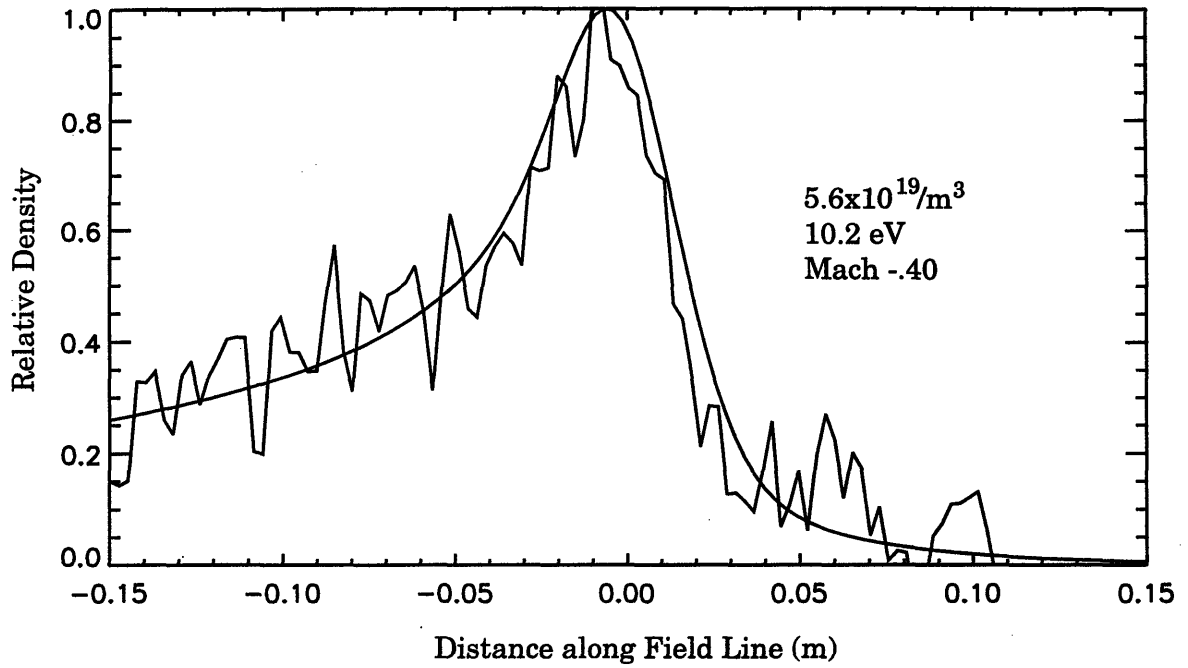
Figure 6.7: Perpendicular Fluid fit to Shot 951219011

$5.6 \times 10^{19}/m^3$
10.2 eV
365 m/sec

– – – Experiment
——— Fluid Model

Relative Density

Poloidal Distance (m)
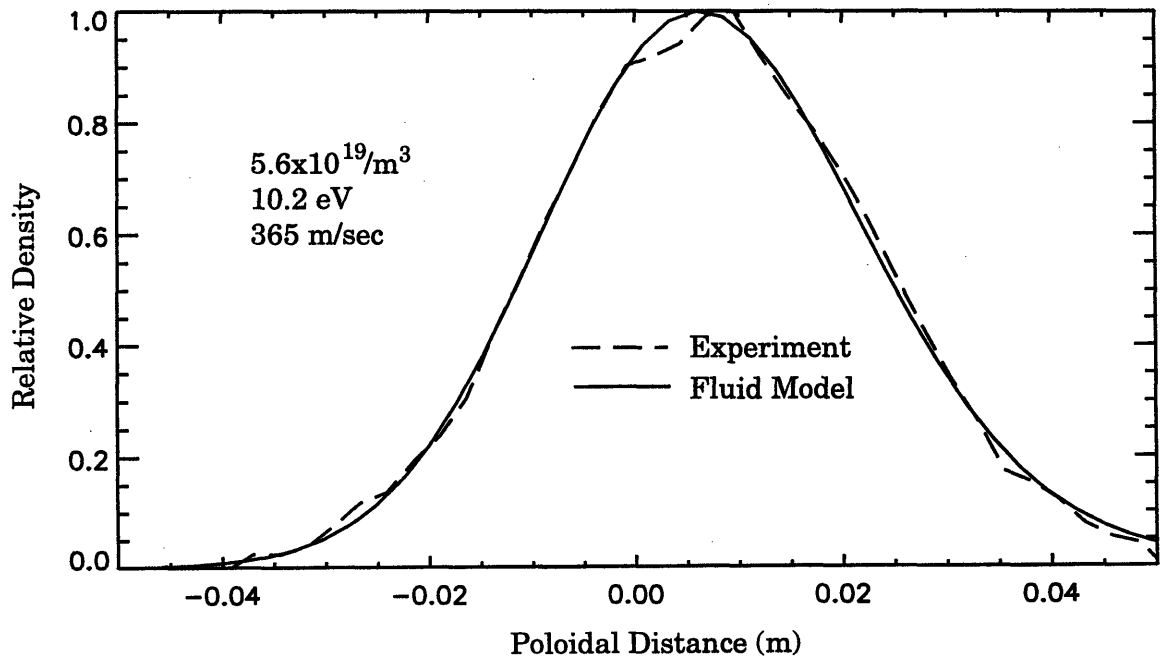
match that measured by the scanning probe for the flux surface (9.5 eV). Because of the implied conservation of pressure, this agreement in temperature validates the use of the scanning probe measured density. The Mach number at this temperature corresponds to a parallel Deuterium ion velocity of -12300 m/sec. If one takes the perpendicular drift velocity as entirely due to ExB drift (see section 1.3.2, specifically equations 1.15 and 1.18, and the discussion in the next section), since the magnetic field is about 8 Tesla at the inner-wall, a 2920 V/m radially outward (in minor radius) electric field is indicated. As will be detailed in section 3, this value is on the order of scanning probe measurements.

The sign convention is that in the parallel direction, a positive value denotes along the field line towards the upper part of the machine (right). A negative value is used for along the field towards the lower part of the machine (left). In the perpendicular (poloidal) direction, a positive value implies upwards, a negative downwards. Hence, for flow towards a lower strike-point, as in the above discussed case, the parallel velocity is negative. For the magnetic field in the clockwise (CW) direction, as is the case above, an ExB drift (for a radially outward electric field) would be upward, hence a positive ion drift velocity. If the direction of E or B is switched, a negative perpendicular velocity would be obtained.

A few words should be said about the uncertainties of the fits. The perpendicular profile fit in figure 6.6 is mathematically and aesthetically pleasing, that of figure 6.7 perhaps somewhat less so. The quality of these fits can be evaluated and error bars assigned to the found parameters (temperature, Mach number, and poloidal drift velocity). It is expected that the quality of the fit will not be the greatest source of uncertainty however. While the other sources of error are harder to quantify (in the case of the

effect of radial integration of the plumes, nearly impossible in a quantitative way), estimates of the associated uncertainties can be made. Such estimates for the fitted plume of shot 951219011 are listed in table 6.1. Four sources of error are considered: the statistical quality of the fit, the electron density employed in the fluid model, the uncertainty of the ionization rate coefficients used, and the angle of tilt of the camera imaging the plumes. Calculating the statistical uncertainty is a straightforward matter of finding how far from the fitted value the parameter in question would need to be to increase χ^2 by 1.0.[5] For temperature and drift velocity, the resultant error-bar is negligible, while for Mach number, it is significant (about 13%).

As stated above, the uncertainty of the scanning probe measured density is 10-20% (for the density at the scanning probe location). To check how density uncertainty affects the plume calculations, the density is decreased by a conservative 30% (to $3.9 \times 10^{19} \, m^{-3}$) and the fitting redone. The changes in each parameter that result is listed in the table. While the change in temperature and drift velocity are not insignificant, they are small (about 10%). The relatively small change in temperature is a product of the non-linearity the ionization rate coefficient shows with the temperature. A greater change in perpendicular velocity might be expected, but since the lower density induces a higher temperature for a proper fit (and hence a higher rate coefficient), the decrease in drift velocity is ameliorated. Note that this amelioration will only get one so far, if the density is instead off by a factor of 5, the error on this drift velocity will be much larger. For Mach number, a significant change is seen, to -.6, a

---

[5]P.R. Bevington and D.K. Robinson, <u>Data Reduction and Error Analysis for the Physical Sciences</u>, New York: McGraw-Hill, Inc, 1992.

Table 6.1: Potential Sources of Error for 951219011 Model Fit

Parameter	Fit	Statistical (χ^2 inc by 1)	SP Density (-30%)	Ion Rate (+20%)	Camera Angle (+2 deg)
Temp (eV)	10.2	±.2 (2%)	+.9 (9%)	0 (0%)	0 (0%)
Mach	-.40	±.05 (13%)	-.2 (50%)	-.1 (25%)	0 (0%)
Drift (m/sec)	365	±5 (1%)	-24 (7%)	+73 (20%)	-18 (5%)

magnitude increase of 50%. To first order, to keep a plume profile shape, the product of electron density and Mach number needs to be kept constant. (If the electron density is instead increased by 30%, Mach number would need to be decreased in magnitude by about 20%.) This implies that a choice of a reasonable density for the fluid calculations is important; a large error in the chosen density will lead to a correspondingly large error in the found Mach number (if the density is known to 10% or so, the uncertainty introduced will be about the same as the statistical).

For ionization rate, the values used by the model have been measured experimentally and are accurate to within 10%. They do not take finite density effects into account however (the experimental measurements are made under conditions in which the plasma density is essentially zero).[6] The change in parameter fits resulting from an increase of the rates by 20% are found. Because of the non-linearity the rates show with temperature, the change in the temperature fit is negligible. The change in Mach number is significant (about 25%), but probably less so than the change seen with density errors. Since there is no change in temperature, the derived drift velocity changes by the same amount as that posited for the ionization rate, giving an increase of 73 m/sec.

The magnetic field angle at the inner-wall is known accurately (to within a fraction of a degree). There is a slight tilt to the camera which images the plumes however. This tilt was found by observing He-I emission during simultaneous Helium puffs at two locations on the inner-wall (which have the same toroidal location). For the runs 950414 and 950526, this angle was about 7 degrees, for run 951219, about 1 degree. The

---

[6]K.L. Bell, et al, "Atomic and Molecular Data for Fusion, Part I", UKAEA Report CLM-R216, 1982.

plume images are corrected for these angles, which are likely good to within a degree. For a conservative calculation, the plumes were rotated 2 degrees, then the fittings redone (an altered orientation will affect the parallel and perpendicular plume integrations). The parallel profile was more or less unaffected, leading to no change in the fitted temperature and Mach number. For the perpendicular profile, the assumed tilt angle has a greater impact, though still producing relatively small 5% in derived drift velocity.

Though an in depth error analysis is not presented for the other plume fittings presented in the next section, the results of this analysis for shot 951219011 can be generalized, and used to understand the accuracy of the results that are presented. At least for the sources of uncertainty considered, the temperature is largely unaffected, the largest potential uncertainty being less than 10% for an uncertainty in density of about 30% (note that this error-bar on temperature is in fact less than that for the scanning probe measurement). For the poloidal drift velocity, the situation is similar, with, roughly speaking, the value fitted acquiring the same uncertainty (on a percentage basis) as the ionization rates employed by the model (as long as the density used by the model is reasonable; if it is off by a factor of 5, a possibility for the secondary separatrix affected shots, then the error will be much larger). For Mach number, the potential for error is large. If the rate coefficient and background electron density are well known (to say 10%), there will be 10-20% error bars on the fitted Mach number. This would be a satisfactory uncertainty, likely smaller than those for Mach probe measurements, for example. If, however, the density is very uncertain (as it likely is for the cases fitted in runs 950414 and

950526), the error bars will be such to make the parallel velocity measurement only accurate in direction.

6.2 Plume Analysis Results

The shots from three run periods (17 in total) have been analyzed in the same way as 951219011 above, and tabulated in table 6.2. All of the discharges were single-null diverted, 800 kA, 5.3 Tesla on axis. Run 950414 had the plasma current and magnetic field CCW (the discharges are always run with the same helicity; the toroidal B-field and plasma current are always parallel), the other two runs used the standard CW configuration, as is indicated in column 4. The shot numbers and times (of the particular plume image modeled) are listed in the first two columns, the impurity gas injected (the plumes analyzed were observed through C-II, N-II, and He-II filters) is given in the third. The location of the x-point (and hence utilized divertor) is listed in the fourth column, and the volume averaged core electron density (as measured with the TCI and computed with EFIT results) is listed in column six. The measurements of the scanning probe at the appropriate flux surfaces is given in the next two columns. For the Nitrogen and methane injection shots, these values correspond to those at the flux surface grazing the inner-wall at the midplane, for the two Helium shots listed they correspond to those values at the flux surface 9 mm out from the inner-wall. Using the measured density listed in the 7th column, the results of the fluid analysis on the plumes is detailed in the final 5 columns: the temperature, Mach number, and parallel velocity (the Mach number multiplied by the sound speed) found fitting the parallel profile, and the perpendicular velocity and radial electric field (assuming drift velocity is due to ExB) found fitting the

Table 6.2: Summary of Analyzed Plumes

(1) Shot	(2) Time (sec)	(3) Gas	(4) Ip	(5) X-Pnt	(6) Core n_e 10^{20}m^{-3}	Scanning Probe (7) n_e 10^{19}m^{-3}	(8) Temp (eV)	Parallel Plume Model (9) Temp (eV)	(10) Mach	(11) Vel (m/sec)	Perpendicular (12) Drift v (m/sec)	(13) E-Fld (V/m)
950414013	.57	C	CCW	Dwn	0.98	1.2	17.5	10.0	-.30	-8200	-9	72
950414013	.72	C	CCW	Dwn	1.03	1.1	17.0	11.0	-.35	-11500	0	0
950414015	.62	C	CCW	Dwn	2.56	2.4	8.5	7.0	.10	2600	370	-2960
950414023	.57	C	CCW	Up	1.04	1.2	19.0	8.0	.25	7100	0	0
950414025	.62	C	CCW	Up	2.03	2.6	19.0	6.0	.10	2700	-50	400
950526002	.68	C	CW	Dwn	1.50	0.8	13.5	12.5	-.50	-17200	450	3600
950526006	.60	C	CW	Dwn	1.86	3.5	12.0	10.0	-.50	-15400	115	920
950526010	.72	C	CW	Dwn	2.30	5.0	13.0	7.0	-.20	-5600	110	880
950526011	.70	C	CW	Dwn	2.27	5.4	11.0	10.0	-.45	-14300	108	864
950526018	.63	C	CW	Up	1.15	1.5	14.3	7.0	.20	5100	-15	-120
950526022	.72	C	CW	Up	1.73	2.5	21.5	7.5	.20	5800	-122	-980
951219004	.67	N	CW	Dwn	1.51	3.6	8.0	7.5	-.20	-4800	170	1360
951219009	.67	N	CW	Dwn	2.09	4.3	9.5	10.0	-.35	-10900	274	2190
951219011	.67	N	CW	Dwn	2.09	5.6	9.5	10.0	-.40	-12300	365	2920
951219017	.67	He	CW	Dwn	2.31	8.0	15.5	17.0	-.15	-5900	135	1080
951219020	.63	He	CW	Dwn	1.66	3.6	20.0	20.5	-.25	-10000	53	420
951219037	.63	N	CW	Dwn	1.16	1.9	8.0	8.0	-.25	-6300	65	520

perpendicular. A radially outward (in minor radius) electric field is defined as positive.

Because the field lines in the region of a secondary separatrix are not continuous between the scanning probe and the inner-wall midplane, the density used in solving the fluid equations is uncertain for the shots of two of the three run periods. This leads to large uncertainties in the found parameters, for the Mach number in particular, as discussed in the last section. Hence, performing a systematic analysis on these numbers to find trends and dependencies is difficult (only those results for run 951219 can be considered reliable). Except perhaps for the three shots with radially inward electric fields, the numbers found seem reasonable. The temperatures found by analyzing the plumes of run 951219 in fact all well agree with those measured by the scanning probe at the same flux surface (as discussed in the last section, this validates the use of the scanning probe density for these shots). In the other two runs, the plume-found temperatures are all lower, a phenomenon undoubtedly due to having two strike-points on each flux surface on the inboard (cooling the surfaces).

To provide a better visual impression of the plume found background plasma Mach numbers and impurity ion drift velocities listed in table 6.2, they are plotted in figures 6.8 and 6.9. No dependency is meant to be displayed, the values are just plotted in sequence (chronologically). The Mach numbers calculated range between .1 and .5, with the flow towards the primary strike point in all cases but one. The exception (950414015) has the problem magnetic equilibrium shown in figure 6.4. The secondary separatrix for this shot is 7 mm from the inner-wall (10 mm from the LCFS), further out than any of the other shots. This 'reverse flow' can probably be attributed to this magnetic configuration, with the flow going

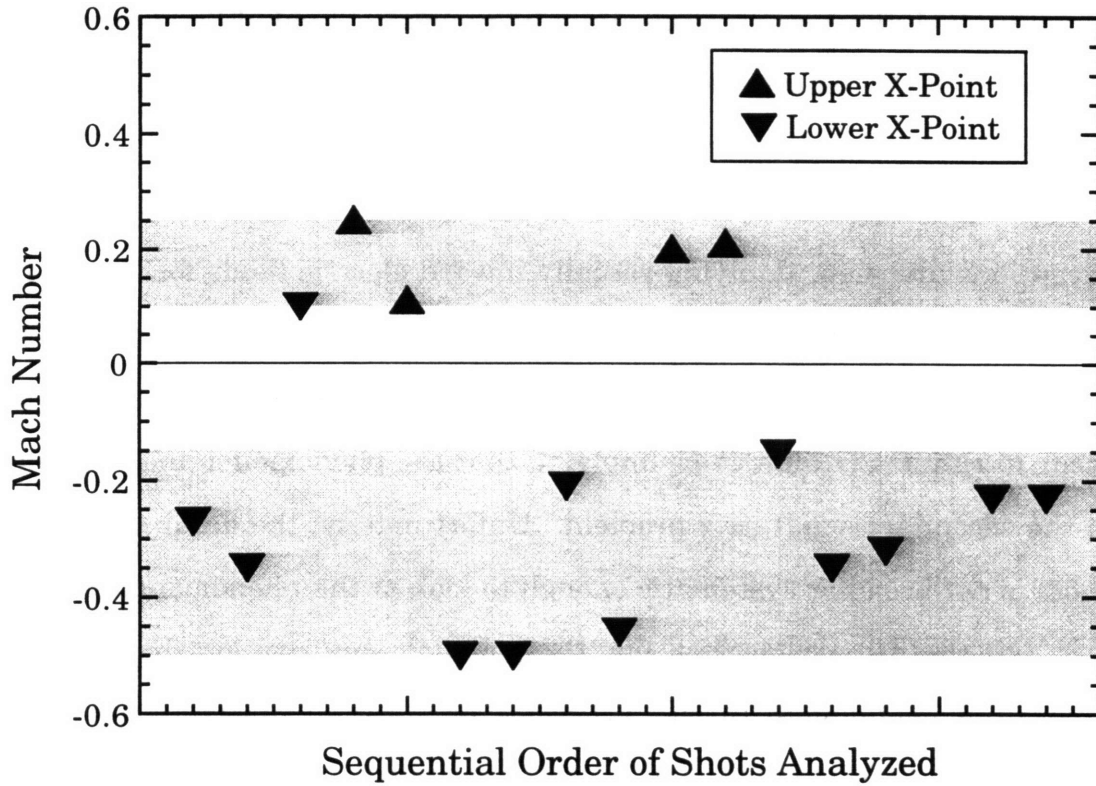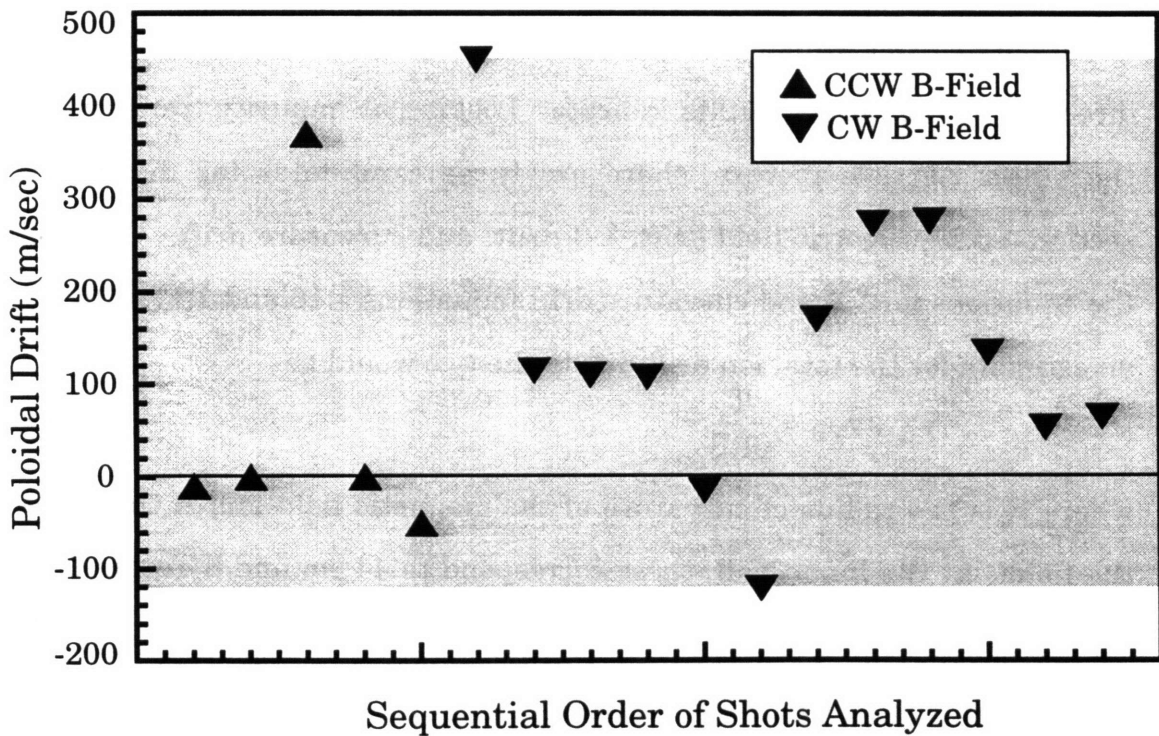## Figure 6.8: Mach Numbers of Analyzed Shots

Figure 6.9: Poloidal Impurity Ion Drift of Analyzed Shots

towards the upper inboard strike point. The found poloidal drift velocities range up to 450 m/sec, corresponding to an electric field of 3600 m/sec if due entirely to ExB. These electric field values are in the same range as those observed with the scanning probe. If the drift is due to ExB, one would expect a positive velocity for CW B-field shots, a negative for CCW. Three exceptions are seen, implying radially inward electric fields for these shots. Because the plasma potential is expected to decrease monotonically with increasing minor radius, it is a bit disturbing. None of the three exceptions occur in run 951219 however, implying that the phenomenon may be related to the secondary separatrix problem. Unfortunately, the database of plume shots is not broad or systematic enough to look at the phenomenon in depth.

In the discussion thus far, the poloidal impurity ion drift has been attributed exclusively to the existence of a radial electric field. From scanning probe measurements, a radial electric field can be deduced of the same orders of magnitudes as the plumes would indicate (more on this in the next section). Additionally, no other cross-field drifts (short of anomalous) exist which can give velocities of the same magnitude and direction as the plume results indicate. Looking at impurity transport from the single particle picture, there are three candidates (as discussed in section 1.3.2): electric field drift, ∇B drift, and curvature drift. Combining the equations for ∇B and curvature drift (equations 1.16 and 1.17 with 1.15), an estimate for the total ion drift due to the two would be:

$$v_R + v_{\nabla B} \approx \frac{T}{eRB} \tag{6.1}$$

where R is the radius of curvature of the magnetic field and B the value of the field. At the inner-wall, these correspond to 44 cm and 8 Tesla. Hence, for temperatures of 10-20 eV, the value of these drifts combine to only a few meters/sec, much below those indicated by the perpendicular plume shapes

(additionally, these drifts point downward for ions in CW B-field shots, the opposite direction of the drifts measured in most cases). Note that the ExB drift will be the same magnitude for both the impurity ions and background Deuterium (no mass dependence), so that the extracted impurity ion drift is that for the background ions as well.

For completeness, the contour plots of the two-dimensional emission plumes of the 17 shots analyzed are given in figures 6.10-12. Additionally, plumes from run 960208 are plotted in figure 6.13. The fluid model was not applied to these shots because of the lack of scanning probe data. The emission patterns, all observed in upper x-point shots, are an anomaly. Though there are hints of flow direction in some of the contours, no distinct direction is shown in any of them. There are two probable contributions to this behaviour: the first is the existence of a secondary separatrix problem on the shots, the second is the nature of the discharges. These were the only somewhat successful upper x-point shots in C-Mod for the run period. The modifier 'somewhat' is used because, except for shot 35, they all experienced disruptions halfway through the shot, at about .75 sec. Because these were the only upper x-point discharges of the run period, it is expected that impurities that had collected on the upper part of the machine were ejected into the plasma in the discharges, causing early disruptions and, most likely, affecting edge flow patterns. Particularly without any modeling analysis or scanning probe data, this is only supposition, but it does seem to be the most likely explanation for the anomalous behaviour.

Figure 6.10: Plume Contours of Run 950414

Shot 23 at .57 sec

Shot 25 at .62 sec

Shot 13 at .57 sec

Shot 13 at .72 sec

Shot 15 at .62 sec

Toroidal Distance (cm)

Toroidal Distance (cm)

Poloidal Distance (cm)
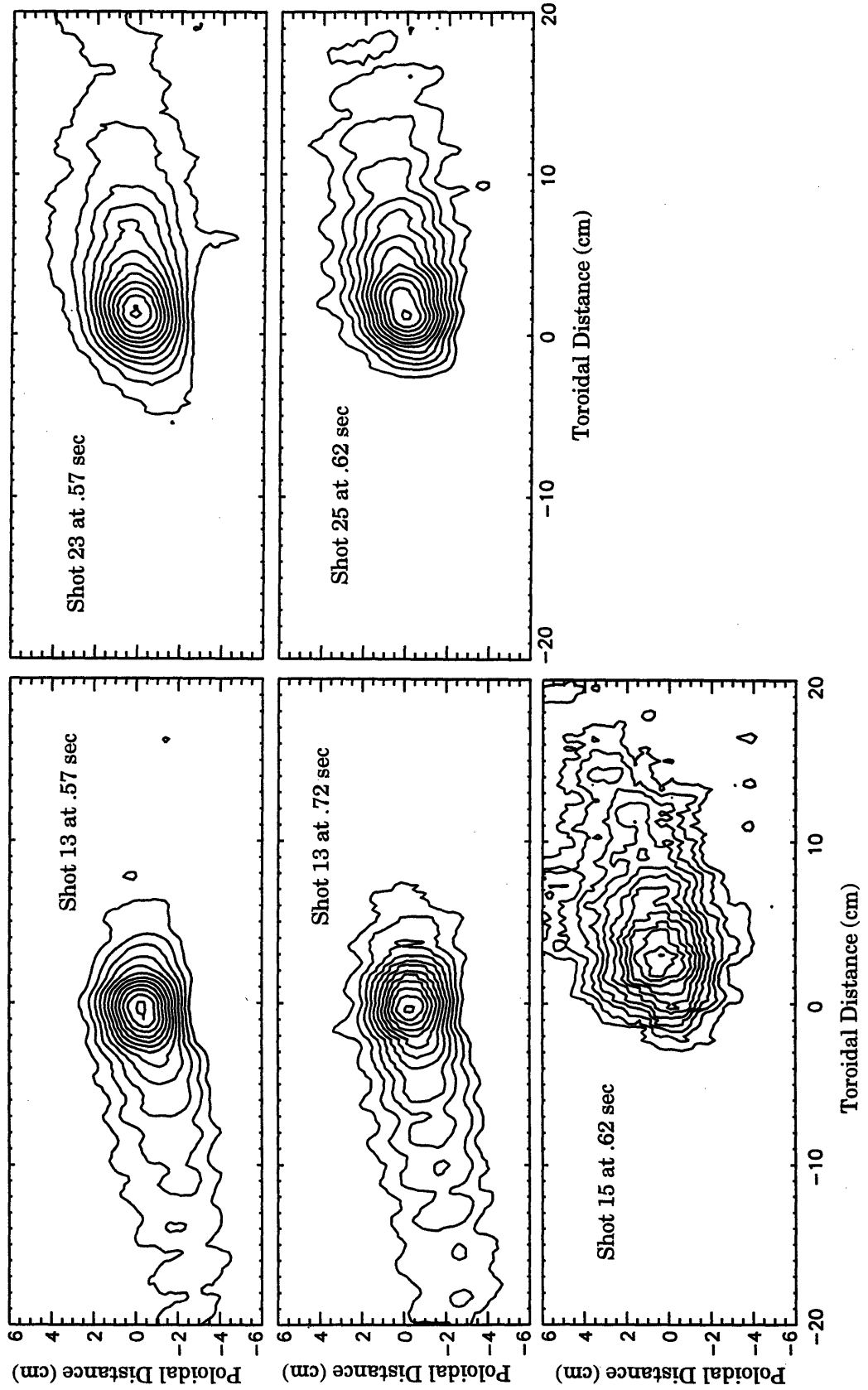
Poloidal Distance (cm)

Poloidal Distance (cm)

Figure 6.11: Plume Contours of Run 950526
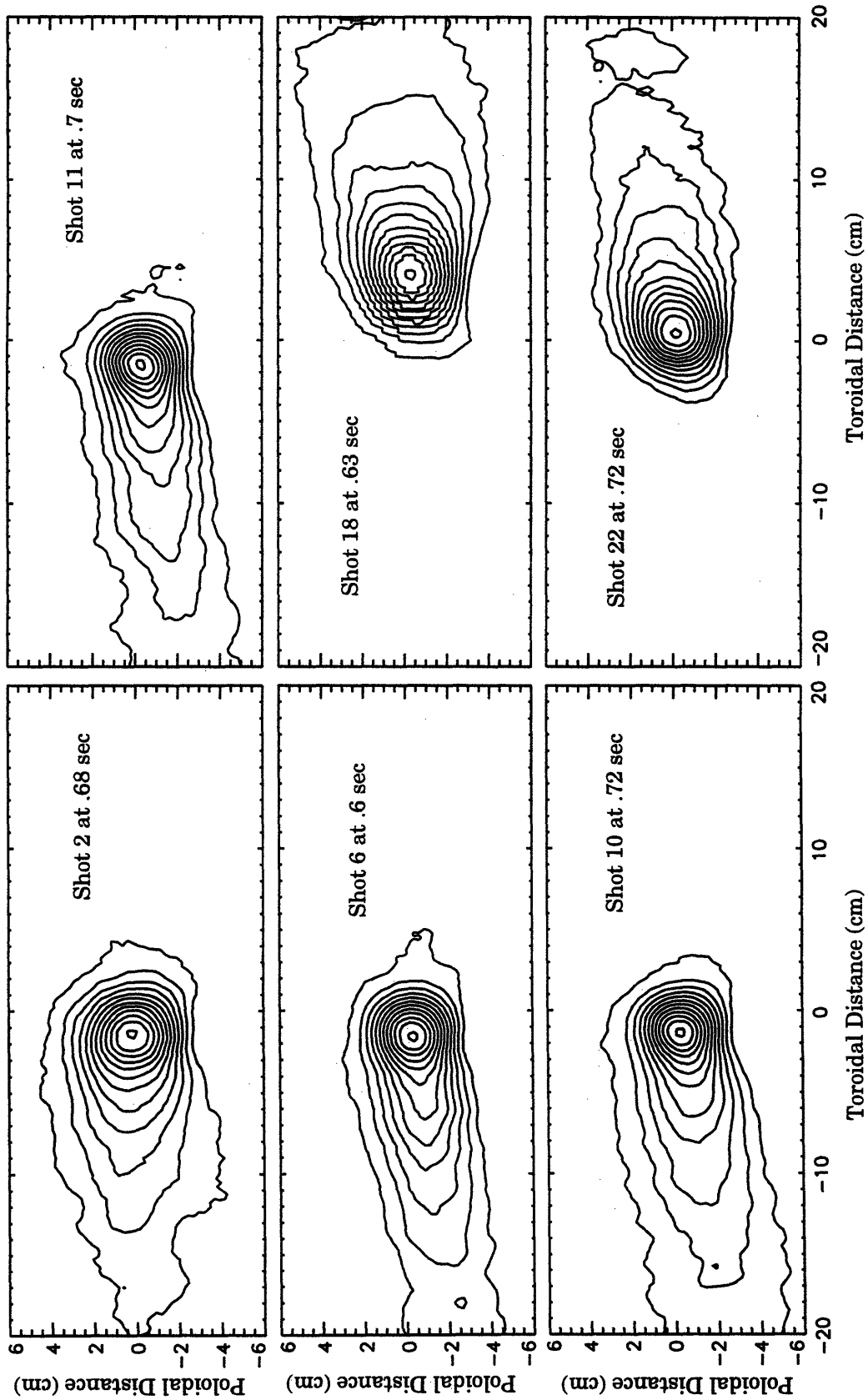
Figure 6.12: Plume Contours of Run 951219
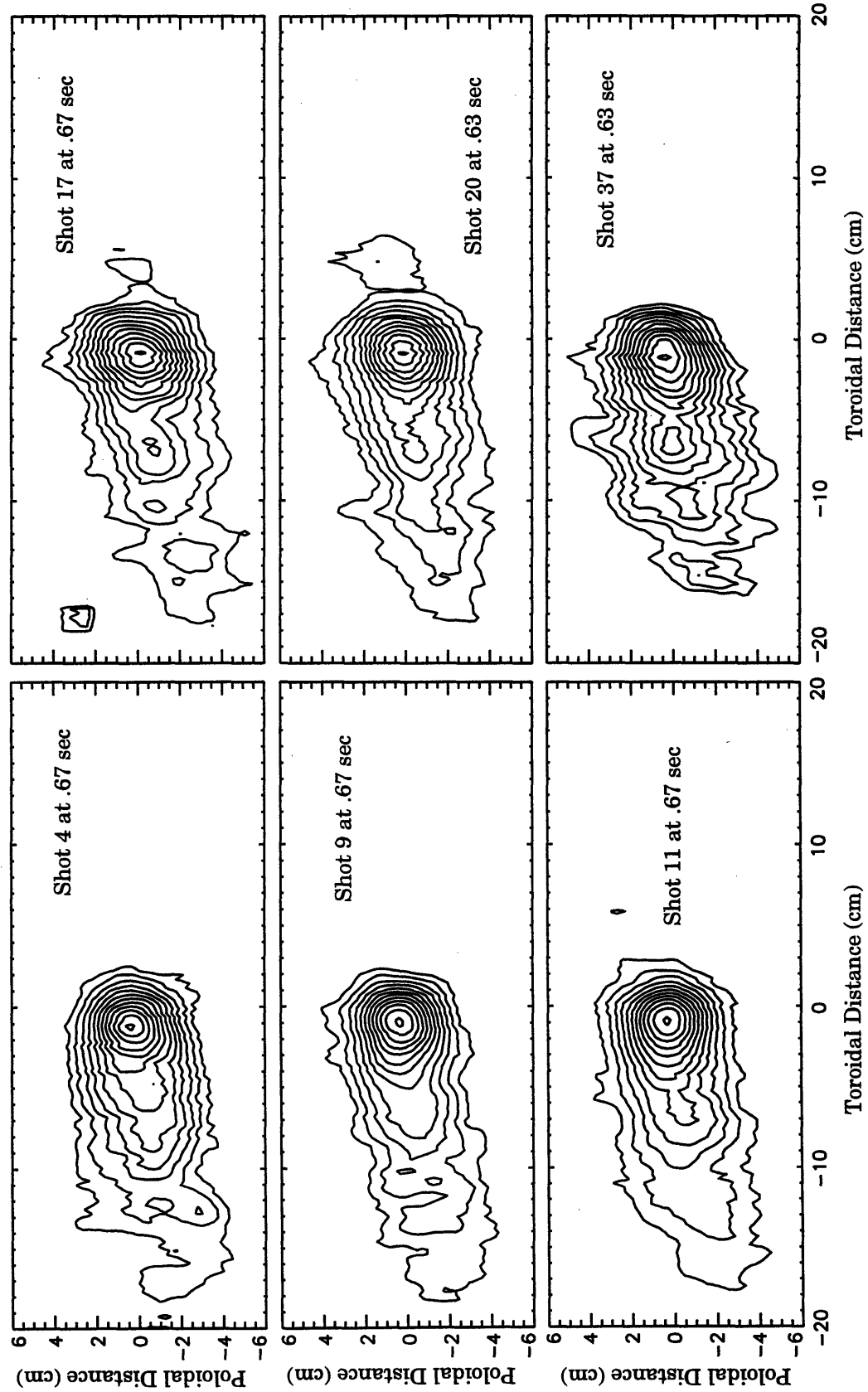
Figure 6.13: Plume Contours of Run 960208
(all upper x-point shots)

Shot 33 at .6 sec
(N-II)

Shot 35 at .6 sec
(N-II)

Shot 20 at .57 sec
(He-II)

Shot 24 at .6 sec
(He-II)

Shot 32 at .63 sec
(N-II)

Toroidal Distance (cm)

Poloidal Distance (cm)
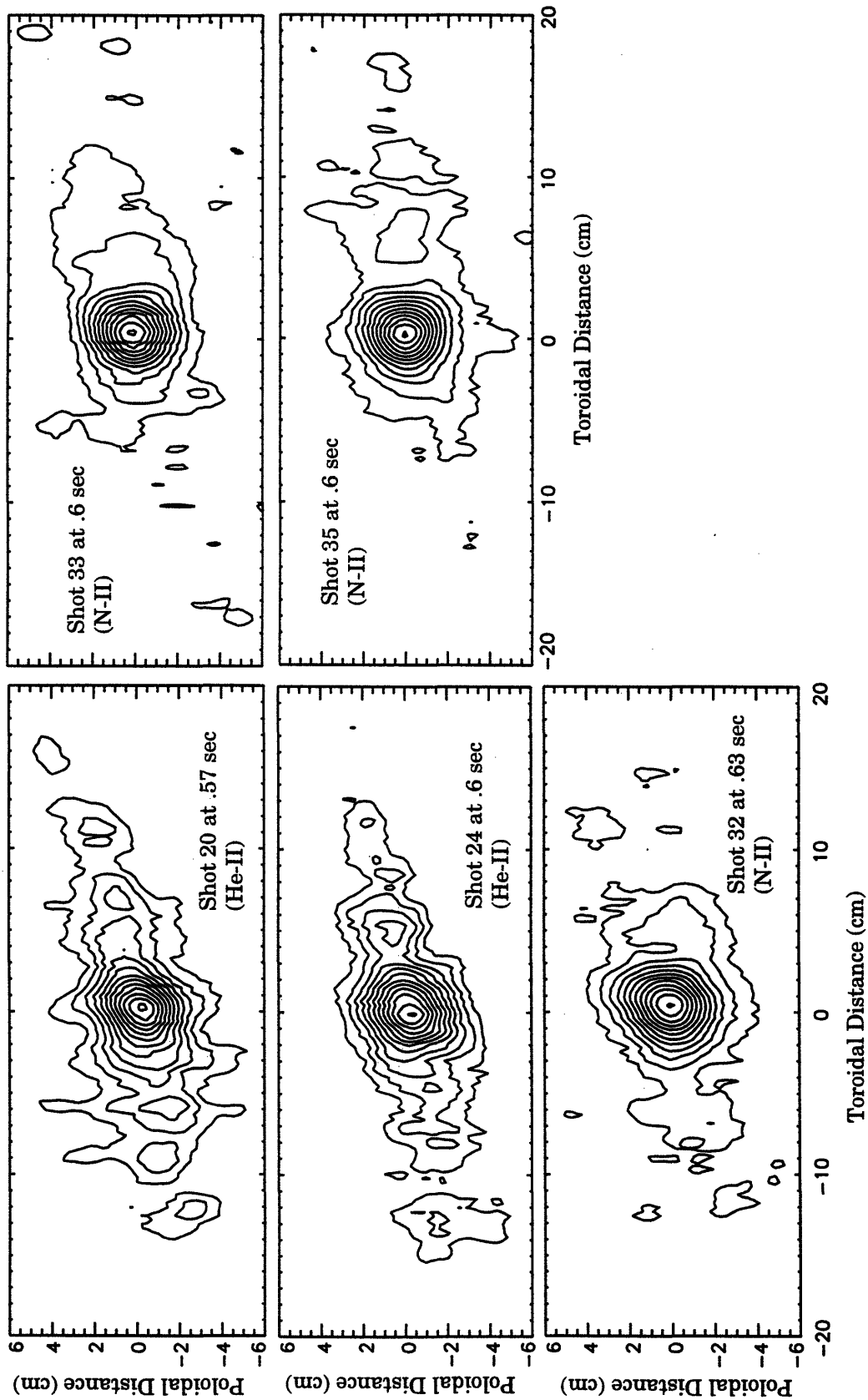
6.3 Comparison with Scanning Probe Measurements

Measurements of Mach number and plasma potential (the radial derivative of which yields electric field) made by the scanning probe can be compared with the results of the fluid analysis. The comparison can only be done qualitatively, of course; there is no reason to suspect that the electric field and parallel velocity at the IWM and scanning probe location would be equal. In fact, for the velocity, they are generally oppositely directed (the comparison of velocities will be performed with absolute values). Since the plume analysis of run 951219 shots are the most reliable (no secondary separatrix problem, good communication along the field lines between the IWM and probe locations), the comparison will be confined to it.

Before performing the comparison, the question of how the scanning probe measurements of Mach number and electric field are made needs to be addressed. Unlike Langmuir probe theory for the computation of plasma density, temperature, and plasma potential from the I-V characteristics of an electrical probe, the theory for computing the plasma ion velocity is unsettled. The ion saturation current measured by a probe is related to the ion velocity incident upon it. To make a measurement of this velocity, one needs two Langmuir probes on the same field line, one of which only collects ions upstream along the field, the other which only collects ions from the downstream side (as is the case with the C-Mod scanning probe). One can then use fluid theory (similar to the parallel equations of section 1.3.2) to relate the ratio of the two ion fluxes to the velocity of the plasma ions along the field line. Specifically, one finds the value of Mach number to be

given approximately by:

$$M = M_c(\alpha) \ln\left(\frac{\Gamma_{i,\text{upstream}}}{\Gamma_{i,\text{downstream}}}\right)$$ (6.2)

such that the sign convention has flow from the upstream to downstream giving a positive Mach number. M_c is called the calibration Mach number. Its value will be dependent on what assumptions are put into the fluid model to obtain equation 6.2, specifically what value is used for the parameter α, a ratio of the perpendicular diffusivities of momentum and particles. In the pre-sheath of each Langmuir probe in a strong magnetic field, there will be a source of ions coming from the perpendicular diffusion of particles from surrounding magnetic flux surfaces. The question becomes what to do about the momentum source in the pre-sheath. It works out that the dependence of the momentum source in the fluid equations appears as a ratio of it to the particle source, specifically the ratio of the momentum to the particle diffusivities (α). Unfortunately, the value of this parameter cannot be calculated from theory (or at least it has not been done yet). It is generally either set to 0, thereby assuming the presence of no momentum source in the pre-sheath, or set to 1, thereby assuming that the diffusivities are equal. For the calibration Mach number, $M_c(0) = 1.0$ and $M_c(1.0) = .45$. Since the question of which paradigm is better is still begged by some (though experimental measurements do seem to show an α estimate of 1.0 to be closer to the actual), the calculations that follow will be made with both. The models will be referred to by the names of their progenitors: Stangeby for α set to zero,[7] and Hutchinson for an α of 1.0.[8] It should be noted that the calculation of density from the I-V characteristic is

[7]P.C. Stangeby, "Measuring Plasma Drift Velocities in Tokamak Edge Plasmas using Probes", Phys Fluids, 27(1984), pp. 2699-704.
[8]I.H. Hutchinson, "A Fluid Theory of Ion Collection by Probes in Strong Magnetic Fields with Plasma Flow", Phys Fluids, 30(1987), pp. 3777-81.

also dependent upon what is assumed for the momentum diffusivity. The dependence is much less pronounced however, and the uncertainty generally not worried about.

The top plot of figure 6.14 shows the profile of the ratio of upstream to downstream ion saturation current measured by the scanning probe in shot 951219011 mapped to the outboard midplane. The primary source of error for these measurements is in the uncertainty of the probe areas which collect the currents. This uncertainty is about 20% for each probe, leading to about 30% uncertainty in the current ratio. Using the ratio, the Mach probe profile calculated using equation 6.2 with both Stangeby and Hutchinson is shown in the lower plot. The current ion ratio uncertainty puts error bars on the Mach number plot of about 25% at each value. The ion velocity is seen to rise radially outward, by Stangeby going from below .2 near the LCFS to supersonic far out in the SOL (values corresponding to .1 and .5 by Hutchinson). The shape of this profile is typical for Mach probe measurements in C-Mod. The indication of supersonic flow by Stangeby is seen often in Mach probe measurements, both in C-Mod and on other machines, and does indeed cast doubt on the accuracy of the model (at least in certain regimes). It should be noted that while not shown in the profile for this particular shot, reverse flow (away from the strike point) is often seen in scanning probe measurements near the separatrix. It is an interesting phenomenon observed on both C-Mod and other machines, and is expected from theory, though the reversal observed on C-Mod appears to have unique characteristics.[9]

---

[9]B. LaBombard, et al, "Experimental Investigation of Transport Phenomena in the Scrape-off Layer and Divertor", Journal of Nuclear Materials, to be published.

Figure 6.14: Mach Number Profile for Shot 951219011
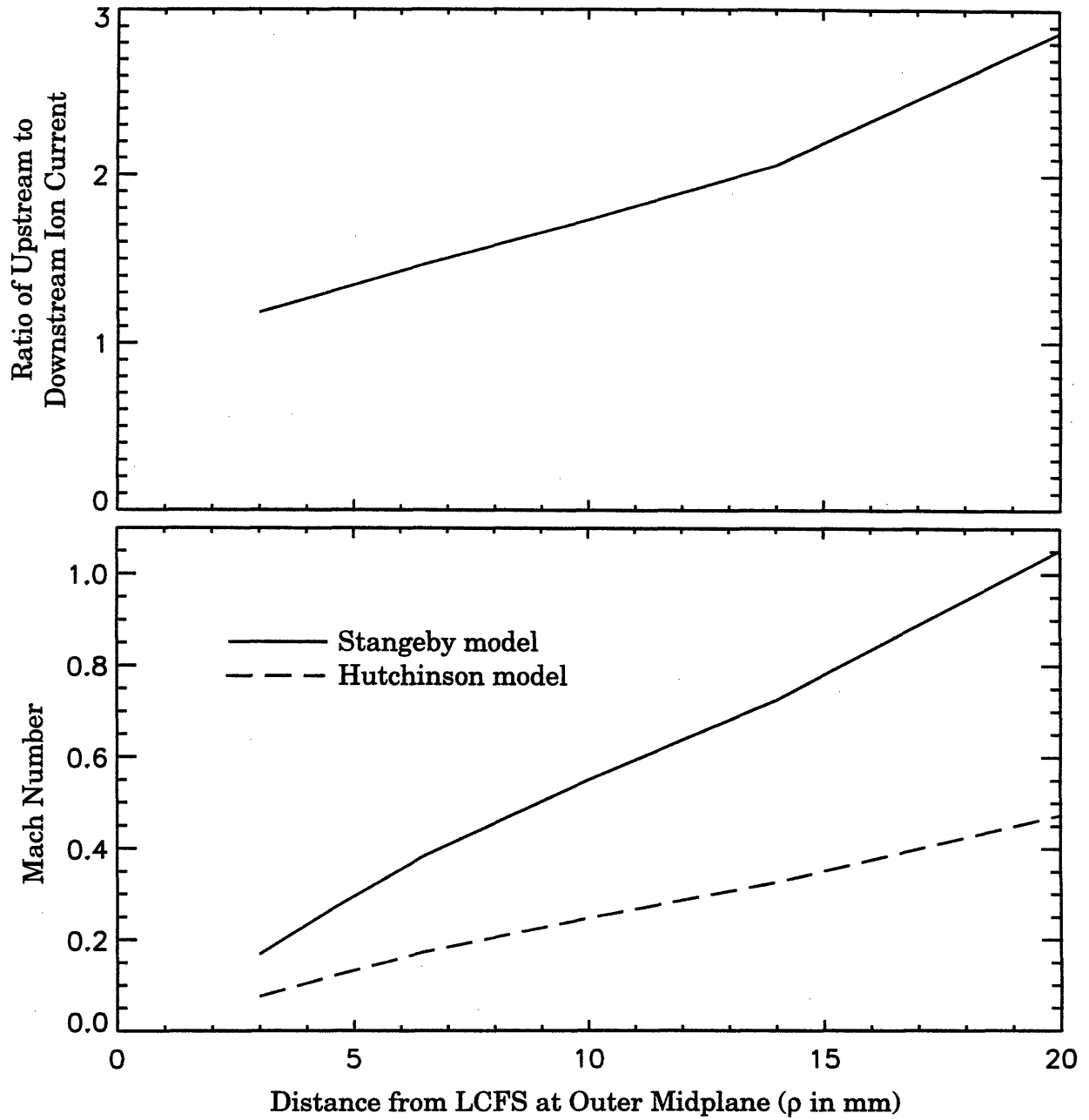
Calculation of the electric field is more straightforward. From well accepted Langmuir probe theory, the plasma potential is known to be (for a Deuterium plasma):

$$V_p = V_f + 3.7 \frac{T_e}{e} \tag{6.3}$$

where the electron temperature, T_e, and the floating potential, V_f, are those measured by the probe. The floating potential is that for which the Langmuir probe collects no current. Potentials are relative to the machine (vessel walls) potential (set to zero). The radial electric field is then the derivative of the plasma potential. The profiles of these quantities (at the outboard midplane) are plotted in figure 6.15. The resulting radial electric field is seen peaked near the LCFS, reaching 10 kVolts/m, dropping off to under 2 kV/m further out in the SOL. The values along this profile are typical for C-Mod scanning probe measurements, as is the profile's monotonic shape. Uncertainties in measured plasma potential and temperature combine for error bars of about 30% on the plasma potential values, and hence about 50% on the electric field values. In other words, the electric field measured in this manner can only claim to be known to within 50%.

Figures 6.16 and 6.17 take these measured values of Mach number and electric field and map them to the inner-wall midplane (the plasma potential is mapped, then its derivative taken). For this particular shot, it is seen that the values at the IWM flux surface are .8 and .36 by Stangeby and Hutchinson respectively for Mach number, and 1500 V/m for electric field. Table 6.3 compares the plume found data with the values of the parameters calculated with scanning probe measurements in the six shots of run 951219. The scanning probe values listed are those on the flux surface mapped to the inner wall for the four Nitrogen injection shots, and those

Figure 6.15: Scanning Probe Derivation of Electric Field

(a) Floating Potential (Volts)

(b) Electron Temperature (eV)

(c) Plasma Potential (Volts)

(d) Radial Electric Field (kVolts/m)

Distance from LCFS at Outer Midplane (ρ in mm)
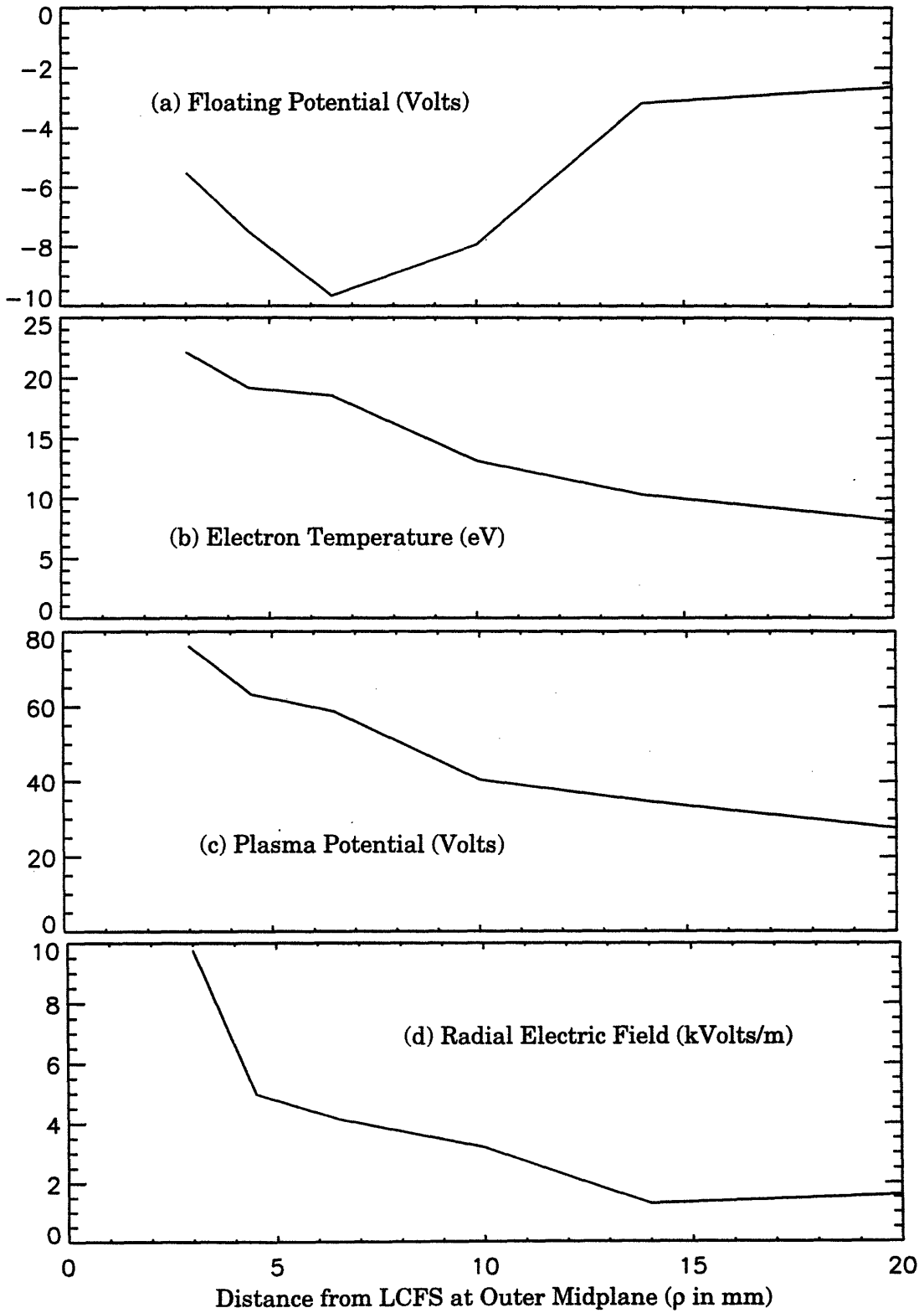
Figure 6.16: Mach Number Profile Mapped to Inner-wall
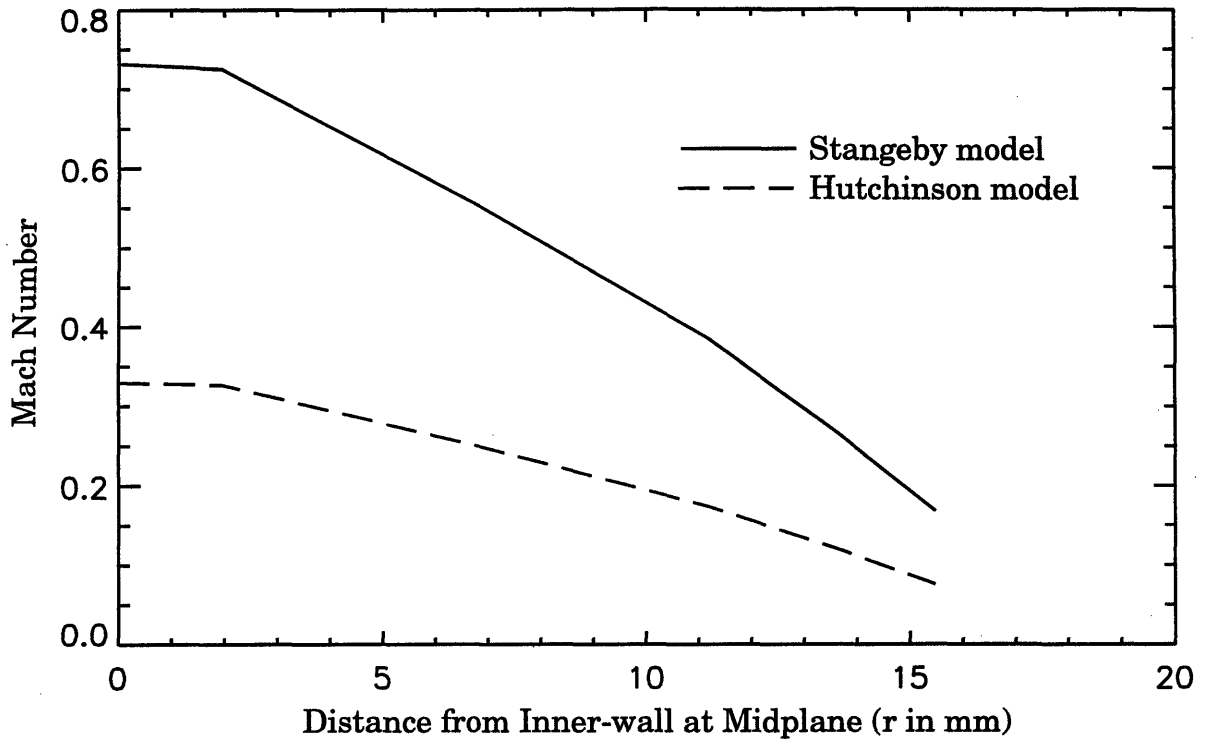
Figure 6.17: Electric Field Profile Mapped to Inner-wall
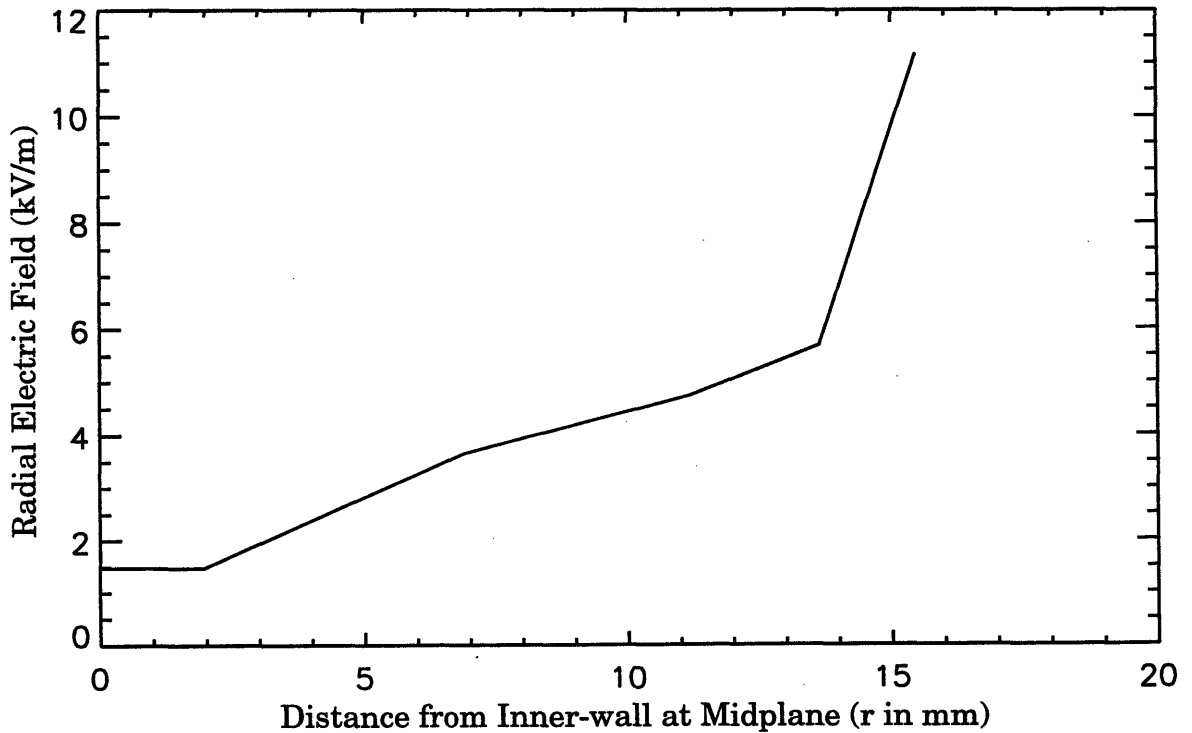
Table 6.3: Plume and Scanning Probe Measurement Comparison

| Shot | Temperature (eV) | | Mach Number (Abs Val) | | | E_r-Field (V/m) | |
	Plume	FSP	Plume	FSP (Stngby)	FSP (Hutch)	Plume	FSP
951219004	7.5	8.0	.20	.97	.44	1360	1100
951219009	10.0	9.5	.35	.70	.32	2190	1900
951219011	10.0	9.5	.40	.80	.36	2920	1500
951219017	17.0	15.5	.15	.45	.20	1080	3700
951219020	20.0	20.5	.25	.30	.14	420	5000
951219037	8.0	8.0	.25	.80	.36	520	1500

mapped to 9 mm from the inner wall for the two Helium injections. The second and third columns of the table recount the agreement the scanning probe measured temperature showed with the plume result (agreement well within the estimated 20% uncertainty of the scanning probe measurement). This agreement does imply good communication along the flux surface between the two locations, providing a justification for a qualitative velocity and electric field comparison (as well as justifying the original use of the scanning probe density in the fluid analysis). In the next three columns, the Mach number measurements are listed for the plume, and for the scanning probe by both Stangeby and Hutchinson. In the last two columns, the electric field measurements are compared (that calculated from the plume coming from assuming the impurity ion drift velocity is entirely due to ExB, as discussed in the last section).

As stated at the beginning of this section, numerical agreement in Mach number and radial electric field is not expected, both because of fair sized error bars on the measurements, and because, even with very accurate measurements, the values of these parameters on the inboard and outboard of the machine will generally be different. For plasma ion velocity in fact, the drifts go in opposite directions (towards the two different strike points, the locations being on opposite sides of the stagnation point). What is sought is qualitative agreement. If very different values are consistently seen, the plume found parameters would be brought into serious question. For Mach number, the Hutchinson theory provides better agreement. Considering the uncertainties on the scanning probe measurement (about 25%), and that on the plume model fit (15% or higher), the numbers do in fact fall within each others error bars in at least five out of the six cases. The agreement in electric field varies from rather close on shots 4, 9, and 11

(well within the 50% uncertainty estimated for the scanning probe measurement), to more than an order of magnitude on shot 20. The two shots for which the agreement in electric field are worst are those with Helium injections. The plume analysis on these required the selection of an 'average' radial location in the face of a broad Helium ionization profile. In the flux surfaces close to the LCFS, there tends to be large variations in the electric field as measured by the scanning probe, so that even if one would think that the plasma potential profiles did not vary greatly with poloidal location, one could find great disagreement in the measurements by being slightly off on flux surface location.

Chapter 7
Implications

The implications of the work presented in the last five chapters is discussed in the three sections that follow. In the first, a brief summary of the results of the work is given. The other two discuss the use of plumes as a scrape-off layer diagnostic. An evaluation of the diagnostic method in light of the results so far observed is given in section two. Future application and refinement of the technique is discussed in the third section.

7.1 Summary of Findings

The findings of the work fall into three categories: results of deuterium fueling studies with the NINJA capillaries, results of impurity screening experiments, and observations and modeling of impurity plumes with the NINJA/Culham diagnostic. Interestingly, the last two show the capillary system to be useful, indeed inimitable, for their respective experimental purposes. The basic result of the first was to show that the poloidal distribution of capillaries is of little use as a SOL plasma control knob other than in its ability to get large Deuterium throughput to the plasma chamber. It was found that for fueling, location played little, if any,

role. With particular analysis of core plasma density and divertor to midplane neutral pressure compression ratio, the properties of the plasma were seen to be solely dependent upon the quantity of fuel introduced. The import of this is that the properties of a discharge cannot be controlled with selective edge fueling.

In impurity screening experiments, it was found that for recycling impurities, the behaviour, termed 'steady-state', was much like that of the Deuterium. The quantity of puffed Neon or Argon entering the core plasma was seen to be a function of the quantity injected, independent of puffing location. For non-recycling impurities, the behaviour was seen to be 'transient'. Rather than the quantity of gas entering the core plasma being proportional to the total amount injected, as was the case with the noble gases, it was seen to be proportional to the instantaneous rate of injection. While the recycling impurities are characterized by a screening efficiency (amount in the core plasma divided by the total quantity injected) which is observed to be roughly inversely proportional to core plasma density, the non-recycling impurities are characterized by a screening time (ratio of quantity in the core to the injection rate). Further, the screening of the non-recycling (specifically in the experiments, methane/Carbon and Nitrogen) impurities is seen to be dependent upon the location of introduction, while showing only weak dependence with core density. NO-RISC, a one-dimensional fluid model, was used to elucidate the physics of the non-recycling transport, giving qualitative agreement in screening time values with those experimentally observed, and showing how the screening time could be expected to vary with puff location. Screening efficiencies of less than 2% are typically observed for Argon and Neon. Screening times between .2 and 5 msec are typically observed for Carbon and Nitrogen.

The plume studies have shown the analysis of ion charge-state emission in the vicinity of a puffing location to be of value. The experiments showed the direction of parallel background ion flow and perpendicular impurity ion flow vividly. The parallel flow indicated by the plumes was seen to be towards the strike-point, in both upper and lower x-point discharges, independent of other plasma parameters. This result was indicated in impurity puffing experiments with methane, Nitrogen, and Helium. Additionally, with a high capillary fueling rate, plumes of neutral Deuterium emission can be observed in the direction of background flow. Quantitative information is extracted from the first charge state impurity ion plumes through modeling. One-dimensional fluid models for the parallel and perpendicular profiles of the impurity plumes are used in tandem to extract the magnitudes of the background ion velocity, the background electron temperature, and the poloidal impurity ion drift. The poloidal velocity is posited as ExB drift, allowing the extraction of the magnitude of the radial electric field. Through benchmarking of the model calculations with DIVIMP, a Monte Carlo code, and by comparison with scanning probe measurements, the model characterization of the plumes was shown to be valid. In analysis of three run days of experiments, background temperatures and flow velocities, and radial electric fields were calculated with the fluid model. Mach numbers from .1 to .5 and electric fields of up to 3600 V/m were found over a variety of discharges.

7.2 Evaluation of NINJA/Culham Diagnostic

The use of impurity plumes to diagnose the edge region of Alcator C-Mod has been a success. Even before any modeling effort, the flow of the background deuterium ions, and the direction of the impurity ion drift is

displayed rather plainly. This on its own is of value because of the great flexibility and ease of use of the diagnostic. These plumes can be observed wherever a capillary puffing location is located, as long as a camera view and appropriate filter is available. This is unique for an edge diagnostic, allowing the finding of flow direction on the inboard of the machine as easily as on the better diagnosed outboard (in fact, it is easier to use inboard locations since they have a better camera view available to them). In this general sense, the one drawback to the diagnostic as it exists is the perturbations to the plasma the impurity puffs cause. This is not as much of a problem for methane (unfortunately, the use of methane puffs on C-Mod has not been allowed since boronization began on a regular basis), but is an obviously major problem with Nitrogen and Helium. Ideally, the puffs would be non-perturbative, and thus could be performed as often as desired. As it is now, C-Mod discharges need to be devoted to plume studies, the perturbative puffs making other experiments difficult to perform simultaneously. As discussed in the next section, this suggests that a viewing camera of higher sensitivity should be a high priority in upgrades to the diagnostic (allowing lower sized puffs to still be bright enough for observation).

With the fluid model outlined in chapter 5, five parameters can theoretically be extracted from the plume shape: background plasma density, background plasma temperature, background plasma velocity, the anomalous poloidal diffusion coefficient for the impurity ions, and the impurity ion poloidal drift velocity. In practice, two of these are rather difficult to extract. To match a parallel fluid solution to an experimentally produced profile with three free variables is problematic, if not impossible. While the shape of the plume profile for any three choices is unique,

because of inevitable noise in the experimentally produced data, it is not unique enough. Instead of finding one unique profile identifying the three parameters, one instead finds a range of profiles giving a similar quality fit to the experimental curve. Since the profile is relatively insensitive to the electron density, and since a measurement of the electron density on the appropriate flux surface is available from scanning probe data, this free variable is eliminated in fitting experiments. For the perpendicular solution, it is found that the profile is far too insensitive to the perpendicular diffusion coefficient value to allow its extraction. Within reasonable values, altering the diffusion coefficient by an order of magnitude makes little observable difference in the profile shape. As discussed in chapter 5, this is because the diffusion lengths are much smaller than the width of the source. One might imagine increasing the experimental observation sensitivity to the perpendicular profile shape with the combination of a higher resolution camera and collimation of the injected neutrals. These steps would seem unlikely to allow the diffusion coefficient to be measured however since noise in the image will never be eliminated and since, short of using a neutral beam, collimation has limits (resolution of less than a millimeter would be required to get a measure of the diffusion coefficient).

Hence, with the parallel equations, the background plasma temperature and parallel velocity are extracted, and with the perpendicular equations, the perpendicular impurity ion drift. Comparisons with DIVIMP and the scanning probe have shown the efficacy of this extraction (and perhaps, more specifically, that these values can be found using a relatively simple fluid model in lieu of a more complex model such as DIVIMP). Error estimates made in section 6.1 showed that for

temperature and poloidal drift/electric field, the error bars are small (20% or less), while that for fitted Mach number can be much larger (roughly in line with the uncertainty of the electron density). A reliable density is necessary to obtain reasonable extracted parameters, particularly for parallel velocity.

The capabilities and limitations of the diagnostic become apparent in comparison with other possible diagnostic techniques for the same edge measurements. SOL temperatures can be found with a number of diagnostics, such as Thomson scattering and with a scanning probe. These two have a number of advantages over the NINJA/Culham diagnostic. First and foremost, they give full temperature profiles. The plume technique cannot give profile measurements, and indeed the radial location of measurements is limited to the ionization location of the injected neutrals. One can use low atomic weight, low ionization rate gases, as has been done with Helium, to observe plumes at various flux surfaces, but this introduces problems of its own (wider radial distribution of the ions, making the location of plume 'measurement' difficult to interpret). NINJA/Culham has two distinct advantages however: its relative ease and cheapness of implementation (assuming a capillary gas injection system is already installed), and its ability to make measurements at any poloidal location. The cost and ease of implementation advantage is particularly apparent compared with Thomson scattering. On the issue of location, both of the other diagnostics are stationary, they cannot give simultaneous measurements at both the inboard and outboard midplane for example (in fact, it is not physically possible for either to give measurements on the inboard in any configuration). On the issue of accuracy of measurement, if the error analysis of section 6.1 is taken as correct, the plume technique has

the potential to measure temperature more accurately than the scanning probe. For the measurement of parallel flow velocity, the comparison is similar. Using Doppler spectrometry, one could measure parallel velocities more accurately than does the plume, but the plume technique has major advantages over Doppler spectrometry in terms of cost, ease of implementation, and the ability to make measurements more or less anywhere in the SOL. In giving a measure of perpendicular flow velocity, the NINJA/Culham method is somewhat unique. The scanning probe provides a measure of electric field, but it indeed does not measure perpendicular flow directly. Attempts have in fact been made to design electrical diagnostics to measure this flow,[1] but the theory to support such measurements is lacking. Doppler spectrometry techniques can be used to measure poloidal flows; the relative advantages and disadvantages are the same as with the parallel measurement.

7.3 Future Work

The results presented on plume analysis are in large part preliminary. Enough data has not been systematically collected to make cogent generalizations about edge flows. What can be drawn from the results is that the plume diagnostic is a potentially very valuable technique. The most basic level of future work is to further the study already begun, obtaining more plume data at the inner-wall midplane in discharges without a secondary separatrix problem, with complimentary scanning probe data. The next step would be to apply the fluid model to locations other than the inner-wall midplane. For the sake of initial measurements

---

[1]C.S. MacLatchy, et al, "Gundestrup: A Langmuir/Mach Probe Array for Measuring flows in the Scrape-off Layer of TdeV", Rev Sci Instrum, 63(1992), pp. 3923.

and diagnostic evaluation, the focus has been on the IWM because of the excellent view accorded to it by the outer Culham camera, and the ease with which the geometry of the transport can be unfolded. Further work can also be performed on benchmarking of the fluid model with DIVIMP or a similar code, and better integrating DIVIMP into fluid analysis, particularly when puffing locations are analyzed for which unfolding the geometry is non-trivial, and in modeling ionization states other than the lowest. On the subject of the fluid model itself, for regular analysis, work could be done on speeding and better automating the code. Though not mentioned in chapter 5, as the code is now written and implemented, it is rather slow and tedious.

The research could be expanded upon, on Alcator or other machines, in a number of ways. Other impurity gases, having different ionization cross-sections, could be employed to confirm results and to examine behaviour at different flux surfaces, for example. Perhaps the most important equipment upgrade that could be made is in installing a camera system of greater sensitivity and resolution. The Hitachi KP-M1 CCD camera employed is sensitive to an illuminance of .5 lux.[2] A camera with a minimum illuminance of .25 lux instead, for example, would allow imaging of plumes of equal quality with half the flow rate now injected into the chamber for these experiments. Such an equipment upgrade is necessary for the plume analysis to become a regularly used diagnostic. One obvious candidate for such a camera system is ACECAT, the higher end version of MACECAD, which uses EEV asynchronous cameras.[3]

2"Operation Manual: KP-M1 Black and White CCD Camera", Hitachi Denshi, Ltd.
3D.H.J. Goodall and M.E. Price, "Plasma Boundary Observations using an Asynchronous CCD Camera with Automatic Exposure Control", Journal of Nuclear Materials, 196-198 (1992), pp. 1047-52.

There are two upgrades which could be made, which while not of being great use for 2-D fluid analysis, would be very useful for analysis by DIVIMP, or a similar code, both in extracting more detailed information (such as diffusion coefficients, and, on a stretch, radial profiles of the plasma temperatures and velocities), and in benchmarking the transport assumptions which go into a Monte Carlo transport code. The most basic of these is to install a beam splitter and two cameras with independent filter wheels on a single view to allow for imaging two ionization states simultaneously. The other is to work out two camera views and a puffing location such that a plume can be well imaged from two views simultaneously (such a situation does not exist on C-Mod currently). Ideally, these views would be perpendicular, allowing the full 3-D shape of a plume to be reconstructed. Both of these upgrades would, of course, work best with a higher sensitivity and resolution camera, such as ACECAT.

Perhaps the most ambitious extension of the work presented in this thesis would be to construct a combination scanning probe/gas injection device. Something of this sort was in fact implemented on DITE.[4] With a fast high-resolution camera system (fast meaning on the order of millisecond resolution) with an appropriate view, one could obtain profiles of plume derived parameters. Because the time-scales of all the relevant atomic processes are faster than the physical scanning time-scales, the successful implementation of such a measurement device is feasible. Additionally, the Langmuir probes would be taking measurements at the same locations, poloidally and radially, as the plumes, allowing for quantitative benchmarking of the measurements made with each

---

[4]It would be of little use in Alcator however, it being a slow-scan device, ref: C.S. Pitcher, et al, "Carbon Impurity Transport around Limiters in the DITE Tokamak", Journal of Nuclear Materials, 162-4(1989), pp. 337-42.

technique. Construction of such a scanning plume probe would be challenging, but could be done at reasonable cost. The largest stumbling block to its implementation would likely be the cost of an appropriate camera system (likely in the hundreds of thousands of dollars), though a gated high sensitivity CCD system might act as a stop-gap (the gating timed so as to give a single plume image at a desired flux surface on each scan).

Works Cited

Allen, A., et al. "The High-Resolution Video Capture System on the Alcator C-Mod Tokamak." Rev Sci Instrum to be published.

Ascoli-Bartoli, U., et al. "High- and Low- Density Plasma Experiments within the MIT Alcator Programme." Plasma Physics and Controlled Fusion Research 1974, volume 1: 191-203.

Bell, K.L., et al. "Atomic and Molecular Data for Fusion, Part I." UKAEA Report CLM-R216 (1982).

Bell, K.L., et al. "Electron Impact Ionization of Molecules." Queens University of Belfast (1990), unpublished.

Bevington, P.R. and D.K. Robinson. Data Reduction and Error Analysis for the Physical Sciences. New York: McGraw-Hill, Inc., 1992.

Chen, F.F. Plasma Physics and Controlled Fusion, Volume 1. New York: Plenum Press, 1984.

Childs, R., et al. "Design, Control, and Operation of the Vacuum and Gas System for Alcator C-Mod." Proceedings of the 15th IEEE/NPSS Symposium on Fusion Engineering (1994), volume 2: 1051-4.

Elder, J.D. and P.C. Stangeby. "The DIVIMP Users Manual." University of Toronto IAS (1995).

Engelhardt, W. and W. Feneberg. "Influence of an Ergodic Limiter on the Impurity Content in a Tokamak." Journal of Nuclear Materials 76-77 (1978): 518-20.

Fairfax, S., et al. "Papers Presented at the IEEE 14th Symposium on Fusion Engineering by the Alcator C-Mod Engineering Staff, Oct. 1991." PFC/JA-91-33.

Goodall, D.H.J. and M.E. Price. "Plasma Boundary Observations using an Asynchronous CCD Camera with Automatic Exposure Control." Journal of Nuclear Materials 196-198 (1992): 1047-52.

Goodall, D.H.J. "Instructions for Operating MACECAD (Multiple Automatic Camera Exposure and Display)." UKAEA (Jun 1994).

Graf, M.A., et al. "Spectroscopic Measurement of Impurity Transport Coefficients and Penetration Efficiencies in Alcator C-Mod Plasmas." Rev Sci Instrum 66 (1995): 636-8.

Graf, M.A. "Impurity Injection Experiments on the Alcator C-Mod Tokamak." Doctoral Thesis, MIT Department of Nuclear Engineering (Jun 1995), PFC/RR-95-6.

Granetz, R.S., et al. "Magnetic Diagnostics in Alcator C-Mod." Rev Sci Instrum 61 (1990): 2967-9.

Granetz, R.S., et al. "A Comparison of Screening between Limited and Diverted Plasmas in the Alcator C-Mod Tokamak." Journal of Nuclear Materials to be published.

Greenwald, M., et al. "Energy Confinement of High-Density Pellet-Fueled Plasmas in the Alcator C Tokamak." Physical Review Letters 53 (1984): 352-5.

Harrison, M.F.A., et al. "Plasma Edge Physics for NET/INTOR." CEC, Brussels (1986), Report EUR-FU/XII-361/86/50.

Herman, R. Fusion: The Search for Endless Energy. New York: Cambridge University Press, 1990.

Hulse, R.A. "Numerical Studies of Impurities in Fusion Plasmas." Nuclear Technology/Fusion 3 (1983): 259-72.

Hutchinson, I.H. "A Fluid Theory of Ion Collection by Probes in Strong Magnetic Fields with Plasma Flow." Phys Fluids 30 (1987): 3777-81.

Hutchinson, I.H. Principles of Plasma Diagnostics. New York: Cambridge University Press, 1987.

Hutchinson, I.H., et al. "First Results from Alcator C-Mod." Phys Plasmas 1 (1994): 1511-8.

Hutchinson, I.H., et al. "The Effects of Field Reversal on the Alcator C-Mod Tokamak." Plasma Phys Control Fusion 37 (1995): 1389-1406.

Hutchinson, I.H., et al. "Plasma Shape Control: A General Approach and its Application to Alcator C-Mod." Fusion Technology to be published.

Hwang, A.G. "The Transport of Impurities in the Boundary Layer of the Joint European Torus (JET)." Doctoral Thesis, University of Toronto Institute for Aerospace Studies (Oct 1994).

Jablonski, D., et al. "First Results from the Alcator C-Mod Reciprocating Probe System." Bulletin of the APS 38 (1993): 3S7.

Jablonski, D., et al. "Capillary Gas Injection Experiments on Alcator C-Mod." Bulletin of the APS 39 (1994): 6P29.

Jablonski, D., et al. "Observation of Impurity Injection Plumes in the Scrape-off Layer of the Alcator C-Mod Tokamak." Bulletin of the APS 40 (1995): 6F3.

Jablonski, D., et al. "Local Impurity Puffing as a Scrape-off Layer Diagnostic on the Alcator C-Mod Tokamak." Journal of Nuclear Materials to be published.

Janeschitz, G. "The ITER Divertor Concept." Journal of Nuclear Materials 220-222 (1995): 73-88.

Janeschitz, G. "Status of ITER." Plasma Phys Control Fusion 37 (1995): A19-35.

Kögler, U., et al. "Experimental Studies and Modeling of Layer Deposition on Limiter Surfaces by Local Gas Injection in TEXTOR." Proceedings of the 22nd European Conference on Controlled Fusion and Plasma Physics (1995), volume IV: 281-4.

Krane, K.S. Introductory Nuclear Physics. New York: John Wiley & Sons, 1988.

Kurz, C. "Tomography of Light Emission from the Plasma Edge of Alcator C-Mod." Doctoral Thesis, MIT Department of Nuclear Engineering (May 1995), PFC/RR-95-5.

Lao, L.L., et al. "Reconstruction of Current Profile Parameters and Plasma Shapes in Tokamaks." Nuclear Fusion 25 (1985): 1611-22.

LaBombard, B. and B. Lipschultz. "DENSEPACK: An Array of Langmuir Probes in the Limiter Shadow Plasma of the Alcator C-Mod Tokamak Fusion Experiment." Rev Sci Instrum 57 (1986): 2415-24.

LaBombard, B., et al. "First Results from the Divertor Probe Array in Alcator C-Mod." Bulletin of the APS 38 (1993): 3S6.

LaBombard, B., et al. "Scaling and Transport Analysis of Divertor Conditions on the Alcator C-Mod Tokamak." Phys Plasmas 2 (1995): 2242-8.

LaBombard, B., et al. "Evidence of Strong Plasma-Neutral Momentum Coupling in the Alcator C-Mod Divertor." Bulletin of the APS 40 (1995): 3P34.

LaBombard, B. Private communication (Feb 1996).

LaBombard, B., et al. "Experimental Investigation of Transport Phenomena in the Scrape-off Layer and Divertor." Journal of Nuclear Materials to be published.

Lamb, H. Hydrodynamics. Cambridge, UK: the University Press, 1895.

Lidsky, L.M. "The Trouble with Fusion." Technology Review Oct 1993: 32-44.

Lipschultz, B., et al. "Dissipative Divertor Operation in the Alcator C-Mod Tokamak." Journal of Nuclear Materials 220-222 (1995): 50-61.

Lipschultz, B., et al. "Modification and Control of Divertor Detachment in Alcator C-Mod." Journal of Nuclear Materials to be published.

Lisgo, S. Private communications (Dec 1995 - April 1996).

Luke, T.C. "Measurement of Particle Transport Coefficients on Alcator C-Mod." Doctoral Thesis, MIT Department of Physics (Oct 1994), PFC/RR-94-12.

MacLatchy, C.S., et al. "Gundestrup: A Langmuir/Mach Probe Array for Measuring flows in the Scrape-off Layer of TdeV." Rev Sci Instrum 63 (1992): 3923.

Matthews, G.F., et al. "Impurity Transport at the DIII-D Divertor Strike Points." Proceedings of the 18th European Conference on Controlled Fusion and Plasma Physics (1990), volume III: 229-32.

McCracken, G.M. and P.E. Stott. "Plasma-Surface Interactions in Tokamaks." Nuclear Fusion 19 (1979): 889-981.

McCracken, G.M., et al. "A Study of Impurity Transport in the Plasma Boundary of TEXTOR using Gas Puffing." Journal of Nuclear Materials 176-177 (1990): 191-6.

McCracken, G.M., et al. "Impurity Screening in Alcator C-Mod." Proceedings of the 22nd European Conference on Controlled Fusion and Plasma Physics (1995), volume II: 313-6.

McCracken, G.M. Private communications (Mar-Apr 1996).

McCracken, G.M., et al. "Screening of Recycling and Non-Recycling Impurities in the Alcator C-Mod Tokamak." Journal of Nuclear Materials to be published.

Neuhauser, J., et al. "Modeling of Impurity Flow in the Tokamak Scrape-off Layer." Nuclear Fusion 24 (1984): 39-47.

Niemczewski, A. "Neutral Particle Dynamics in the Alcator C-Mod Tokamak." Doctoral Thesis, MIT Nuclear Engineering Department (Aug 1995), PFC/RR-95-8.

Niemczewski, A., et al. "Neutral Particle Dynamics in the Alcator C-Mod Tokamak." Submitted to Nuclear Fusion.

Pitcher, C.S. "Tokamak Plasma Interaction with Limiters." Doctoral Thesis, University of Toronto Institute for Aerospace Studies (1987).

Pitcher, C.S., et al. "Carbon Impurity Transport around Limiters in the DITE Tokamak." Journal of Nuclear Materials 162-164 (1989): 337-42.

Pitcher, C.S. and P.C. Stangeby. "Experimental Divertor Physics." Plasma Phys Control Fusion to be published.

Porkolab, M., et al, "Overview of Recent Results from Alcator C-Mod." Plasma Physics and Controlled Fusion Research 1994, volume 1: 123-35.

Post, D.E. "ITER: Physics Basis." Plasma Physics and Controlled Fusion Research 1990, volume 3: 239-53.

Press, W.H., et al. Numerical Recipes in C: The Art of Scientific Computing. New York: Cambridge University Press, 1992.

Rawls, J.M., et al. "Status of Tokamak Research." DOE/ER-0034 (1979).

Rebut, P.-H., et al. "The Key to ITER: the Divertor and First Wall." JET-P(93)06 (Jan 1993).

Rice, J.E. and E.S. Marmar. "Five-Chord High-Resolution X-ray Spectrometer for Alcator C-Mod." Rev Sci Instrum 61 (1990): 2753-5.

Sakharov, A.D., and I.E. Tamm. "Theory of a Magnetic Thermonuclear Reactor", in Plasma Physics and the Problem of Controlled Thermonuclear Reactions. New York: Pergamon Press, 1961: 1-47.

Shewmon, P.G. Diffusion in Solids. New York: McGraw-Hill Book Company, 1963.

Snipes, J.A., et al. "Characteristics of H-Modes on Alcator C-Mod." Phys Plasmas to be published.

Spitzer, L., Jr. Physics of Fully Ionized Gases. New York: Interscience Publishers, Inc., 1956.

Stangeby, P.C. "Measuring Plasma Drift Velocities in Tokamak Edge Plasmas using Probes." Phys Fluids 27 (1984): 2699-2704.

Stangeby, P.C., et al. "Monte Carlo Modeling of Impurity Ion Transport for a Limiter Source/Sink." Nuclear Fusion 28 (1988): 1945-62.

Stangeby, P.C. and G.M. McCracken. "Plasma Boundary Phenomena in Tokamaks." Nuclear Fusion 30 (1990): 1225-1379.

Stangeby, P.C. and J.D. Elder. "Some Possibilities for Measuring Local Plasma Parameters in the Edge Plasma by Impurity Injection." Plasma Phys Control Fusion 33 (1991): 1435-52.

Stangeby, P.C. and J.D. Elder. "Calculation of Observable Quantities using a Divertor Interpretive Code, DIVIMP." Journal of Nuclear Materials 196-198 (1992): 258-63.

Stangeby, P.C. and J.D. Elder. "A Guide to the DIVIMP Code." University of Toronto IAS (1995).

Summers, H.P. "Atomic Data and Analysis Structure (ADAS)." JET (1994).

Weaver, J. "The Development of a Reciprocating Langmuir Probe System for Alcator C-Mod." Bachelor's Thesis, MIT Department of Physics (May 1992).

Wesson, J.A., ed. Tokamaks. New York: Oxford University Press, 1987.

Winter, J. "A Comparison of Tokamak Operation with Metallic Getters (Ti, Cr, Be) and Boronization." Journal of Nuclear Materials 176-177 (1990): 14-31.

IDL (Interactive Data Language), version 4. Research Systems Inc, Boulder, CO.

"Operation Manual: KP-M1 Black and White CCD Camera." Hitachi Denshi, Ltd.